Université du Québec

Institut National de la Recherche Scientifique

Centre Énergie Matériaux Télécommunications

Development of a prototype Time Domain Spectroscopy system for in vivo terahertz thermal imaging

by

Diego Caraffini

Mémoire ou thèse présentée pour l'obtention du grade de

Maître ès sciences (M.Sc.)

Jury d'évaluation

Président du jury et examinateur interne	Prof. Patrizio Antici INRS-EMT
Examinateur externe	Prof. Matthew Reid Department of Physics University of Northern British Columbia
Directeur de recherche	Prof. Roberto Morandotti INRS-EMT
Codirecteur de recherche	Prof. Luca Razzari INRS-EMT

 6 juin 2020

Acknowledgements

I am very grateful to my supervisors Prof. Roberto Morandotti and Prof. Luca Razzari for guiding me throughout my master's program. Without their support, collaboration and vision, it would not have been possible for me to finish my Master. I am also immensely thankful for their generosity in funding my Master and for allowing me to participate in several national and international conferences.

I am very thankful to all the members of the Nonlinear Photonics Group for giving me invaluable suggestions and inputs whenever I needed it. I would specially like to thank Dr. Anna Mazhorova, Prof. Fabio Grazioso and Dr. Alessandro Tomasino, who were always ready to discuss ideas with me, help me with my experiments and assist me in moving my project forward.

Great thanks to all my friends, both in the Institute and Montreal, who did not help the student with his work, but cheered up the person in his life. It may not seem much, but it means a lot to me.

My heartiest thanks also go to the staff members of INRS-EMT's administration, who were always very helpful and supportive.

I also want to thank *M.* Louis Peloquin and *Mme* Danielle Meilleur, retired *réviseure* of *Université Laval*, for the help in proofreading the final version of the thesis.

Dulcis in fundo, my dear wife Valentina, who sustained and spurred me forward, always believing, always loving. Any words I might choose to express my gratitude would fall miserably short and I am left speechless before you.

Abstract

Terahertz radiation (THz or Terahertz) is that part of the electromagnetic spectrum lying between the electrical domain of microwaves and the optical domain of infrared radiation ($0.1\,\mathrm{THz}$ to $10\,\mathrm{THz}$), which is now blooming with a myriad of new applications after decades where it was only considered as some sort of technological 'gap', mainly because of a lack of standardized generation and detection systems.

The most common applications of THz are in the industrial domain as a non-contact means to perform material identification, measure thickness of plastic objects and coatings, as well as carry out spectroscopic analysis of packaged substances. It is also used for cultural heritage diagnostics, security inspections (body scan) and many other uses.

The intrinsic safety of THz, due to its characteristic low photon energy that cannot cause ionization, makes it suitable for probing living tissues, and a highly attractive candidate for sensing and monitoring systems in the biological and biomedical fields. We are particularly interested in the use of THz as a complementary instrument in the therapy of skin cancer, which is becoming an increasingly common occurrence in developed countries and imposes a significant burden on society.

After being reflected by the skin, THz carries information about the refractive index of the water contained in epidermal tissue that can be used to infer the temperature and hydration of the skin. This could prove to be invaluable as a monitoring tool during sessions of Photothermal Therapy (PTT) and enable us to assess its outcome afterwards.

This thesis is part of a larger research project that aims first to demonstrate the feasibility and utility of a THz-based monitoring system for PTT and then to refine the analysis algorithms and measurement procedures to allow this idea to exit the physics research laboratory and become a tool commonly used in the healthcare system. This work focuses on the development of a fast and reliable data acquisition system that will constitute the basis of the project. The setup will have to be powerful and flexible enough to accommodate the necessities of a research environment, but present an interface that is simple to use and understand for operators that have no specific training in spectroscopy and nonlinear optics.

The first chapter briefly reviews the medical and social issues that physics is called upon to address and summarizes why this new approach to thermal monitoring is an interesting alternative to other well-established techniques.

The second chapter illustrates the state of the art in the field of THz generation and detection, in order to allow us to *i*) evaluate the viability of the various options for use in a clinical context and *ii*) choose the most appropriate ones.

The third chapter describes in detail the setup itself, from the point of view of both the hardware components and the software used to drive them, thereby providing adequate justification for the choice of components and software architecture. This chapter also contains the description of the measurement procedures employed for each operating mode of the setup.

The fourth chapter describes a set of measurements performed with the aim *i*) of characterizing the instrument used, *ii*) determining how its operating mode affects the collected data and *iii*) establishing the limits within which the settings of the various sub-systems should lie to ensure optimal performance. One of the tests involves the simulation of a PTT session on a porcine skin model to show that the setup is actually capable of performing its function, in conditions as close as possible to its intended use.

The fifth chapter contains the conclusion and several suggestions for future development of the system.

Contents

Acknowledgements **ii**

Abstract **iii**

Liste des figures **vii**

Liste des abréviations **ix**

Résumé **xi**

0.1 Organisation de cette thèse xiv

0.2 Introduction au Térahertz xv

0.3 Description du système xxi

0.4 Évaluation des performances du système xxvi

0.5 Conclusion et perspectives xxxv

Bibliographie **xxxviii**

Liste des publications **xlvii**

List of figures **1**

List of abbreviations **5**

1 Motivation **8**

2 Introduction to Terahertz **12**

2.1 Review of generation and detection methods 14

2.1.1 Continuous Wave (CW) sources 15

2.1.2 Continuous Wave (CW) detectors 18

2.1.3 Broadband pulsed sources and detectors 20

3 Description of the setup **30**

3.1 Optical path 31

3.2 The software 35

3.2.1 User Interface 38

3.2.2 Graphing module 40

3.2.3 Output file management module 42

3.2.4 The slow scan procedure 43

3.2.5 The fast scan procedure 46

3.2.6 Image scanning 53

4 Assessment of the setup **58**

4.1 Slow scan 58

4.2 Fast scan 62

4.3 Imaging 67

5 Conclusion and future development **73**

Appendix A Format of saved data **76**

A.1 Generic block 76

A.2 Scan data block 78

A.3 Record block 79

A.4 Pixel block 80

A.5 Image block 81

Bibliography **89**

List of publications **102**

Liste des figures

1 Répartition des causes de décès les plus courantes en 2016. Le cancer se classait au deuxième rang dans le monde par une bonne marge, mais si l'on considère seulement les pays riches, la marge est réduite, dans le cas du Canada, les maladies cardiovasculaires ont cédé la première place au cancer, même si la marge est moindre. xii

2 La plage de rayonnement térahertz se situe entre les portions « infrarouge lointain » et « micro-ondes » du spectre électromagnétique. xvi

3 (a) Diagramme de bande d'une PCA: les transitions intrabande rapides provoquent l'émission du signal, jusqu'à ce que la relaxation non radiative arrête le processus. (b) Diagramme schématique d'une PCA utilisé en configuration d'« émetteur »: [...] (c) Diagramme schématique d'une PCA utilisé en configuration de « détecteur »: [...] xxi

4 (a) Vue en plongée du système TeTechS. [...] (b) Vue supérieure du boîtier de commande TeTechS. [...] (c) Vue du panneau avant du boîtier de commande TeTechS. [...] xxiii

5 Tracés du décalage du signal ***a***, de la valeur maximale du pic d'impulsion ***b***, de la position ***c*** et de la FWHM ***d***, du bruit d'obscurité (Dark Noise, DN) ***e*** et de la gamme dynamique (Dynamic Range, DR) ***f*** pour les traces prises avec t_{int} allant de 10 µs à 10 000 µs. La plage ombrée en vert est considérée comme optimale pour le fonctionnement réel. xxviii

6 Comparaison entre les acquisitions réalisées avec t_{int} égale à 10 µs et 100 µs. Le plus petit t_{int} n'est pas capable de filtrer le bruit, à tel point que, dans le panneau supérieur, les fluctuations au pic du signal tombent hors de l'échelle (> 10 V). Le plus grande t_{int} utilisé pour la trace dans le panneau inférieur est celui que est sélectionné par défaut dans le logiciel. xxix

7 Comparaison entre la mesure de référence effectuée avec la ligne à retard lente (slow delay line, SDL) et les acquisitions rapides: pour plus de clarté, seules les acquisitions effectuées à $1\,\mathrm{Hz}$, $5\,\mathrm{Hz}$, $6\,\mathrm{Hz}$ et $10\,\mathrm{Hz}$ sont signalées et les tracés ont été décalés dans le temps de façon que les positions des pics soient les mêmes. L'accord se détériore progressivement avec des fréquences d'acquisition plus élevées qui sont associées à des t_w, plus longs, jusqu'à $5\,\mathrm{Hz}$. [...] xxx

8 Valeur de crête des traces THz prélevés pendant l'irradiation de l'échantillon de peau de porc. Les trois tracés correspondent à l'irradiation sur les trois lignes: supérieure, centrale et inférieure. Notez que la ligne centrale a été mesurée en premier, suivie dans l'ordre par les lignes supérieure et inférieure, d'où les traces dans les axes abscisses. [...] xxxi

9 ***a*** Photographie de l'échantillon de peau après irradiation. ***b*** Définitions des paramètres de forme extraits par les traces mesurées par **`Image_scanner`**: les amplitudes du pic principal (E_{THz}^{peak}), de la vallée d'attaque (E_{THz}^{front}) et de la première vallée de fuite (E_{THz}^{tail}), ainsi que leur largeur d'impulsion respective (Δt^{peak}, Δt^{front} and Δt^{tail}). xxxiii

10 Imagerie de l'échantillon de peau à l'aide de diverses propriétés des impulsions THz réfléchies. [...] xxxiv

Liste des abréviations

3D tridimensionnel(le) (three dimensional)

BLOS au-delà de la vue directe (Beyond the line of sight)

BWO oscillateur à onde rétrograde (Backward Wave Oscillator)

CT chimiothérapie (chemotherapy)

CW onde continue (Continuous Wave)

DAQ boîtier d'acquisition (Data Acquisition)

DFG génération de fréquence différence (Difference Frequency Generation)

DNA acide désoxyribonucléique (deoxyribonucleic acid)

DN bruit d'obscurité (Dark Noise)

DR gamme dynamique (Dynamic Range)

EM électromagnétique (Electro Magnetic)

FDL ligne à retard rapide (fast delay line)

FEL laser à électrons libres (Free Electron Laser)

FTIR transformation de Fourier infrarouge (Fourier Transform Infrared)

FWHM largeur à mi-hauteur (Full Width at Half Maximum)

GNR nanotiges d'or (Gold Nanorods)

IR infrarouge (Infrared)

MKRD *Measurement Kit for Research and Development*

NIR proche infrarouge (near infrared)

NI National Instruments

NP nanoparticules (nanoparticles)

OR redressement optique (Optical Rectification)

PCA antenne photoconductrice (Photoconductive Antenna)

PDT thérapie photodynamique (Photodynamic Therapy)

PRF fréquence de répétition des impulsions (pulse repetition frequency)

PTT thérapie photothermique (Photothermal Therapy)

QCL laser à cascade quantique (Quantum Cascade Laser)

RT radiothérapie (radiotherapy)

RDX Triméthylène-Trinitramine (Research Department Explosive)

SDL ligne à retard lente (slow delay line)

SRF fréquence de balayage (Scan Repetition Frequency)

TDS spectroscopie résolue en temps (Time Domain Spectroscopy)

T-GAP lacune térahertz (THz Gap)

THZ-TDS spectroscopie térahertz résolue en temps (Terahertz Time-Domain Spectroscopy)

THZ/Térahertz rayonnement térahertz (Terahertz radiation)

TNT trinitrotoluène (Trinitrotoluene)

UI interface utilisateur (User Interface)

VI instrument virtuel (Virtual Instument)

ZnTe tellurure de zinc (Zinc Telluride)

Résumé

La recherche en physique n'est pas seulement un moyen de satisfaire la curiosité innée de l'homme. Bien que cela ne soit pas évident au grand public, il y a toujours eu une synergie entre l'étude des phénomènes naturels et l'ingénierie, dont l'objectif ultime est de fournir des solutions à des problèmes pratiques touchant pratiquement tous les aspects de la vie humaine — en les améliorant, à partir du repos (matelas en mousse viscoélastique) jusqu'au voyage (avions). Parmi tous ces aspects, le plus important est, sans doute, la santé. Au fur et à mesure que la science médicale progresse, l'incidence et la gravité relative des maladies changent, et de nouveaux défis se présentent sur la scène ; le cancer, malheureusement, en est un bon exemple.

Le cancer est le résultat d'un déséquilibre dans le processus biologique de l'apoptose, qui maintient la santé du corps par la mort « programmée » et la subdivision des cellules. Lorsque le matériel génétique (DNA) est endommagé pendant la mitose, les cellules touchées peuvent commencer à croître, à se multiplier plus rapidement que la normale, et aussi à mourir plus tard que prévu, formant une tumeur. Puisque les dommages au DNA sont un effet aléatoire, l'allongement de la durée de vie rend moins probable qu'une personne ne soit jamais affectée. En fait, dans plusieurs pays, le cancer se classe au deuxième rang des causes de décès les plus fréquentes à la suite de maladies cardiovasculaires et, avec une amélioration significative du traitement et de la prévention de ces dernières, la première devrait prendre de l'importance dans de nombreuses régions du monde. Déjà en 2016, le Canada a vu le cancer gagner du terrain sur les maladies cardiovasculaires (voir figure 1) [1], devenant presque deux fois plus fréquent que dans le monde entier.

Ces chiffres sont sujets à des variations au fil des ans, mais ils établissent fermement le cancer comme un fardeau majeur de la maladie, causant des souffrances aux millions de personnes qui sont diagnostiquées atteintes de cancer dans le monde et à leurs familles. De nombreuses stratégies sont à l'étude pour le traitement de cette maladie, mais certaines des plus anciennes sont encore considérées comme parmi les plus réussies, à savoir la chirurgie, la chimiothérapie (chemotherapy, CT) et la radiothérapie (radiotherapy, RT). [2, 3]. Ces traitements sont assez nocifs pour le patient, car ils impliquent l'ablation ou l'endommagement cellulaire des tissus entourant la tumeur (chirurgie et RT), ou l'administration de substances qui causent une intoxication locale et systémique (CT). Une part significative de l'effort de la recherche dans la thérapie du cancer est consacrée à la réduction des effets

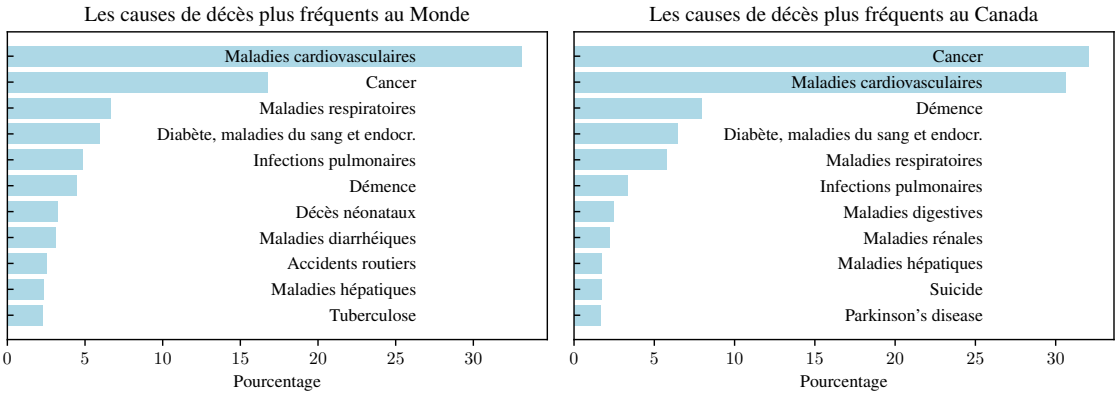

FIGURE 1 : Répartition des causes de décès les plus courantes en 2016. Le cancer se classait au deuxième rang dans le monde par une bonne marge, mais si l'on considère seulement les pays riches, la marge est réduite, dans le cas du Canada, les maladies cardiovasculaires ont cédé la première place au cancer, même si la marge est moindre. [1]

indésirables en développant des médicaments qui peuvent attaquer les cellules tumorales plus sélectivement, soit à cause de leur chimie, soit grâce à des systèmes de livraison sophistiqués.

D'un intérêt particulier pour les physiciens dans le domaine de l'optique, les techniques de thérapie photodynamique (Photodynamic Therapy, PDT) et de thérapie photothermique (Photothermal Therapy, PTT) utilisent le rayonnement électromagnétique (Electro Magnetic, EM) causant la perturbation des cellules tumorales. Les deux techniques reposent sur des substances qui sont absorbées de préférence par les cellules tumorales et excitées par des stimuli de lumière, mais diffèrent en ce que la PDT provoque une série de processus photochimiques et photobiologiques de la part du médicament, tandis que la PTT utilise la substance active comme milieu pour produire de la chaleur sélective dans le tissu cancéreux. [4, 5]

Le chauffage est généralement obtenu par excitation plasmonique de nanoparticules qui résonnent avec la lumière infrarouge (Infrared, IR) et transfèrent de l'énergie au tissu par le processus de relaxation plasmon-phonon [6]. Les matériaux plasmoniques les plus couramment utilisés pour les applications biomédicales sont les métaux nobles, comme l'or et l'argent, en raison de leur toxicité inférieure connue sous forme de masse, bien que la possibilité que le fait d'être sous forme de nanoparticule puisse se comporter différemment et nécessite une étude plus approfondie.

Pour des raisons évidentes, ce type de traitement n'est applicable que pour les tumeurs qui ne sont pas trop profondes sous l'épithélium (y compris celles des cavités internes accessibles par endoscopie) et est considéré

principalement comme adjuvant à d'autres thérapies ; toutefois, le cancer de la peau est de plus en plus fréquent, selon une étude réalisée en 2014 sur les données recueillies jusqu'en 2006 qui indique une augmentation du type histologique le plus grave, le mélanome, de $1.2\,\%$ et $1.5\,\%$ pour les femmes et les hommes, respectivement, surtout chez les jeunes adultes. [7]

En particulier, la pratique de la PTT augmente la nécessité de surveiller la température atteinte par la zone traitée, car elle est la clé de l'efficacité du processus.

Dans la peau, la température peut être déterminée en mode contact par des thermomètres [8] basés sur des thermistances ou par thermométrie infrarouge et thermographie [9–11], mais les premiers nécessitent un contact avec la peau (ce qui augmente le risque de contamination), et donnent une mauvaise résolution spatiale, empêchant ainsi de discerner le chauffage différent entre les cellules saines et cancéreuses.

Les thermomètres infrarouges fournissent une détection non destructive et sans contact en détectant le rayonnement infrarouge, dans la plage de $8\,\mu\mathrm{m}$ à $13\,\mu\mathrm{m}$, qui émane d'objets chauds, et permettent la reconstruction d'images thermiques à deux dimensions [9, 12, 13] ; toutefois, leur précision se détériore rapidement avec la profondeur sous la surface de la peau à laquelle la chaleur est acheminée. De plus, les deux méthodes ne fonctionnent pas au-delà de la vue directe (Beyond the line of sight, BLOS) ou dans des conditions obstruées, e.g. par une gaze médicale.

Pour obtenir une mesure sans contact de la température sous-cutanée, avec une résolution sous-micrométrique, il est possible d'utiliser des nanoparticules (nanoparticles, NP) [14–19] qui fournissent des capacités de détection thermique intracellulaire, bien que le choix des matériaux devrait être mûrement réfléchi, car ils doivent être injectés en plus des substances nécessaires pour effectuer le traitement.

L'alternative au NP fluorescent est l'exploitation des propriétés du rayonnement térahertz (Terahertz radiation, THz ou Térahertz) qui n'est pas ionisant et cause donc un préjudice minimal aux tissus biologiques pour extraire plusieurs propriétés optiques du tissu lui-même (e.g. : son indice de réfraction complexe [20, 21]) à différentes profondeurs avec une résolution spatiale submillimétrique.

La connaissance de la dépendance par la température du changement de l'indice de réfraction dans l'eau du THz [22, 23] peut être appliquée pour déduire la température et le niveau d'hydratation de la peau et être utile pendant les séances de PTT, pour vérifier que la quantité appropriée de chaleur est livrée dans la zone pertinente.

Jusqu'à présent, il existe peu d'études sur l'application de NP excitées par laser comme agents de contraste à l'imagerie des cellules cancéreuses à l'aide de la spectroscopie térahertz résolue en temps (Terahertz Time-Domain Spectroscopy, THz-TDS) [24–26], ou pour chauffer les suspensions aqueuses de NP tout en caractérisant la dynamique de la température à l'aide du THz [27, 28].

Les études rapportées se sont principalement concentrées sur l'imagerie bidimensionnelle THz des tumeurs dans les organes excisés ou ont caractérisé la distribution de chaleur sur des NP injectées dans les tissus cutanés. Cependant, les études mentionnées ci-dessus n'ont pas exploité toute l'étendue des capacités du THz, par exemple pour récupérer des informations sur l'amplitude et la phase qui peuvent être utilisées pour obtenir une analyse précise du temps de vol.

Ce travail de thèse s'inscrit dans un projet dont le but ultime est d'utiliser les informations qui peuvent être recueillies par spectroscopie résolue en temps (Time Domain Spectroscopy, TDS) pour effectuer des mappages tridimensionnel(le)s (three dimensionals, 3Dss) avec l'imagerie thermique THz pour visualiser la distribution cutanée des NP [29] injectées ou coulées en gouttes dans différents échantillons de tissus cutanés avec et sans excitation par illumination laser, par analogie avec ce qui a été montré dans des études récentes impliquant la distribution sous-cutanée d'un médicament dans les tissus biologiques [28, 30].

Bien que la caractérisation initiale sera effectuée sur des solutions aqueuses et de la peau de porc, le système finale est destinée à être utilisée comme complément au traitement clinique des patients. Le but de cette thèse est donc le développement d'un système rapide et fiable pour l'acquisition de données, avec une interface destinée au personnel qui n'est pas nécessairement familier avec un système THz-TDS.

0.1 Organisation de cette thèse

Cette thèse a été divisée en cinq chapitres.

Le chapitre 1 montre brièvement comment le cancer devient un problème de santé majeur et comment il motive la recherche sur l'utilisation du THz comme outil de diagnostic et de pratique thérapeutique. Ensuite, il définit la nature générale, la portée et les objectifs de ce travail et du projet de recherche dans son ensemble.

Le chapitre 2 consiste en une recension des écrits qui présente le sujet de la génération et de la détection de THz, en soulignant les propriétés de chaque technique afin de déterminer laquelle convient le mieux à l'application prévue.

Le chapitre 3 contient une description détaillée du système, en commençant par les composants matériels, leur finalité, la façon dont ils sont assemblés et leurs relations mutuelles. La description du matériel est suivie d'une illustration détaillée du logiciel qui pilote le système. Les principaux aspects de l'architecture du programme sont examinés en fonction des avantages qu'ils procurent en matière de flexibilité du flux de travail et d'extensibilité du logiciel.

Le chapitre 4 est dédié à l'évaluation des performances du système. La qualité des mesures THz est vérifiée en utilisant notre système avec différentes valeurs de différentes variables de configuration et un échantillon composé d'un miroir, afin de déterminer quantitativement le degré de distorsion de l'impulsion THz dû à chaque mode de mesure. Dans le cas de l'imagerie par scansion raster, le miroir a été remplacé par un échantillon biologique composé de peau d'oreille porcine, choisi parce qu'il est généralement un bon substitut de la peau humaine pour la similarité respective des propriétés histologiques et physiologiques [31]. Nous avons utilisé l'échantillon pour une séance simulée de PTT afin de montrer qu'une technique basée sur le THz peut être un complément précieux pour surveiller la séance de traitement et effectuer des vérifications diagnostiques par la suite.

Enfin, au chapitre 5, nous présentons nos conclusions, illustrant ce qui a été mis en œuvre dans le système et quelles sont ses capacités attendues, compte tenu des résultats de notre test sur la peau porcine. Nous proposons également des moyens d'améliorer le système afin de faciliter et de permettre des études plus détaillées sur les échantillons biologiques, d'améliorer notre capacité à traiter les données au cours de la mesure, afin de donner une rétroaction précieuse à l'opérateur en temps réel et faire du système un outil thérapeutique viable.

0.2 Introduction au Térahertz

La locution rayonnement térahertz (Terahertz radiation, THz ou Térahertz) est le nom conventionnel de la région du spectre EM comprise dans la gamme de $0.1\,\mathrm{THz}$ à $10\,\mathrm{THz}$ (figure 2), qui signifie de $30\,\mu\mathrm{m}$ à $3000\,\mu\mathrm{m}$ en termes de longueur d'onde et qui correspond à des énergies photoniques de $0.4\,\mathrm{meV}$ à $41\,\mathrm{meV}$.

Il y a plusieurs raisons pour lesquelles le THz est intéressant pour la physique et l'ingénierie ; les fréquences de rayonnement térahertz, en fait, correspondent aux transitions rotationnelles et vibrationnelles dans les molécules, les modes vibrationnels ou torsionnels collectifs [32–34] dans la matière condensée, ainsi que les excitations à basse énergie et la dynamique des vecteurs dans les matériaux électroniques [35–37].

Par conséquent, en effectuant des mesures spectroscopiques sur un échantillon, il est possible d'identifier ses composants chimiques en recherchant leur signature unique dans le spectre d'absorption, cependant, puisqu'il est situé entre micro-ondes et IR, la génération et la détection de THz posent des défis particuliers, lorsqu'elles sont abordées avec les outils et les méthodes disponibles pour les deux gammes voisines. En fait, les fréquences supérieures à 10×10^{11} Hz, dépassent les capacités de l'électronique conventionnelle (micro-ondes), tandis que les technologies optiques normales reposent sur des processus impliquant des énergies photoniques beaucoup plus élevées que l'énergie térahertz typique d'environ $1\,\mathrm{meV}$.

Cela a entravé l'adoption de solutions technologiques basées sur THz, et pendant longtemps, l'expression lacune térahertz (THz Gap, T-GAP) a été utilisée pour mettre en évidence le manque comparatif d'applications dans ce domaine de fréquence, par rapport à micro-ondes et IR.

Grâce à un effort de recherche continu pour développer des solutions *ad hoc* pour la production, la manipulation et la détection de THz, l'écart s'est constamment creusé au cours des dernières décennies, comme le développement de l'optique ultra rapide et de la physique des semi-conducteurs a permis la conception ou l'amélioration de plusieurs types de détecteurs, sources et techniques de mesure fiables (e.g. : [38–40]) qui a ouvert les possibilités intéressantes que cette gamme de longueurs d'onde a à offrir.

À cet égard, la technique appelée THz-TDS [41] rend le THz particulièrement efficace et polyvalente, car elle permet la mesure du vecteur de champ électrique ($\mathbf{E}$) plutôt que d'enregistrer son intensité ($E = |\mathbf{E}|$) comme c'est généralement le cas en optique, e.g. : avec la spectroscopie de transformation de Fourier infrarouge (Fourier Transform Infrared, FTIR) [42]. THz-TDS a été utilisé dans la caractérisation de plusieurs polymères tels que le polyéthylène, le polypropylène, le polycarbonate, etc. [43], ainsi que pour l'étude de petites bio-molécules (e.g. : acides aminés, polypeptides) [44], bio-macromolécules (e.g. :,DNA, acide ribonucléique, protéines) [45] et pour l'identification d'explosifs tels que le trinitrotoluène (Trinitrotoluene, TNT) et la Triméthylène-Trinitramine (Research Department Explosive, RDX) [46].

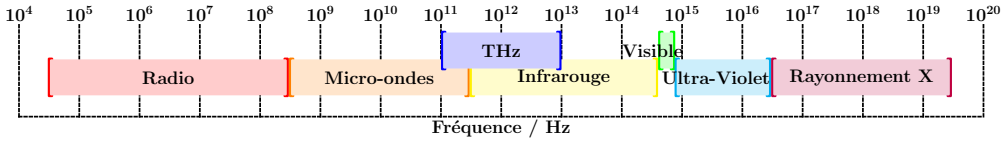

FIGURE 2 : La plage de rayonnement térahertz se situe entre les portions « infrarouge lointain » et « micro-ondes » du spectre électromagnétique.

De plus, étant donné que le THz peut être manipulé par diffraction, réflexion et réfraction, il convient pour des applications d'imagerie à une résolution typique comparable à celle de l'œil humain et le fait que plusieurs matériaux (en plus de l'air) utilisés couramment dans l'industrie, comme le plastique, le papier, la céramique, le textile et le bois [47–50] ont un assez bon degré de transparence au THz, qui permet d'effectuer des mesures sans contact sur des objets cachés et des marchandises emballées (e.g. : assurance qualité à une chaîne de production [51], diagnostic du patrimoine culturel [52]), alors que d'autres techniques établies nécessitent un contact (ultrasons), ou sont entravées par le matériau interposé (thermographie IR). Dans le cas des rayons X, le danger pour la santé dû à l'ionisation est également évité en utilisant le THz, étant donné la petite quantité d'énergie ($O(\mathrm{meV})$) transportée par ses photons. Pour sa sécurité intrinsèque, le THz est apte à sonder les tissus vivants, même si la profondeur de pénétration *in vivo* est réduite par la présence de grandes quantités d'eau par rapport au cas des diélectriques, en limitant son utilisation à des applications sous-cutanées (pour obtenir une détection à une profondeur d'environ $5\,\mathrm{mm}$, un rapport signal sur bruit de 10000 est requis [53]). Toutes ces propriétés uniques font du térahertz un candidat très attractif pour les systèmes de détection et de surveillance dans les domaines biologiques et biomédicaux, ainsi que pour les applications d'inspection, de sécurité et de défense [54–58].

De façon générale, les techniques de production et de détection se divisent généralement en trois régimes :

1. À bande étroite/onde continue (Continuous Wave, CW).
2. À large bande.
3. À bande ultra large.

Dans la première catégorie, nous avons, par exemple, les photo-mixeurs, les cristaux non linéaires (2^{de} non-linéarité) [59, 60], les lasers à cascade quantique [40] pour la production tandis que les détecteurs thermiques et les systèmes de mesure hétérodyne sont couramment utilisés pour la pièce de détection. Certaines de ces sources CW sont également adaptées à l'imagerie des ondes THz (voir [61–63]).

L'émission/détection pulsée de THz est couverte dans les deux régimes restants ; ceux-ci sont répertoriés comme cas séparés parce que les techniques employées pour mesurer le haut débit pulsé sont difficilement utilisables pour les fréquences supérieures à $4\,\mathrm{THz}$, où le rayonnement résonne avec les phonons du cristal du transducteur (par exemple, les phonons du tellurure de zinc (Zinc Telluride, ZnTe) correspondent à $5.3\,\mathrm{THz}$ [64]), et est alors fortement déformé, donc un équipement spécial est nécessaire pour traiter les signaux à très large bande.

Le rayonnement térahertz à onde continue peut être généré de plusieurs façons, par exemple le photo-mélange, également connu sous le nom de conversion optique hétérodyne vers le bas, mélange deux lasers avec des fréquences légèrement différentes (ω_1 et ω_2) à l'intérieur d'un milieu non linéaire (e.g. : photoconducteur ou supraconducteur) et utilise la fréquence de battement correspondant à la différence entre ceux des entrées ($\omega_{beat} = \omega_1 - \omega_2$) pour moduler le photo-courant dans l'appareil et générer du THz (génération de fréquence différence (Difference Frequency Generation, DFG)).

Il est possible de produire THz à onde continue[1] en utilisant la technologie laser, soit en sélectionnant un support de gain tel que capable d'émettre dans la THz, tel que CH_3F, CH_3OH, NH_3 et CH_2F_2. Par exemple, CH_3OH est capable d'émettre des lasers dans la région THz [65, 66].

Un autre moyen de gain consiste en des courants de Lorentz quantisés, produits par des champs électriques et magnétiques croisés dans un cristal de germanium dopé p à température cryogénique. [67] Ce type de source est accordable de $1\,\mathrm{THz}$ à $4\,\mathrm{THz}$ en changeant les valeurs des champs : un avantage qui compense la nécessité de la cryogénie. [68]

Une autre possibilité pour atteindre l'accordabilité est d'accélérer un faisceau d'électrons et d'utiliser soit une série d'aimants ou un réseau mécanique pour forcer une oscillation latérale du faisceau aux fréquences THz, et d'exploiter la production de *bremsstrahlung* : les aimants sont utilisés dans les installations de laser à électrons libres (Free Electron Laser, FEL) [67] (e.g. : FIREFLY, situé à Stanford CA, USA, et CLIO, situé au Laboratoire de Chimie Physique à Orsay, France), tandis que l'autre méthode en utilisée dans un oscillateur à onde rétrograde (Backward Wave Oscillator, BWO) [69].

Le dispositif appelé laser à cascade quantique (Quantum Cascade Laser, QCL) est particulièrement prometteur en tant que générateur CW. Il se compose d'un ensemble de puits quantiques couplés : l'application d'un biais approprié force les niveaux d'énergie occupés d'un puits à correspondre aux niveaux supérieurs du suivant, à faire migrer les électrons par effet tunnel, puis émettre des photons lorsqu'ils tombent au fond du puits nouvellement occupé. [70] Les propriétés de la lumière émise sont fixées par les paramètres constructifs des puits quantiques [71–74], mais la production d'une QCL serait relativement peu coûteuse si elle était produite en masse. En plus le développement de QCL travaillant à des températures de plus en plus élevées ($150\,\mathrm{K}$ est attesté dans la littérature [75]) réduit le coût de l'opération cryogénique.

[1] Ou des impulsions si longues qu'elles ne font aucune différence pratique.

Souvent, les mêmes procédés utilisés pour la production de THz peuvent également être adaptés pour la partie détection des systèmes : la détection hétérodyne est basée sur la conversion basse fréquence dans un dispositif non linéaire, par analogie à la production par photo-mélange, le rayonnement incident rayonnement térahertz (ω_{THz}) est mélangé à un rayonnement de référence (aussi appelé oscillateur local) à une fréquence fixe (I_{-}), et le courant photoélectrique qui en résulte est filtré pour ne conserver que le composant oscillant à la fréquence différence (I_{-}). L'amplitude de I_{-} est proportionnelle au produit des amplitudes de l'oscillateur local et du signal, ce qui fait E_{LO} un facteur d'amplification efficace pour E_{THz}. Certains des mélanges les plus sensibles sont les détecteurs cryogéniques à base d'antimoniure d'indium (InSb) [76] ou de niobium (Nb) et de nitrure de niobium (NbN) [77, 78].

Les systèmes de détection les plus simples pour THz à onde continue utilisent des détecteurs thermiques qui convertissent la puissance incidente THz en chaleur lue à l'aide d'un thermomètre ou qui mesurent d'autres propriétés dépendantes de la température, e.g. : résistance électrique comme dans le cas de certains bolomètres qui fonctionnent en conditions cryogéniques. Le changement de température est mesuré par un thermomètre [60, 61].

Étant donné qu'à long terme nous voulons effectuer des mesures spectroscopiques avec le système, les appareils CW ne sont pas vraiment adaptés et nous devons tenir compte du régime pulsé pour atteindre nos objectifs.

La majorité des techniques basées sur des dispositifs électroniques ou la manipulation des micro-ondes donnent lieu à des impulsions térahertz à bande étroite, obtenues par génération harmonique plus élevée [79], éventuellement avec une diode Schottky [80] ou en utilisant des schémas à plusieurs étages qui commencent par l'interaction des micro-ondes avec un laser CW [81], mais ces techniques ne peuvent générer au plus que des fréquences de quelques centaines de gigahertz.

Un moyen courant de générer des impulsions THz à large bande consiste à exploiter des cristaux optiques avec des tenseurs de susceptibilité électrique de rang supérieur non nuls ($\chi^{(n)}$). Par exemple, le tenseur $\chi^{(2)}$ d'un cristal électro-optique sans symétrie d'inversion permet le processus appelé redressement optique (Optical Rectification, OR) de sorte que chaque fréquence comprise dans une impulsion laser intense se propageant dans le cristal subira DFG, et générera une fréquence THz différente, créant ainsi une impulsion THz.

Ce mécanisme de DFG intra-impulsions est efficace seulement si les photons d'entrée et de sortie respectent les conditions de correspondance de phase $\omega_1 - \omega_2 = \Omega_{THz}$, $k_1 - k_2 = k_{THz}$. Cette condition ne peut pas être

vérifiée à la fois pour toutes les combinaisons de fréquences, et l'efficacité diminue à mesure que les photons se propagent, de telle façon que l'emploi de cristaux plus épais est inutile [82]. Comme ces méthodes reposent sur des matériaux polaires, elles sont également affectées par la résonance des phonons optiques, qui supprime l'émission dans la région $\approx 5\,\mathrm{THz}$ à $10\,\mathrm{THz}$ [83].

Les cristaux optiques sont également adaptés à la détection du rayonnement THz, bien qu'ils exploitent un phénomène différent, nommé effet électro-optique linéaire [84, chap. 11]. Il s'agit également d'un effet non linéaire de second ordre qui se manifeste par une variation de l'indice de réfraction proportionnelle à un champ électrique (presque) statique appliqué externement, tel qu'un faisceau laser qui se propage dans le cristal aura sa polarisation modifiée en conséquence. Puisque le champ électrique du THz est pratiquement constant pendant la durée des impulsions laser ultrarapides de la sonde, il joue le rôle de E_{st} et l'intensité de la SH de la sonde est modulée par l'enveloppe de l'impulsion THz. En changeant le délai relatif entre l'heure d'arrivée sur le cristal entre la sonde et le signal, il est possible de reconstruire la forme de l'impulsion THz avec une résolution élevée : c'est la base de la technique appelée THz-TDS.

Une antenne photoconductrice (Photoconductive Antenna, PCA) pour rayonnement térahertz se compose d'un film mince à semi-conducteur direct hautement résistif cultivé épitaxialement sur un substrat semi-isolant et très résistif (généralement un composé III-V comme GaAs avec dopage différent), avec deux plaquettes de contact électriques. Chaque photon dont l'énergie $\hbar\omega$ est plus grande que la bande interdite du semi-conducteur (E_g) absorbé dans le film crée une paire électron-trou dans le film qui migre ensuite vers le bas de la bande de conduction en émettant des photons THz (transitions intrabande rapides) jusqu'à la recombine des porteurs (voir figure 3a).

Ce temps de relaxation dépend de la densité des défauts de cristaux (figure 3a) et peut être fait plus court que $1\,\mathrm{ps}$ en réglant le dopage. [85, 86]. Une impulsion laser ultra-courte focalisée sur l'espace inter-électrode de la PCA génère un nuage de charge, et un biais appliqué sur les électrodes sépare les porteurs, leur donnant le temps de subir des transitions intrabande et de générer une impulsion THz (voir figure 3b).

En configuration de détection, les porteurs de charge créés par le laser de la pompe sont séparés par le champ électrique de l'impulsion THz entrante, générant un courant sur les électrodes qui peut être mesuré par un amplificateur *lock-in* (voir figure 3c). La nature ultracourte de la pompe laser permet d'effectuer THz-TDS avec PCA aussi.

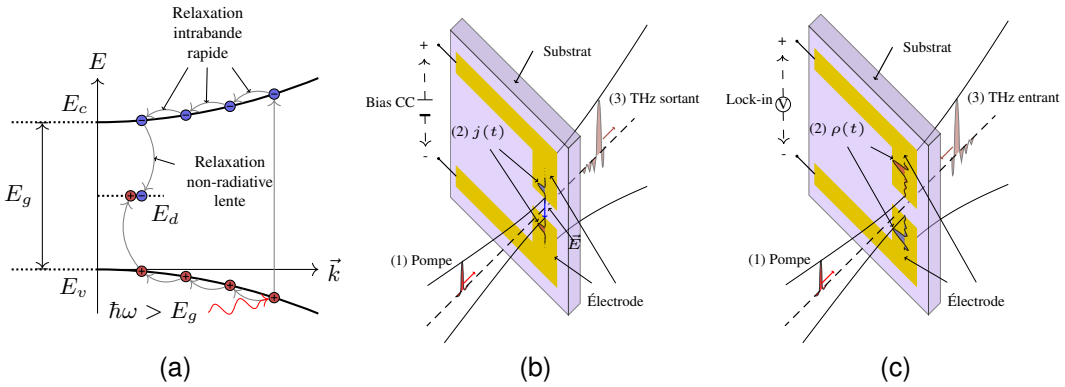

FIGURE 3 : (a) Diagramme de bande d'une PCA : les transitions intrabande rapides provoquent l'émission du signal, jusqu'à ce que la relaxation non radiative arrête le processus. (b) Diagramme schématique d'une PCA utilisé en configuration d'« émetteur » : une polarisation externe crée des séparations entre les porteurs de charge créés par le laser de la pompe, ce qui donne le temps aux transitions intrabande pour développer une impulsion THz. (c) Diagramme schématique d'une PCA utilisé en configuration de « détecteur » : le champ électrique THz sépare les porteurs produits par le laser pompe pour produire un ΔV aux bornes de la PCA, qui peut être détecté à l'aide d'un amplificateur *lock-in*.

0.3 Description du système

Puisque notre objectif à long terme est d'utiliser le système en temps réel, sur les patients oncologiques pendant le traitement, la génération et les pièces de détection doivent être compactes, mécaniquement autonomes et stables, pour faciliter le placement à proximité de la pièce traitée, l'acquisition TDS doit être effectuée le plus rapidement possible.

La première exigence signifie que nous devons utiliser des PCA, même si la largeur de bande des impulsions sera limitée à environ $4\,\mathrm{THz}$ à $5\,\mathrm{THz}$, la seconde impose l'utilisation d'une ligne de retard capable de se déplacer très rapidement et avec précision. Néanmoins, il est également utile d'effectuer des acquisitions lentes et précises, de calibrer l'instrument ou de régler la longueur relative des branches de la pompe et de la sonde avant le début d'une session de traitement : à cet effet, une ligne de retard lente et plus longue a aussi été incluse.

En fait, les composants du système sont en grande partie ceux du *Measurement Kit for Research and Development* (MKRD) [87], commercialisés par l'entreprise canadienne TeTechS, choisis pour leur qualité et leur susceptibilité à être modifiés avec des composants personnalisés supplémentaires.

Le système de base se compose de deux boîtiers, l'un contenant le chemin optique et l'autre dédié à l'alimentation et à l'électronique de contrôle qui peuvent être interfacés avec un ordinateur portable.

La figure 4a est une photographie du chemin optique du THz-TDS prise en plongée, après la personnalisation de certains composants.

Le boîtier marqué avec F.4a-1 est le module 3.1a-1 laser de banc fournissant des faisceaux d'excitation pour actionner les antennes : il a une longueur d'onde de $785\,\mathrm{nm}$, puissance de sortie moyenne de $40\,\mathrm{mW}$ à une fréquence de répétition des impulsions (pulse repetition frequency, PRF) de $100\,\mathrm{MHz}$, et une largeur d'impulsion nominale de $100\,\mathrm{fs}$.

Le diviseur de faisceaux marqué F.4a-2 sépare le laser en deux faisceaux égaux qui sont acheminés à l'émetteur THz (modèle T-Era-100A-800-air) sur la branche THz, et au récepteur (modèle T-Era-20D40P-800-air) sur la branche de sonde et marqués respectivement F.4a-3 et F.4a-4.

Après l'émetteur, la branche THz propage les impulsions THz au récepteur via une série de miroirs paraboliques hors axe et comprend deux porte-échantillons pour les mesures en transmission et en réflexion (situés respectivement à F.4a-5 et F.4a-6). La branche de la sonde s'assure que le laser atteint l'arrière du récepteur « à temps » avec le signal, où il fournit une fenêtre de temps de $100\,\mathrm{fs}$ pour échantillonner une section de l'impulsion THz. La ligne à retard lente (slow delay line, SDL) placée en marque F.4a-8 est utilisée pour effectuer des mesures TDS précises : elle se compose d'un étage de translation motorisée Zaber (modèle T-LSM050A), avec une plage de déplacement de $5\,\mathrm{cm}$ et une résolution spatiale de $0.1\,\mu\mathrm{m}$, permettant de modifier en toute sécurité la position temporelle relative de THz et les impulsions de la sonde par pas de $5\,\mathrm{fs}$.

Une des améliorations requises par notre application est la ligne à retard rapide (fast delay line, FDL) placée dans la branche de la sonde en marque F.4a-7. Il s'agit d'un oscillateur actionné magnétiquement qui peut effectuer plusieurs balayages par seconde par opposition à la SDL marqué avec F.4a-8, ce qui prend au mieux quelques minutes pour effectuer une scansion[2]. Les deux lignes de retard mettent l'accent sur différents aspects de la mesure : la SDL permet de longs balayages avec des lectures précises du champ THz, ce qui permet une représentation plus fidèle et détaillée des caractéristiques temporelles et spectrales des impulsions, alors que le FDL sacrifie une certaine précision et se concentre sur le type d'opération rapide nécessaire pour l'application prévue.

[2]La FDL montrée en figure 4a a été nsuite remplacée par un modèle différent, sans que cela n'ait d'effet sur l'argument du paragraphe actuel.

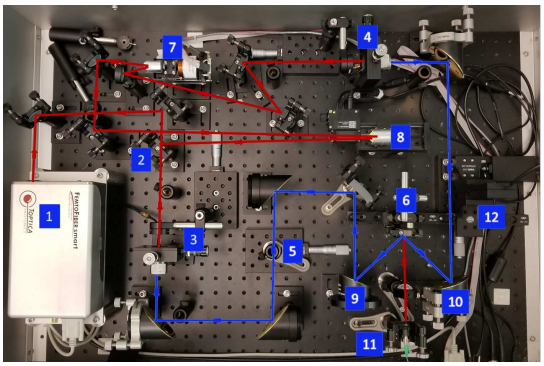

(a)

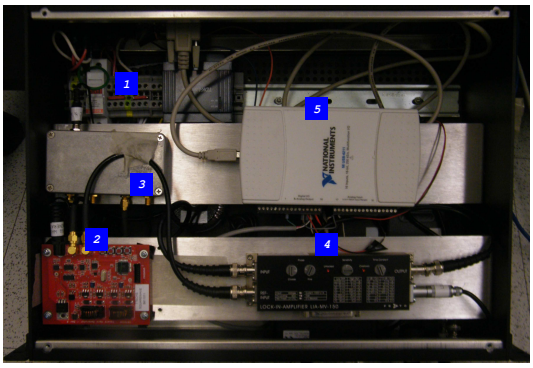

(b)

(c)

FIGURE 4 : (a) Vue en plongée du système TeTechS. a-1: Laser femtoseconde. a-2: Diviseur de faisceaux. a-3: Émetteur THz. a-4: Détecteur THz. a-5: Support d'échantillon en géométrie de transmission. a-6: Support d'échantillon en géométrie de réflexion. a-7: La ligne à retard rapide (fast delay line, FDL). a-8: La ligne à retard lente (slow delay line, SDL). a-9, a-10: Miroirs dorés et hors-axe à 45°. a-11: Diode laser NIR. a-12: Étage motorisé en deux dimensions pour imager. (b) Vue supérieure du boîtier de commande TeTechS. b-1: Bloc d'alimentation (en arrière-plan). b-2: Générateur d'impulsions carrées pour synchroniser la tension de polarisation et la référence pour le *lock-in*. b-3: Amplificateur qui transforme l'onde carrée en tension de polarisation. b-4: Amplificateur *lock-in* intégré. b-5: Module boîtier d'acquisition (Data Acquisition, DAQ) USB de NI, pour l'acquisition de signaux et le commande de la FDL. (c) Vue du panneau avant du boîtier de commande TeTechS. c-1: Interrupteur de sécurité et bouton de réglage du module laser marqué a-1 dans la figure. c-2: Sortie USB pour connecter le DAQ à un ordinateur. c-3: Sortie d'impulsions carrées de référence pur un instrument externe optionnel. c-4: Sortie de signal pour l'utilisation avec un amplificateur *lock-in* externe optionnel.

Les miroirs paraboliques marqués F.4a-9 et F.4a-10 ont été ajoutés pour livrer la THz sur l'échantillon et capter la réflexion à un angle de $45°$, tout en laissant une ligne de vision claire devant le porte-échantillon pour le laser en proche infrarouge (near infrared, NIR) marqué F.4a-11, utilisé pour simuler la PTT sur nos échantillons. Le porte-échantillon lui-même est monté sur un étage motorisé X-Y (au marque F.4a-12)[3] spécifiquement ajouté pour effectuer des scansions raster de la zone cible et obtenir un mappage des zones qui ont été chauffées, avec une analyse spectrale complète effectuée à chaque pixel de l'acquisition.

En figure 4b et 4c, sont montrées une vue du dessus et du panneau avant du boîtier de commande. L'unité d'alimentation est intégrée et est visible sous le reste de l'équipement à la marque F.4b-1. Pour assurer la sécurité, la ligne d'alimentation laser contient un bouton de régulation et deux interrupteurs supplémentaires (l'un fonctionnant à l'aide d'une clé) sur le panneau avant, marqués par F.4c-1. Le panneau rouge marqué avec F.4b-2 émet un train continu d'impulsions carrées unipolaires, réparties sur deux sorties. Le premier est amplifié par le module marqué avec F.4b-3 pour fournir une polarisation intermittente à l'émetteur qui allume et éteint l'antenne à chaque impulsion, ainsi modulant la sortie et servant de hachoir électronique. Le second train d'impulsions est envoyé à l'amplificateur *lock-in* intégré pour être utilisé comme oscillateur de référence.

Normalement, nous utilisons la polarisation à une PRF de ~$1.314\,159\,\mathrm{kHz}$, avec une valeur de crête correspondant à celle requise par l'antenne, à savoir $\pm 50\,\mathrm{V}$ pour le T-Era-100A-800-air, mais la carte a des boutons qui permettent le réglage des paramètres d'impulsions carrées. Le *lock-in* (marqué avec F.4b-2) est directement relié à l'antenne du récepteur via le connecteur du panneau avant marqué F.4c-4 et utilise la polarisation de l'émetteur comme fréquence de référence.

Étant donné que la PRF de la sonde est beaucoup plus élevé que celui de la polarisation, chaque cycle de polarisation produit une moyenne de plusieurs impulsions et produit une tension proportionnelle au champ THz à l'intérieur de la fenêtre de temps de $100\,\mathrm{fs}$, qui est redirigée vers une carte boîtier d'acquisition (Data Acquisition, DAQ) produite par National Instruments (NI), marqué avec F.4b-5 et géré par un ordinateur portable via le port USB au marque F.4c-2.

Le *lock-in* intégré peut également être facilement contourné pour uti iser un module externe à sa place, chaque fois qu'une meilleure performance est requise dans une mesure. En fait, nous avons utilisé un Stanford Technology

[3] L'étage X-Y est composé par deux étages produites par Thorlabs qui sont assemblés à ang : un MTS25B-Z8 avec une plage de déplacement de MTS25B-Z8 en direction X et un MTS50B-Z8 avec une plage de déplacement de $5\,\mathrm{cm}$ en direction Y.

SR865 comme *lock-in* externe pour exploiter sa haute sensitivité ($1\,\mathrm{nV}$) et son faible bruit ($2.5\,\mathrm{nV\,Hz^{0.5}}$ à $1\,\mathrm{kHz}$ avec une plage d'entrée de $10\,\mathrm{mV}$) pour établir la réponse « réelle » des nôtres détecteurs.

TeTechS a fourni un programme écrit an utilisant le langage LABVIEW (ce qu'on appelle un instrument virtuel (Virtual Instument, VI)) pour faire fonctionner le système et a fourni les fonctionnalités de base pour positionner le SDL, pour effectuer un scan et l'enregistrer ou, en alternative, pour enregistrer un nombre indéterminé de scans ultérieurs dans le même fichier.

À l'origine, ce logiciel était destiné à être utilisé dans des mesures de routine pour la caractérisation des matériaux ou pour effectuer des contrôles ponctuels dans une chaîne de production, cependant, le type de mesures que nous effectuons quotidiennement exige une plus grande flexibilité de fonctionnement et la capacité de traiter un volume de données beaucoup plus élevé que celui envisagé par le développeur initial.

En inspectant le code source, nous avons identifié plusieurs pistes d'amélioration possibles et nous avons procédé à la mise en œuvre de celles qui étaient jugées plus utiles pour nous à l'heure actuelle[4]

Tout d'abord, nous avons cherché le code répété et l'avons factorisé dans un ensemble de routines bien définies (sub-VI), en particulier pour l'interface avec les moteurs. Nous avons identifié quelques domaines clés où les sub-VIs seraient bénéfiques, et construit des bibliothèques dédiées correspondantes : `zaber_wrapper` et `thorlabs_wrapper`, pour un fonctionnement facile des moteurs Zaber et Thorlabs, respectivement, `data_manipulation` qui encapsule les opérations génériques sur les données qui sont utilisées plus souvent, `save_load_data` pour l'écriture et la lecture de données vers et depuis le disque dur, `graph_handling` pour simplifier la gestion des zones de tracé et `utilities` pour ces VISs qui ne cadrent pas bien dans aucun des précédents.

La première phase, n'a pas changé le comportement ou les caractéristiques de l'ensemble du logiciel d'aucune façon, mais le rend beaucoup moins complexe, visiblement plus réactif et plus propice à d'autres modifications. Nous avons identifié six tâches réalisées par le logiciel que nous voulions améliorer et étendre :

1. l'interface utilisateur,
2. le traçage des données,
3. l'écriture des données sur le disque,

[4]Nous avons inspecté et modifié le logiciel original en vertu de l'accord que toutes les améliorations seraient mises à la disposition de TeTechS pour utilisation dans les versions subséquentes.

4. la procédure d'acquisition lente,
5. la procédure d'acquisition rapide,
6. la procédure de scansion d'image.

Les tâches liées à l'UI sont clairement la responsabilité du programme principal, mais chacune des autres peut être traitée indépendamment dans une large mesure : par exemple, la façon dont les données d'une acquisition sont tracées dépend peu de la façon dont elles sont mesurées. LABVIEW a la particularité que toutes les boucles de haut niveau et les sub-VIs sont exécutées en même temps pourvu que toutes les entrées initiales nécessaires sont disponibles, donc nous avons utilisé la stratégie de dédier une boucle ou un sub-VI à chaque tâche et avons défini un protocole strict pour l'échange de données entre les tâches au moment de l'exécution. La communication a été mise en place en utilisant la combinaison de références aux éléments de l'UI et les queues de messages comme entrée initiale dans les différents modules du programme : les références permettent aux sub-VIs d'accéder directement au même contrôle de l'UI principale, tandis que les queues fournissent un mécanisme standard pour envoyer des données ou des instructions d'un sub-VI à un autre. Les sub-VIs qui traitent les données (e.g. : écriture et traçage des données) sont implémentés comme des automates finis qui attendent de recevoir des instructions de l'une des queues et les exécutent ensuite. Une instruction est assemblée dans l'un des sub-VIs qui produisent des données (e.g. : les procédures de scansion) et consiste en général en un code qui identifie une opération et les données sur lesquelles opérer. Cette architecture fournit au programme un degré élevé de flexibilité qui permet de changer (ou de corriger) la manière d'effectuer n'importe quelle opération avec un impact minimal sur toutes les autres parties du logiciel, et a joué un rôle déterminant dans l'amélioration des performances de l'ensemble du système (e.g. : accélération de la scansion d'image à environ 1000 pixels en $22\,\mathrm{min}$).

0.4 Évaluation des performances du système

Pour établir la sensibilité du *lock-in* qui correspond le mieux au pic THz non perturbé à la pleine échelle de sa limite de sortie analogique de $10\,\mathrm{V}$, nous avons utilisé la SDL pour effectuer une mesure à très faible vitesse $v_{dl} = 0.1\,\mathrm{mm\,s^{-1}}$, et temps d'intégration extrêmement élevé $t_{int} = 30\,\mathrm{ms}$. Le long temps d'intégration réduit l'effet du bruit aléatoire, tandis que la faible vitesse minimise le mélange des données des parties adjacentes de l'impulsion causée par l'interaction entre le temps d'intégration et la vitesse discutée en détail à la page 47.

Figure 7 montre la mesure qui correspondait le mieux au pic et à la plage de sortie : le spectre dans le panneau inférieur s'est bien comporté jusqu'à presque 2 THz, en dehors des lignes d'absorption dues à l'atmosphère non purgée. Si nous utilisons $i_{sens} = 10\,\mathrm{nA}$ comme valeur standard pour la sensitivité du *lock-in*, la valeur de crête mesurée devrait être inférieure à toute autre vitesse d'acquisition. Une vitesse minimum arbitraire de $v_{dl} = 1\,\mathrm{mm\,s^{-1}}$ a été choisie pour maintenir le temps d'acquisition sous un délai raisonnable lors de l'opération sur un patient.

Pour estimer une recommandation de t_{int}, nous avons effectué une série de mesures, pour balayer les valeurs de t_{int} permises par le SR865 tout en maintenant les i_{sens} et v_{dl} à leur valeur standard et évaluer certaines propriétés des impulsions comme indicateurs de l'altération induite par le paramètre changeant, à savoir : le décalage du signal, la valeur maximale de crête d'impulsion, la position et la largeur à mi-hauteur (Full Width at Half Maximum, FWHM), le bruit d'obscurité (Dark Noise, DN) et la gamme dynamique (Dynamic Range, DR) de l'instrument.

Les résultats de la scansion paramétrique sont indiqués dans la figure 5. Comme prévu, toutes les quantités dépendent de la valeur de t_{int} différemment, mais il y a une plage de $100\,\mu\mathrm{s}$ à $1000\,\mu\mathrm{s}$ (ombrée à la figure 5) qui semble fournir les meilleurs résultats, par conséquent nous avons adopté t_{int} = 100 µs comme valeur à utiliser par défaut.

Pour évaluer la performance de la FDL, nous avons de nouveau mesuré la THz réfléchie par le miroir, en utilisant la valeur par défaut t_{int} et i_{sens}, tout en faisant varier la fréquence de balayage (Scan Repetition Frequency, SRF) dans la plage de 1 Hz à 10 Hz.

La comparaison entre quelques traces significatives et la référence est affichée à la figure 7. La déformation de l'impulsion produite par la vitesse plus élevée de la ligne à retard rapide n'est pas très prononcée à faible SRF : pour ν_{PRF} = 1 Hz, il n'y a qu'une diminution de la hauteur et de la largeur de l'impulsion, en raison des valeurs de la première vallée, qui se mélangent avec le pic principal.

La différence augmente progressivement dans la région oscillante à la queue de la trace (voir l'insert dans la figure 7) ainsi qu'avec des valeurs croissantes de ν_{PRF}, cependant la forme générale des spectres semble être raisonnablement préservée, au moins jusqu'à ν_{PRF} = 5 Hz (groupe normal). À partir de ν_{PRF} = 6 Hz (groupe anormal), les traces sont déformées plus que ce qu'on pourrait attendre de la plus grande vitesse de scansion ν_{PRF}, en tant que le spectre gagne des caractéristiques parasites au-dessus de $0.8\,\mathrm{THz}$.

Ce comportement a été vérifié jusqu'à 19 Hz, la fréquence de résonance du miroir oscillant du ScanDelay USB, cependant, pour ν_{PRF} = 10 Hz la trace et le spectre reviennent à suivre la tendance attendue observée dans

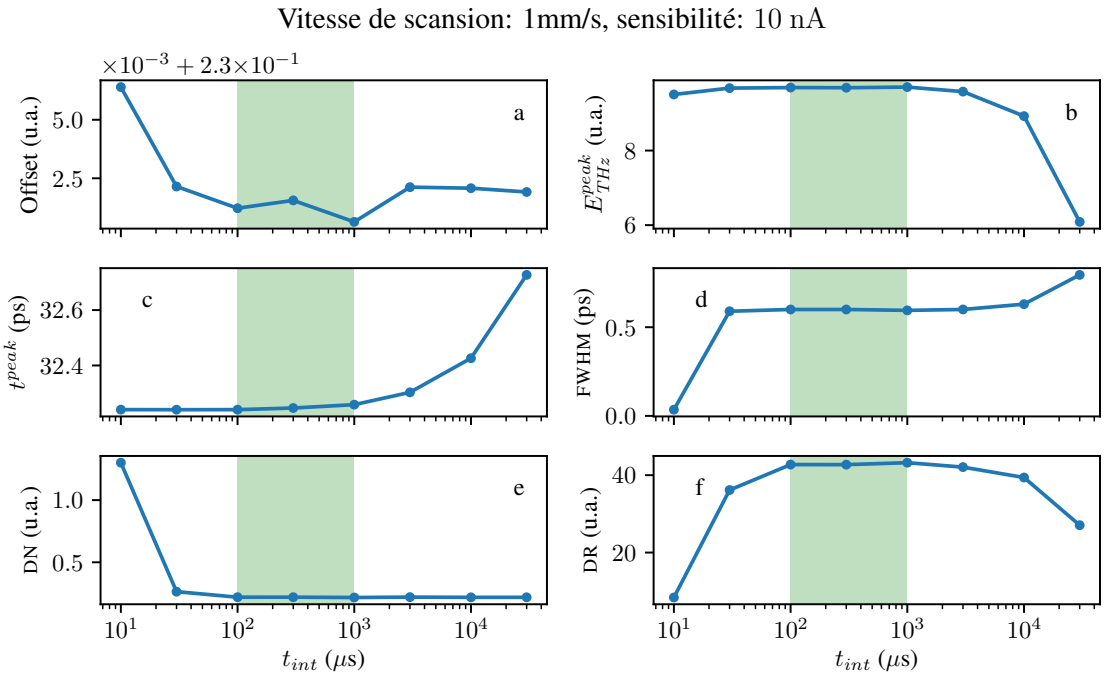

FIGURE 5 : Tracés du décalage du signal ***a***, de la valeur maximale du pic d'impulsion ***b***, de la position ***c*** et de la FWHM ***d***, du bruit d'obscurité (Dark Noise, DN) ***e*** et de la gamme dynamique (Dynamic Range, DR) ***f*** pour les traces prises avec t_{int} allant de 10 µs à 10 000 µs. La plage ombrée en vert est considérée comme optimale pour le fonctionnement réel.

le groupe régulier, sauf que la position du pic dérive linéairement avec le temps. Une explication possible est que, au-delà de 5 Hz, l'oscillateur mécanique amorti constitué par le miroir et son montage à ressort, ne suit pas le stimulus électromagnétique fourni par le contrôleur, et les échantillons sont assignés au mauvais délai : dans le cas de 10 Hz, le mouvement réel est plus similaire à celui attendu et une dérive seulement vient à être observée. Une autre hypothèse sous enquête active est qu'un bogue subtil dans le sub-VI qui configure le FDL provoque une distorsion dans l'horloge de référence utilisée pour actionner le stimulus électrique. Étant donné que la dérive est constante, il serait possible de la corriger avec un coût de calcul minimal dans le logiciel lui-même.

Enfin, nous avons effectué la simulation d'une séance de thérapie photothermique (Photothermal Therapy, PTT) sur un échantillon de peau d'oreille de porc, lequel est reconnu comme un bon modèle clinique pour la peau humaine. [31]

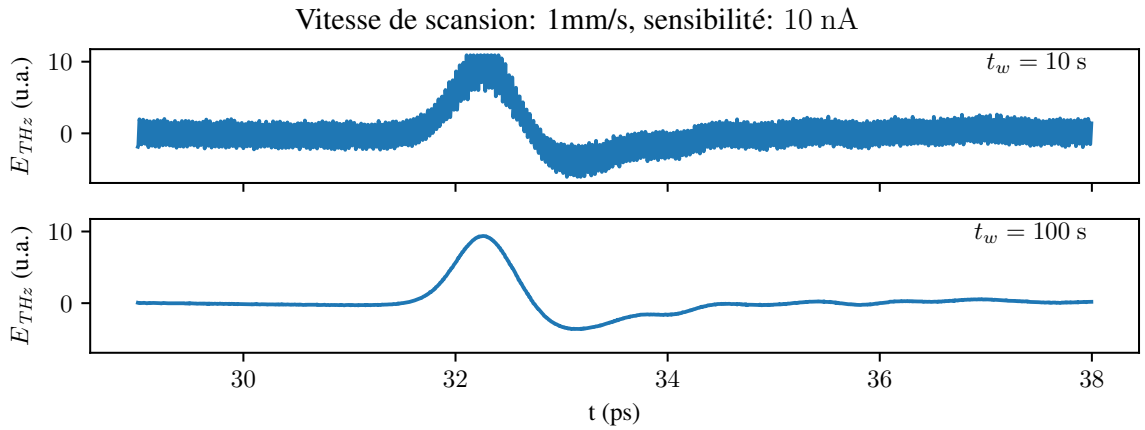

FIGURE 6 : Comparaison entre les acquisitions réalisées avec t_{int} égale à 10 µs et 100 µs. Le plus petit t_{int} n'est pas capable de filtrer le bruit, à tel point que, dans le panneau supérieur, les fluctuations au pic du signal tombent hors de l'échelle (> 10 V). Le plus grande t_{int} utilisé pour la trace dans le panneau inférieur est celui que est sélectionné par défaut dans le logiciel.

L'échantillon a été injecté dans sa partie centrale avec 50 µl d'une suspension de nanotiges d'or (Gold Nanorods, GNR), qui a ensuite été éclairée à l'aide d'une diode laser de 786 nm et puissance moyenne de 650 mW, livré sur une série de points disposés sur trois lignes de neuf points chacune, en utilisant la fibre, couplée à la diode par le producteur.

Chaque point irradié a été surveillé à l'aide de notre appareil opérant en mode d'acquisition rapide, pendant toute la durée de l'exposition au laser. Les discontinuités des tracés identifient clairement les données appartenant à chacun des neuf points d'irradiation (1 mm entre chaque deux points voisins), et il y a un comportement commun au centre et au fond, en ce sens que la THz réfléchie augmente en fonction de la température, puis se stabilise ou augmente légèrement en raison de la diminution de l'hydratation de l'échantillon, causée par la chaleur [88].

Au début de la ligne de scansion du milieu (premier point de chauffage), la réflectivité enregistrée est beaucoup plus grande, augmente un peu et tombe ensuite fortement à une valeur qui est approximativement respectée dans les points d'irradiation suivants. Il est probable que la forte diminution est causée par la perte rapide d'eau subie lorsque la température commence à monter sur le premier point : tenant compte de la durée relativement longue de l'exposition (120 s), cette déshydratation peut affecter les zones voisines et changer leur réponse. Les irrégularités dans la structure de l'échantillon cutané et l'inhomogénéité dans la diffusion des GNR

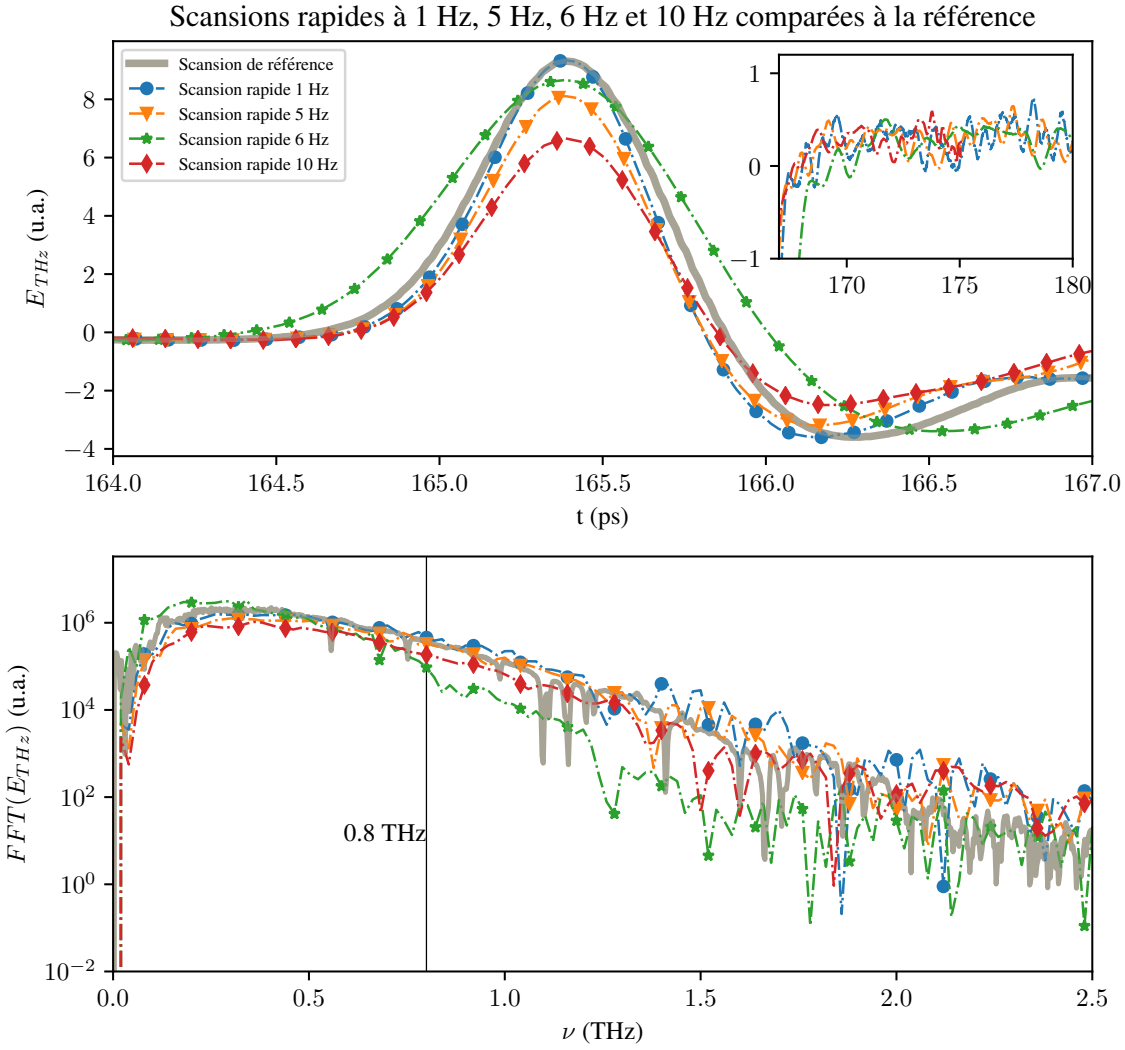

FIGURE 7 : Comparaison entre la mesure de référence effectuée avec la SDL et les acquisitions rapides : pour plus de clarté, seules les acquisitions effectuées à 1 Hz, 5 Hz, 6 Hz et 10 Hz sont signalées et les tracés ont été décalés dans le temps de façon que les positions des pics soient les mêmes. L'accord se détériore progressivement avec des fréquences d'acquisition plus élevées qui sont associées à des t_w, plus longs, jusqu'à 5 Hz. Les mesures à partir de 6 Hz à 9 Hz sont visiblement pires que prévu après avoir tenu compte de l'augmentation de t_w, avec des caractéristiques parasites apparaissant juste au-delà de 0.8 THz, mais à 10 Hz le résultat est compatible avec ceux des fréquences de scansion inférieures.

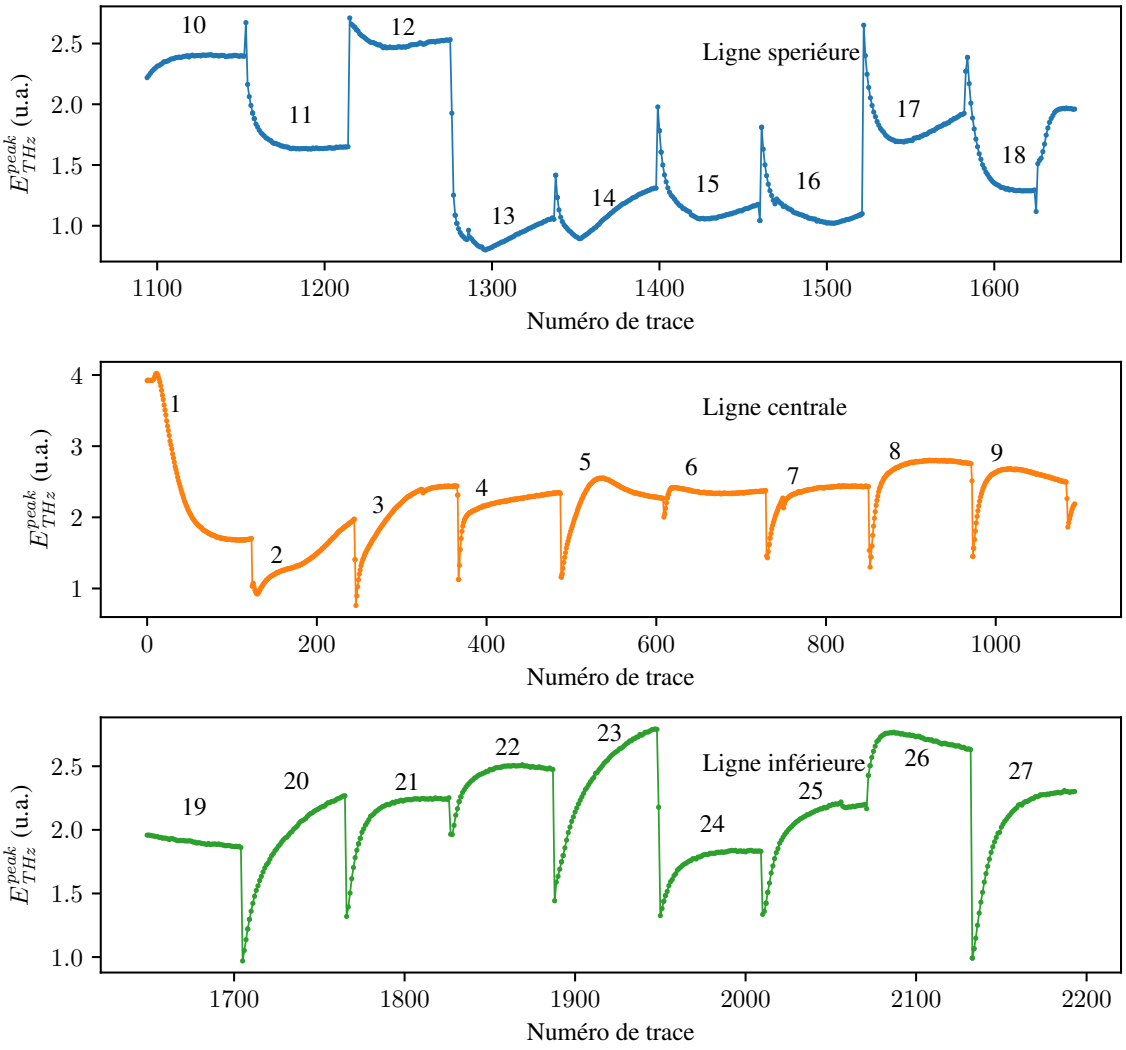

FIGURE 8 : Valeur de crête des traces THz prélevés pendant l'irradiation de l'échantillon de peau de porc. Les trois tracés correspondent à l'irradiation sur les trois lignes : supérieure, centrale et inférieure. Notez que la ligne centrale a été mesurée en premier, suivie dans l'ordre par les lignes supérieure et inférieure, d'où les traces dans les axes abscisses. Les groupes de traces liés à chaque position sont clairement identifiables (marqués avec leur ordre de'irradiation dans la figure) et montrent un bon degré de cohérence dans leur évolution dans le temps : la différence observée à la première position dans la ligne du milieu peut s'expliquer par l'apparition de la déshydratation. Les irrégularités des points de la ligne supérieure doivent faire l'objet d'une enquête plus approfondie, au-delà de la portée de cette thèse.

injectée expliquent le reste de la variabilité.

Le comportement de la ligne supérieure est plus complexe que les autres : la plupart des points d'irradiation présentent une nette diminution initiale de la réflectivité, avec une légère augmentation dans la seconde moitié de l'exposition. Cela pourrait être interprété de la même façon que le premier point d'irradiation (diminution rapide de l'hydratation), mais c'est tellement différent, par rapport aux autres, que des recherches plus approfondies, au-delà de la portée de ce travail, seraient nécessaires.

Après la simulation de la session PTT, l'échantillon de peau a été visiblement brûlé dans la zone irradiée, comme le montre figure 4.10, panel ***a***, et a été inspecté à nouveau à l'aide du module **`Image_scanner`** couvrant la zone irradiée avec une grille de pixels 40×34, récupérer une image des dimensions$19.5\,\mathrm{mm} \times 16.5\,\mathrm{mm}$, où chaque pixel est une acquisition a TDS de la acfr-thz réfléchie de l'échantillon. Pour identifier les positions où la peau avait été altérée, et dans quelle mesure, nous avons identifié le pic principal et les vallées qui le précèdent (avant) et le suivent (queue), et pour chacun nous avons évalué la valeur du champ électrique (E^{peak}_{THz}, E^{front}_{THz}, E^{tail}_{THz}) et la largeur correspondante du trait (Δt^{peak}, Δt^{front}, Δt^{tail}) comme expliqué en figure 4.10, panel ***b***, et en utilisant chaque paramètre, nous avons produit une image de l'échantillon.

Les données de magnitude de champ semblent suivre la même tendance générale, avec E^{front}_{THz} (panel ***e***) fournissant un contraste majeur que E^{peak}_{THz} (panel ***f***) et E^{tail}_{THz} (panel ***g***) produisant des images de la brûlure globalement moins reconnaissables. Toutefois, les informations fournies par le pic principal et la vallée d'attaque semblent être plus complémentaires que celles obtenues par les largeurs d'impulsion, et E^{tail}_{THz} donne une image remarquablement similaire au rapport $\Delta t^{front}/\Delta t^{tail}$ du panel ***d***. Dans le panel ***h*** s'affiche la valeur de crête à crête de l'impulsion THz, définie comme suit :

$$E^{pk2pk}_{\mathrm{THz}} = E^{peak}_{\mathrm{THz}} - \min\left(E^{front}_{\mathrm{THz}}, E^{tail}_{\mathrm{THz}}\right). \tag{1}$$

La valeur de crête à crête ne semble pas très efficace pour améliorer l'image par rapport aux autres paramètres liés au champ, en fait elle n'est que légèrement plus définie que la valeur de pic principale. Toutes les images du panel ***e*** au panel ***h*** ont une tache particulièrement lumineuse juste à droite de la zone brûlée, qui est trop loin du support pour en être la cause : il peut s'agir d'une irrégularité de l'échantillon de peau en question ou d'un artefact causé par un mauvais alignement local.

Enfin, puisque chaque pixel contient toutes les informations spectrales portées par le THz, nous avons également évalué la transformée de Fourier $\hat{F}$ de chaque trace (pixel) et comparé ses valeurs à certaines fréquences sélectionnées. Les grandeurs de la transformation à ν = 0.5 THz, 0.75 THz et 1 THz sont affichées dans les panneaux ***i***, ***j*** et ***k***, tandis que le panel ***l*** rapporte l'intégrale de la magnitude de 0.4 THz à 0.7 THz : toutes les images identifient clairement la zone brûlée avec un bon contraste, bien que se rapprochant de 1 THz l'image devient plus faible et plus difficile à distinguer par rapport à la tache lumineuse déjà observée dans les panneaux de ***e*** à ***h***. Le spectre intégré du panel ***l*** n'est pas très différent des valeurs à 0.5 THz, ce qui indique que les composants spectraux à des fréquences plus élevées ne sont pas suffisamment intenses pour influencer le résultat d'une approche aussi simple. Pour exploiter pleinement les capacités spectrales du système, il est nécessaire de mettre en œuvre une fonction de pondération appropriée.

En outre, une méthode d'atténuation du point chaud observé dans le domaine du temps et de la fréquence via le logiciel est nécessaire : même si ce n'était qu'un artefact dû à l'alignement ou à l'irrégularité de la peau, l'enlever en ajustant le système ne serait pas une solution viable pour une machine en utilisation clinique

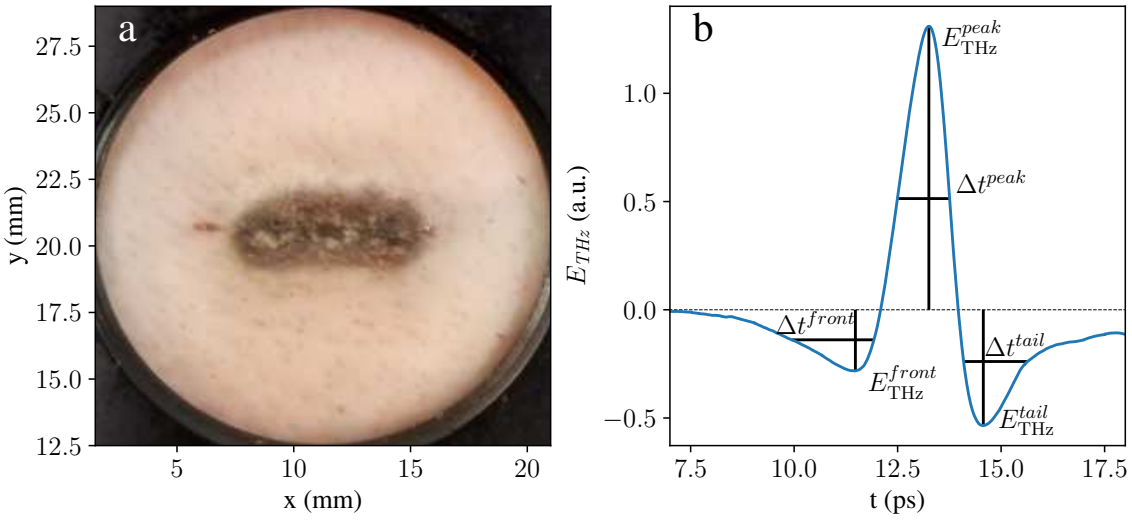

FIGURE 9 : ***a*** Photographie de l'échantillon de peau après irradiation. ***b*** Définitions des paramètres de forme extraits par les traces mesurées par **`Image_scanner`** : les amplitudes du pic principal (E^{peak}_{THz}), de la vallée d'attaque (E^{front}_{THz}) et de la première vallée de fuite (E^{tail}_{THz}), ainsi que leur largeur d'impulsion respective (Δt^{peak}, Δt^{front} and Δt^{tail}).

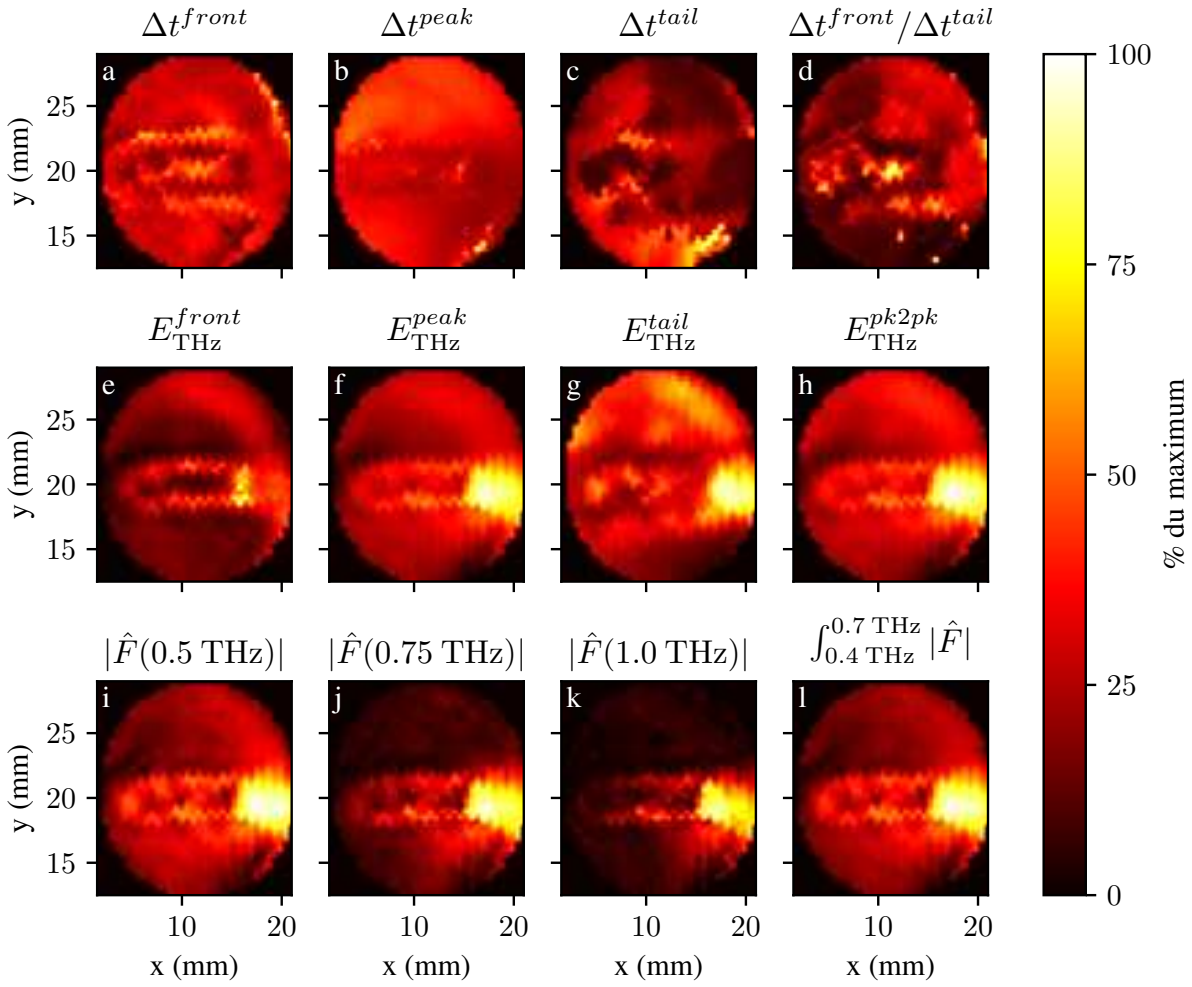

FIGURE 10 : Imagerie de l'échantillon de peau à l'aide de diverses propriétés des impulsions THz réfléchies. ***a*** Largeur de la vallée d'attaque (Δt^{front}), ***b*** largeur du pic principal (Δt^{peak}), ***c*** largeur de la première vallée de fuite (Δt^{tail}), ***d*** rapport entre les largeurs de la vallée d'attaque et de la vallée de fuite ($\Delta t^{front}/\Delta t^{tail}$), ***e*** amplitude du champ à la vallée d'attaque (E^{front}_{THz}), ***f*** amplitude du champ au pic principal (E^{peak}_{THz}), ***g*** amplitude du champ à la première vallée de fuite (E^{tail}_{THz}), ***h*** valeur crête à crête de l'impulsion THz (E^{pk2pk}_{THz}), ***i*** densité spectrale à 0.5 THz, ***j*** densité spectrale à 0.75 THz, ***k*** densité spectrale à 1 THz, ***l*** intégrale de la densité spectrale de 0.4 THz à 0.7 THz.

active, puisque la répétition de l'acquisition prendrait environ $20\,\mathrm{min}$ après chaque réglage. Par conséquent, nous proposons comme développement futur la définition d'une procédure de préparation d'« échantillon » qui minimise l'apparition de ces artefacts et la mise en œuvre d'un algorithme d'analyse capable d'atténuer leur impact, sans nécessiter une répétition de la procédure d'acquisition.

D'autre part, même les images obtenues avec des approches simples semblent capables d'identifier les altérations de la peau dû au processus de chauffage, non seulement dans la zone directement irradiée, mais aussi dans le voisinage immédiat, comme le montre la comparaison des résultats de la figure 10 avec la photographie de l'échantillon brûlé à la figure 9.

0.5 Conclusion et perspectives

La prise d'importance du cancer parmi les causes de décès dans les pays industrialisés comme le Canada n'est que la sonnette d'alarme de la tendance observée dans le monde entier. Bien que cette importance soit en grande partie attribuable à l'augmentation de la durée de vie prévue à mesure que de nouveaux remèdes améliorés pour d'autres maladies sont trouvés, les coûts économiques, sociaux et psychologiques associés au cancer et à son traitement sont très élevés et en augmentation.

À ce jour, une part importante des techniques thérapeutiques du cancer provient de la physique plutôt que de la pharmacologie, e.g. : radiothérapie, thérapie photodynamique and thérapie photothermique (Photothermal Therapy, PTT). Ce dernier, d'un intérêt particulier pour les cancers de la peau, exploite l'excitation plasmonique de nanoparticules via un laser IR pour fournir sélectivement la chaleur dans le tissu cancéreux et bénéficierait d'une technologie capable de surveiller la température atteinte dans la zone traitée, d'évaluer l'efficacité du processus et de limiter les dégâts aux cellules saines à proximité.

Dans ce travail, nous avons développé le prototype d'une installation optique qui utilise le rayonnement THz comme sonde pour mesurer, en temps réel, la température et l'hydratation de la peau d'un patient traité par PTT. Notre système est destiné à être utilisé simultanément avec la PTT comme un moniteur sans contact de l'état de la peau traitée et comme un outil de diagnostic *a posteriori* pour évaluer les dégâts livrés à la tumeur.

Puisque le but ultime est de voir cette machine utilisée sur des patients réels, dans le développement de notre validation de principe, notre principal objectif était d'équilibrer la précision de la mesure avec la vitesse de

l'ensemble de la procédure, afin de réduire au minimum l'inconfort du patient et de rendre toute la séance de traitement aussi efficace que possible. Le système utilise deux lignes de temporisation fonctionnant à des vitesses différentes. La ligne à retard rapide (fast delay line, FDL) est celle destinée à effectuer des acquisitions sur des patients au cours des séances de PTT et à prendre des images diagnostiques de la zone traitée par la suite : il est capable de prendre jusqu'à dix traces THz complètes par seconde en utilisant l'oscillation de rétro-réflecteur 5 Hz (mode bidirectionnel), bien que, puisque le déplacement dans des directions opposées provoque des distorsions différentes sur la trace mesurée, les impairs (vers l'avant) et même (vers l'arrière) numérotés doivent être soumis à un traitement différent pour obtenir des résultats complètement comparables.

Une attention particulière a été accordée au logiciel utilisé pour piloter la configuration, le rendant aussi modulaire que possible, pour rendre les améliorations futures plus faciles à mettre en œuvre, et « cacher » dans des panneaux secondaires de l'UI les contrôles plus avancés qui pourraient être utiles pendant les activités de recherche, mais qui constituent une distraction pour un opérateur formé en médecine plutôt qu'en physique du THz. Le logiciel a été initialement assemblé à partir d'exemples fournis par les producteurs des pièces de matériel, mais il a été considérablement remanié pour atteindre les objectifs de modularité et de simplicité d'utilisation mentionnés ci-dessus ; cet effort a également permis d'identifier plusieurs goulots d'étranglement dans la mise en œuvre initiale, d'accélérer l'acquisition de l'ensemble des données au moins par un facteur trois, et de supprimer les instabilités qui ont causé des pannes de logiciels pendant de longues acquisitions.

Les tests effectués sur des modèles de peau de porc soumis à un traitement PTT confirment que notre système est capable de détecter, en temps réel, les changements subis par le modèle au cours de la procédure, bien que la relation entre la THz réfléchie et la température soit en quelque sorte plus complexe que prévu, parce que le changement concomitant dans l'hydratation induit des changements du signe opposé. D'autre part, l'imagerie par balayage de la zone traitée s'est révélée sensible aux dommages causés aux cellules adjacentes par l'augmentation de la température locale dans la zone contenant des GNRSs. Grâce à cela, il peut être utilisé comme un outil de diagnostic prometteur pour évaluer le succès de la session PTT, et éventuellement, pour déterminer quand cesser de délivrer l'excitation IR sur les GNR.

Le sujet le plus important pour le développement futur est l'amélioration de l'algorithme d'analyse, afin qu'il puisse traiter adéquatement les acquisitions vers l'avant et l'arrière, et lever la restriction à 5 Hz de la fréquence d'oscillation du rétro-réflecteur : cela quadruplerait effectivement le taux d'acquisition des données et permettrait

d'autres optimisations de la procédure de scansion. Par exemple, chaque ligne d'acquisition peut être mesurée sans s'arrêter à la position de chaque pixel, ce qui entraîne une accélération substantielle. Une autre possibilité intéressante est de remplacer la dernière partie des deux branches du chemin optique dans l'espace libre par des fibres optiques, de sorte que les deux antennes photoconductrices PCA peuvent être facilement placées à proximité de l'échantillon (patient) au lieu de l'inverse, comme c'est le cas actuellement.

Du côté logiciel, une amélioration significative serait de mettre en œuvre l'algorithme d'analyse de données dans un sub-VI qui peut transmettre des informations aux autres modules, et de conduire l'imagerie sur un ensemble de points adaptatif et éparse, plutôt que la grille prédéterminé courante.

En fin de compte, pour faire de cette technologie un outil efficace pour le système de santé, il est fondamental de bien comprendre la relation entre les informations que nous pouvons recueillir à partir des différentes caractéristiques du THz réfléchie et l'état de la peau observée, afin qu'elles puissent être combinées en un ou plusieurs estimateurs optimisés, capables d'évaluer l'efficacité et de suivre l'évolution du traitement en temps réel.

Bibliographie

[1] H. RITCHIE et M. ROSER : Causes of Death. https ://ourworldindata.org/causes-of-death, février 2018.

[2] A. URRUTICOECHEA, R. ALEMANY, J. BALART, A. VILLANUEVA, F. VIÑALS et G. CAPELLÁ : Recent advances in cancer therapy : An overview. *Current Pharmaceutical Design*, 16(1):3–10, janvier 2010.

[3] R. BASKAR, K. A. LEE, R. YEO et K.-W. YEOH : Cancer and Radiation Therapy : Current Advances and Future Directions. *International Journal of Medical Sciences*, 9(3):193–199, 2012.

[4] T. J. DOUGHERTY, C. J. GOMER, B. W. HENDERSON, G. JORI, D. KESSEL, M. KORBELIK, J. MOAN et Q. PENG : Photodynamic Therapy. *Journal of the National Cancer Institute*, 90(12):889–905, juin 1998.

[5] L. ZOU, H. WANG, B. HE, L. ZENG, T. TAN, H. CAO, X. HE, Z. ZHANG, S. GUO et Y. LI : Current Approaches of Photothermal Therapy in Treating Cancer Metastasis with Nanotherapeutics. *Theranostics*, 6(6):762–772, 2016.

[6] J.-E. PARK, M. KIM, J.-H. HWANG et J.-M. NAM : Golden Opportunities : Plasmonic Gold Nanostructures for Biomedical Applications based on the Second Near-Infrared Window. *Small Methods*, 1(3):1600032, 2017.

[7] PUBLIC HEALTH AGENCY OF CANADA : *Cancer in Canada - an Epidemiological Overview : A Report Based on the Cancer Incidence Atlas - Volume 2, 2000-2006.* Public Health Agency of Canada, Ottawa, ON, Ottawa, février 2014.

[8] G. URBAN, A. JACHIMOWICZ, F. KOHL, H. KUTTNER, F. OLCAYTUG, H. KAMPER, F. PITTNER, E. MANN-BUXBAUM, T. SCHALKHAMMER, O. PROHASKA et M. SCHÖNAUER : High-resolution thin-film temperature sensor arrays for medical applications. *Sensors and Actuators A : Physical*, 22(1):650–654, juin 1990.

[9] G. J. TATTERSALL : Infrared thermography : A non-invasive window into thermal physiology. *Comparative Biochemistry and Physiology Part A : Molecular & Integrative Physiology*, 202:78–98, décembre 2016.

[10] L. J. JIANG, E. Y. K. NG, A. C. B. YEO, S. WU, F. PAN, W. Y. YAU, J. H. CHEN et Y. YANG : A perspective on medical infrared imaging. *Journal of Medical Engineering & Technology*, 29(6):257–267, janvier 2005.

[11] R. USAMENTIAGA, P. VENEGAS, J. GUEREDIAGA, L. VEGA, J. MOLLEDA et F. G. BULNES : Infrared Thermography for Temperature Measurement and Non-Destructive Testing. *Sensors (Basel, Switzerland)*, 14(7):12305–12348, juillet 2014.

[12] B. B. LAHIRI, S. BAGAVATHIAPPAN, T. JAYAKUMAR et J. PHILIP : Medical applications of infrared thermography : A review. *Infrared Physics & Technology*, 55(4):221–235, juillet 2012.

[13] E. F. J. RING et K. AMMER : Infrared thermal imaging in medicine. *Physiological Measurement*, 33(3):R33–R46, février 2012.

[14] D. JAQUE, B. del ROSAL, E. M. RODRÍGUEZ, L. M. MAESTRO, P. HARO-GONZÁLEZ et J. G. SOLÉ : Fluorescent nanothermometers for intracellular thermal sensing. *Nanomedicine*, 9(7):1047–1062, mai 2014.

[15] X.-d. WANG, O. S. WOLFBEIS et R. J. MEIER : Luminescent probes and sensors for temperature. *Chemical Society Reviews*, 42(19):7834–7869, septembre 2013.

[16] D. JAQUE et F. VETRONE : Luminescence nanothermometry. *Nanoscale*, 4(15):4301–4326, juillet 2012.

[17] C. D. S. BRITES, P. P. LIMA, N. J. O. SILVA, A. MILLÁN, V. S. AMARAL, F. PALACIO et L. D. CARLOS : Thermometry at the nanoscale. *Nanoscale*, 4(16):4799–4829, juillet 2012.

[18] L. M. MAESTRO, P. HARO-GONZÁLEZ, M. C. IGLESIAS-DE LA CRUZ, F. SANZRODRÍGUEZ, Á. JUARRANZ, J. G. SOLÉ et D. JAQUE : Fluorescent nanothermometers provide controlled plasmonic-mediated intracellular hyperthermia. *Nanomedicine*, 8(3):379–388, décembre 2012.

[19] F. VETRONE, R. NACCACHE, A. ZAMARRÓN, A. JUARRANZ DE LA FUENTE, F. SANZ-RODRÍGUEZ, L. MARTINEZ MAESTRO, E. MARTÍN RODRIGUEZ, D. JAQUE, J. GARCÍA SOLÉ et J. A. CAPOBIANCO : Temperature Sensing Using Fluorescent Nanothermometers. *ACS Nano*, 4(6):3254–3258, juin 2010.

[20] M. SCHELLER : Data Extraction from Terahertz Time Domain Spectroscopy Measurements. *Journal of Infrared, Millimeter, and Terahertz Waves*, 35(8):638–648, janvier 2014.

[21] I. PUPEZA, R. WILK et M. KOCH : Highly accurate optical material parameter determination with THz time-domain spectroscopy. *Optics Express*, 15(7):4335–4350, avril 2007.

[22] C. RØ NNE et S. r. R. KEIDING : Low frequency spectroscopy of liquid water using THz-time domain spectroscopy. *Journal of Molecular Liquids*, 101(1):199–218, novembre 2002.

[23] C. RØ NNE, L. THRANE, P.-O. Å STRAND, A. WALLQVIST, K. V. MIKKELSEN et S. R. KEIDING : Investigation of the temperature dependence of dielectric relaxation in liquid water by THz reflection spectroscopy and molecular dynamics simulation. *The Journal of Chemical Physics*, 107(14):5319–5331, octobre 1997.

[24] S. J. OH, J. KANG, I. MAENG, J.-S. SUH, Y.-M. HUH, S. HAAM et J.-H. SON : Nanoparticle-enabled terahertz imaging for cancer diagnosis. *Optics Express*, 17(5):3469–3475, mars 2009.

[25] S. J. OH, J. CHOI, I. MAENG, J. Y. PARK, K. LEE, Y.-M. HUH, J.-S. SUH, S. HAAM et J.-H. SON : Molecular imaging with terahertz waves. *Optics Express*, 19(5):4009–4016, février 2011.

[26] A. STYLIANOU et M. A. TALIAS : Nanotechnology-supported THz medical imaging. *F1000Research*, 2:100, mars 2013.

[27] F. NOVELLI, J. W. M. CHON et J. A. DAVIS : Terahertz thermometry of gold nanospheres in water. *Optics Letters*, 41(24):5801–5804, décembre 2016.

[28] R. NACCACHE, A. MAZHOROVA, M. CLERICI, R. PICCOLI, L. K. KHORASHAD, A. O. GOVOROV, L. RAZZARI, F. VETRONE et R. MORANDOTTI : Terahertz Thermometry : Combining Hyperspectral Imaging and Temperature Mapping at Terahertz Frequencies. *Laser & Photonics Reviews*, 11(5):n/a–n/a, septembre 2017.

[29] B. BAROLI, M. G. ENNAS, F. LOFFREDO, M. ISOLA, R. PINNA et M. ARTURO LÓPEZ-QUINTELA : Penetration of Metallic Nanoparticles in Human Full-Thickness Skin. *Journal of Investigative Dermatology*, 127(7):1701–1712, juillet 2007.

[30] K. W. KIM, H. KIM, J. PARK, J. K. HAN et J. SON : Terahertz Tomographic Imaging of Transdermal Drug Delivery. *IEEE Transactions on Terahertz Science and Technology*, 2(1):99–106, janvier 2012.

[31] I. P. DICK et R. C. SCOTT : Pig Ear Skin as an In-vitro Model for Human Skin Permeability. *Journal of Pharmacy and Pharmacology*, 44(8):640–645, 1992.

[32] B. YU, F. ZENG, Y. YANG, Q. XING, A. CHECHIN, X. XIN, I. ZEYLIKOVICH et R. ALFANO : Torsional Vibrational Modes of Tryptophan Studied by Terahertz Time-Domain Spectroscopy. *Biophysical Journal*, 86(3):1649–1654, mars 2004.

[33] N. Y. TAN, M. T. RUGGIERO, C. ORELLANA-TAVRA, T. TIAN, A. D. BOND, T. M. KORTER, D. FAIREN-JIMENEZ et J. A. ZEITLER : Investigation of the terahertz vibrational modes of ZIF-8 and ZIF-90 with terahertz time-domain spectroscopy. *Chemical Communications (Cambridge, England)*, 51(89):16037–16040, novembre 2015.

[34] M. WALTHER, P. PLOCHOCKA, B. FISCHER, H. HELM et P. UHD JEPSEN : Collective vibrational modes in biological molecules investigated by terahertz time-domain spectroscopy. *Biopolymers*, 67(4-5):310–313, janvier 2002.

[35] J. HOHLFELD, S. S. WELLERSHOFF, J. GÜDDE, U. CONRAD, V. JÄHNKE et E. MATTHIAS : Electron and lattice dynamics following optical excitation of metals. *Chemical Physics*, 251(1–3):237–258, janvier 2000.

[36] I. IVANOV, Y. HU, U. BESER, A. NARITA, K. MÜLLEN, M. BONN et D. TURCHINOVICH : Terahertz Carrier Dynamics in Graphene Nanoribbons with Different Peripherial Functional Groups. *In Conference on Lasers and Electro-Optics (2016), Paper SM3L.6*, page SM3L.6, San Jose, CA, USA, juin 2016. Optical Society of America.

[37] T. CHARI : *Optimization Studies in Graphene Electronics*. Ph.D., Columbia University, 2016.

[38] P. R. SMITH, D. H. AUSTON et M. C. NUSS : Subpicosecond photoconducting dipole antennas. *IEEE Journal of Quantum Electronics*, 24(2):255–260, février 1988.

[39] A. NAHATA, A. S. WELING et T. F. HEINZ : A wideband coherent terahertz spectroscopy system using optical rectification and electro-optic sampling. *Applied Physics Letters*, 69(16):2321–2323, octobre 1996.

[40] R. KÖHLER, A. TREDICUCCI, F. BELTRAM, H. E. BEERE, E. H. LINFIELD, A. G. DAVIES, D. A. RITCHIE, R. C. IOTTI et F. ROSSI : Terahertz semiconductor-heterostructure laser. *Nature*, 417(6885):156–159, mai 2002.

[41] C. A. SCHMUTTENMAER : Exploring Dynamics in the Far-Infrared with Terahertz Spectroscopy. *Chemical Reviews*, 104(4):1759–1780, avril 2004.

[42] P. GRIFFITHS et J. A. DE HASETH : *Fourier Transform Infrared Spectrometry*. Chemical Analysis : A Series of Monographs on Analytical Chemistry and Its Applications. Wiley-Interscience, second édition, 2007.

[43] M. NAFTALY et R. E. MILES : Terahertz Time-Domain Spectroscopy for Material Characterization. *Proceedings of the IEEE*, 95(8):1658–1665, août 2007.

[44] M. R. KUTTERUF, C. M. BROWN, L. K. IWAKI, M. B. CAMPBELL, T. M. KORTER et E. J. HEILWEIL : Terahertz spectroscopy of short-chain polypeptides. *Chemical Physics Letters*, 375(3):337–343, juillet 2003.

[45] A. G. MARKELZ, A. ROITBERG et E. J. HEILWEIL : Pulsed terahertz spectroscopy of DNA, bovine serum albumin and collagen between 0.1 and 2.0 THz. *Chemical Physics Letters*, 320(1):42–48, mars 2000.

[46] M. R. LEAHY-HOPPA, M. J. FITCH, X. ZHENG, L. M. HAYDEN et R. OSIANDER : Wideband terahertz spectroscopy of explosives. *Chemical Physics Letters*, 434(4):227–230, février 2007.

[47] Y.-S. JIN, G.-J. KIM et S.-G. JEON : Terahertz Dielectric Properties of Polymers. *Journal of the Korean Physical Society*, 49(2):513, août 2006.

[48] M. NAFTALY, J. F. MOLLOY, G. V. LANSKII, K. A. KOKH et Y. M. ANDREEV : Terahertz time-domain spectroscopy for textile identification. *Applied Optics*, 52(19):4433–4437, juillet 2013.

[49] D. BANERJEE, W. von SPIEGEL, M. D. THOMSON, S. SCHABEL et H. G. ROSKOS : Diagnosing water content in paper by terahertz radiation. *Optics Express*, 16(12):9060–9066, juin 2008.

[50] Y. LIU, J. TAN, L. JIANG, S. SHI, B. JIN et J. MA : Diagnostic technique of pine wood nematode disease based on THz spectrum. *In SPIE (7277), Photonics and Optoelectronics Meetings (POEM) 2008 : Terahertz*

Science and Technology, volume 7277, page 72770V, Wuhan, China, février 2009. International Society for Optics and Photonics.

[51] K. AHI et M. ANWAR : Advanced terahertz techniques for quality control and counterfeit detection. *In SPIE (9856) :Terahertz Physics, Devices, and Systems X : Advanced Applications in Industry and Defense*, volume 9856, pages 98560G+, Baltimore, MD, USA, 2016.

[52] J. DONG, A. LOCQUET, M. MELIS et D. S. CITRIN : Global mapping of stratigraphy of an old-master painting using sparsity-based terahertz reflectometry. *Scientific Reports*, 7(1):15098, novembre 2017.

[53] E. PICKWELL-MACPHERSON : Practical considerations for in vivo THz imaging. *Terahertz Science and Technology*, 3(4):163–171, décembre 2010.

[54] R. I. STANTCHEV, B. SUN, S. M. HORNETT, P. A. HOBSON, G. M. GIBSON, M. J. PADGETT et E. HENDRY : Noninvasive, near-field terahertz imaging of hidden objects using a single-pixel detector. *Science Advances*, 2(6):e1600190, juin 2016.

[55] D. SUZUKI, S. ODA et Y. KAWANO : A flexible and wearable terahertz scanner. *Nature Photonics*, 10(12):809–813, novembre 2016.

[56] T. OUCHI, K. KAJIKI, T. KOIZUMI, T. ITSUJI, Y. KOYAMA, R. SEKIGUCHI, O. KUBOTA et K. KAWASE : Terahertz Imaging System for Medical Applications and Related High Efficiency Terahertz Devices. *Journal of Infrared, Millimeter, and Terahertz Waves*, 35(1):118–130, janvier 2014.

[57] H.-B. LIU, Y. CHEN, G. J. BASTIAANS et X.-C. ZHANG : Detection and identification of explosive RDX by THz diffuse reflection spectroscopy. *Optics Express*, 14(1):415–423, janvier 2006.

[58] J. DAI, X. GUO et X.-C. ZHANG : Terahertz air photonics for standoff explosive detection. *In IEEE Conference on Technologies for Homeland Security, 2009. HST '09*, pages 461–464, mai 2009.

[59] W. SHI, Y. J. DING, N. FERNELIUS et K. VODOPYANOV : Efficient, tunable, and coherent 0.18–5.27-THz source based on GaSe crystal. *Optics Letters*, 27(16):1454–1456, août 2002.

[60] K. KAWASE, J.-i. SHIKATA, K. IMAI et H. ITO : Transform-limited, narrow-linewidth, terahertz-wave parametric generator. *Applied Physics Letters*, 78(19):2819–2821, mai 2001.

[61] K. J. SIEBERT, H. QUAST, R. LEONHARDT, T. LÖFFLER, M. THOMSON, T. BAUER, H. G. ROSKOS et S. CZASCH : Continuous-wave all-optoelectronic terahertz imaging. *Applied Physics Letters*, 80(16):3003–3005, avril 2002.

[62] I. S. GREGORY, W. R. TRIBE, C. BAKER, B. E. COLE, M. J. EVANS, L. SPENCER, M. PEPPER et M. MISSOUS : Continuous-wave terahertz system with a 60 dB dynamic range. *Applied Physics Letters*, 86(20):204104, mai 2005.

[63] Y. WANG, Z. ZHAO, Z. CHEN, L. ZHANG, K. KANG et J. DENG : Continuous-wave terahertz phase imaging using a far-infrared laser interferometer. *Applied Optics*, 50(35):6452–6460, décembre 2011.

[64] Q. WU, M. LITZ et X.-C. ZHANG : Broadband detection capability of ZnTe electro-optic field detectors. *Applied Physics Letters*, 68(21):2924–2926, mai 1996.

[65] G. W. CHANTRY : Long-wave optics : The science and technology of infrared and near-millimetre waves. Applications. *Astrophysics*, 2:379, 1984.

[66] M. INGUSCIO, G. MORUZZI, K. M. EVENSON et D. A. JENNINGS : A review of frequency measurements of optically pumped lasers from 0.1 to 8 THz. *Journal of Applied Physics*, 60(12):R161–R192, décembre 1986.

[67] Y.-S. LEE : *Principles of Terahertz Science and Technology*. Springer US, Boston, MA, 2009.

[68] A. BERGNER, U. HEUGEN, E. BRÜNDERMANN, G. SCHWAAB, M. HAVENITH, D. R. CHAMBERLIN et E. E. HALLER : New p-Ge THz laser spectrometer for the study of solutions : THz absorption spectroscopy of water. *Review of Scientific Instruments*, 76(6):063110, mai 2005.

[69] C. DAHL, L. GENZEL, P. GOY, G. GRÜNER, J. P. KOTTHAUS, G. KOZLOV, M. C. NUSS, J. ORENSTEIN et A. VOLKOV : *Millimeter and Submillimeter Wave Spectroscopy of Solids*. Springer, softcover reprint of the original 1st ed. 1998 édition, août 2013.

[70] J. FAIST, F. CAPASSO, D. L. SIVCO, C. SIRTORI, A. L. HUTCHINSON et A. Y. CHO : Quantum Cascade Laser. *Science*, 264(5158):553–556, avril 1994.

[71] Y. YAO, A. J. HOFFMAN et C. F. GMACHL : Mid-infrared quantum cascade lasers. *Nature Photonics*, 6(7):432–439, juillet 2012.

[72] S. FATHOLOLOUMI, E. DUPONT, C. W. I. CHAN, Z. R. WASILEWSKI, S. R. LAFRAMBOISE, D. BAN, A. MÁTYÁS, C. JIRAUSCHEK, Q. HU et H. C. LIU : Terahertz quantum cascade lasers operating up to ~ 200 K with optimized oscillator strength and improved injection tunneling. *Optics Express*, 20(4):3866–3876, février 2012.

[73] F. CASTELLANO, S. ZANOTTO, L. H. LI, A. PITANTI, A. TREDICUCCI, E. H. LINFIELD, A. G. DAVIES et M. S. VITIELLO : Distributed feedback terahertz frequency quantum cascade lasers with dual periodicity gratings. *Applied Physics Letters*, 106(1):011103, janvier 2015.

[74] R. DEGL'INNOCENTI, Y. D. SHAH, L. MASINI, A. RONZANI, A. PITANTI, Y. REN, D. S. JESSOP, A. TREDICUCCI, H. E. BEERE et D. A. RITCHIE : Hyperuniform disordered terahertz quantum cascade laser. *Scientific Reports*, 6:19325, janvier 2016.

[75] S. G. RAZAVIPOUR, E. DUPONT, S. FATHOLOLOUMI, C. W. I. CHAN, M. LINDSKOG, Z. R. WASILEWSKI, G. AERS, S. R. LAFRAMBOISE, A. WACKER, Q. HU, D. BAN et H. C. LIU : An indirectly pumped terahertz quantum cascade laser with low injection coupling strength operating above 150 K. *Journal of Applied Physics*, 113(20):203107, mai 2013.

[76] E. H. PUTLEY : Indium Antimonide Submillimeter Photoconductive Detectors. *Applied Optics*, 4(6):649–657, juin 1965.

[77] P. YAGOUBOV, M. KROUG, H. MERKEL, E. KOLLBERG, G. GOL'TSMAN, S. SVECHNIKOV et E. GERSHENZON : Noise temperature and local oscillator power requirement of NbN phonon-cooled hot electron bolometric mixers at terahertz frequencies. *Applied Physics Letters*, 73(19):2814–2816, novembre 1998.

[78] A. SKALARE, W. R. MCGRATH, B. BUMBLE, H. G. LEDUC, P. J. BURKE, A. A. VERHEIJEN, R. J. SCHOELKOPF et D. E. PROBER : Large bandwidth and low noise in a diffusion-cooled hot-electron bolometer mixer. *Applied Physics Letters*, 68(11):1558–1560, mars 1996.

[79] J. F. WEBB : A possible room temperature terrahertz wave source via harmonic generation in a microwave pumped ferroelectric crystal. *In 2009 Asia Pacific Microwave Conference*, pages 186–189, Singapore, décembre 2009.

[80] A. MAESTRINI, J. S. WARD, J. J. GILL, H. S. JAVADI, E. SCHLECHT, C. TRIPON-CANSELIET, G. CHATTOPADHYAY et I. MEHDI : A 540-640-GHz high-efficiency four-anode frequency tripler. *IEEE Transactions on Microwave Theory and Techniques*, 53(9):2835–2843, septembre 2005.

[81] W. LI et J. YAO : Microwave and Terahertz Generation Based on Photonically Assisted Microwave Frequency Twelvetupling With Large Tunability. *IEEE Photonics Journal*, 2(6):954–959, décembre 2010.

[82] X.-C. ZHANG et J. XU : *Introduction to THz Wave Photonics*. Springer US, 2010.

[83] R. ULBRICHT, E. HENDRY, J. SHAN, T. F. HEINZ et M. BONN : Carrier dynamics in semiconductors studied with time-resolved terahertz spectroscopy. *Reviews of Modern Physics*, 83(2):543–586, juin 2011.

[84] R. W. BOYD : *Nonlinear Optics, Third Edition*. Academic Press, Amsterdam ; Boston, 3 edition édition, avril 2008.

[85] F. GANIKHANOV, G.-R. LIN, W.-C. CHEN, C.-S. CHANG et C.-L. PAN : Subpicosecond carrier lifetimes in arsenic-ion-implanted GaAs. *Applied Physics Letters*, 67(23):3465–3467, décembre 1995.

[86] R. J. B. DIETZ, B. GLOBISCH, H. ROEHLE, D. STANZE, T. GÖBEL et M. SCHELL : Influence and adjustment of carrier lifetimes in InGaAs/InAlAs photoconductive pulsed terahertz detectors : 6 THz bandwidth and 90dB dynamic range. *Optics Express*, 22(16):19411–19422, août 2014.

[87] TETECHS INC : Measurement Kit for Research and Development.

[88] D. B. BENNETT, W. LI, Z. D. TAYLOR, W. S. GRUNDFEST et E. R. BROWN : Stratified Media Model for Terahertz Reflectometry of the Skin. *IEEE Sensors Journal*, 11(5):1253–1262, mai 2011.

Liste des publications

Le système décrit dans cette thèse a été utilisé, directement ou indirectement, pour des expériences reliée à l'imagerie sur échantillons de peau. Par conséquence le candidat a été engagé en activités de développement de dispositifs plasmoniques et de procédures d'imagerie avancée. Ce qui suit, est une liste des publications dans des revues scientifiques et de communications lors de conférences produites au cours du travail de thèse.

Journals

[1] V. AGLIERI, X. JIN, A. ROVERE, R. PICCOLI, D. CARAFFINI, S. TUCCIO, F. DE ANGELIS, R. MORANDOTTI, R. MACALUSO, A. TOMA et L. RAZZARI : Improving nanoscale terahertz field localization by means of sharply tapered resonant nanoantennas. *Nanophotonics*, 9(3):683–690, janvier 2020.

[2] L. ZANOTTO, R. PICCOLI, J. DONG, D. CARAFFINI, R. MORANDOTTI et L. RAZZARI : Time-domain terahertz compressive imaging. *Optics Express*, 28(3):3795–3802, février 2020.

[3] J. DONG, H. BREITENBORN, R. PICCOLI, L. V. BESTEIRO, P. YOU, D. CARAFFINI, Z. M. WANG, A. O. GOVOROV, R. NACCACHE, F. VETRONE, L. RAZZARI et R. MORANDOTTI : Terahertz three-dimensional monitoring of nanoparticle-assisted laser tissue soldering. *Biomedical Optics Express*, 11(4):2254–2267, avril 2020.

Conférences

[1] A. TOMASINO, M. K. MRIDHA, A. MAZHOROVA, D. CARAFFINI, H. BREITENBORN, M. CLERICI, M. PECCIANTI, L. RAZZARI, A. C. CINO, S. STIVALA, A. BUSACCA et R. MORANDOTTI : Waveguide-Integrated THz Spectral Filter. *In Photonics North 2015*, Ottawa, Canada, 2015.

[2] A. TOMASINO, M. K. MRIDHA, A. MAZHOROVA, D. CARAFFINI, H. BREITENBORN, M. CLERICI, M. PECCIANTI, L. RAZZARI, A. C. CINO, S. STIVALA, A. BUSACCA et R. MORANDOTTI : Two-Wire Waveguide-Based THz Spectral Filter. *In Colloque de Plasma-Québec*, Montréal, Canada, 2015.

[3] A. TOMASINO, M. K. MRIDHA, A. MAZHOROVA, D. CARAFFINI, H. BREITENBORN, M. CLERICI, M. PECCIANTI, L. RAZZARI, A. C. CINO, S. STIVALA, A. BUSACCA et R. MORANDOTTI : Two-Wire Waveguide-Based THz Spectral Filter. *In Fotonica 2015*, Turin, Italy, 2015.

[4] D. CARAFFINI, R. PICCOLI, X. JIN, S. TUCCIO, R. MORANDOTTI et L. RAZZARI : On the optimization of tapered nanoantennas resonating in the terahertz range. *In 2016 Photonics North (PN)*, pages 1–1, Québec, Canada, mai 2016.

[5] D. CARAFFINI, R. PICCOLI, X. JIN, S. TUCCIO, R. MORANDOTTI et L. RAZZARI : Optimal Taper Angle for Gold Nanoantennas Resonating with Terahertz Radiation. *In Colloque de Plasma-Québec*, Montréal, Canada, mai 2017.

[6] A. TOMASINO, R. PICCOLI, D. CARAFFINI, A. MARKOV, A. MAZHOROVA, R. NACCACHE, F. VETRONE, Y. JESTIN, A. BUSACCA, L. RAZZARI et R. MORANDOTTI : Ultra-broadband terahertz time domain spectroscopy by Solid State Biased Coherent Detection. *In 2017 42nd International Conference on Infrared, Millimeter, and Terahertz Waves (IRMMW-THz)*, pages 1–2, Cancún, Mexico, août 2017.

[7] H. BREITENBORN, J. DONG, A. BRUHACS, D. CARAFFINI, R. PICCOLI, R. MARIN, A. SKRIPKA, F. VETRONE, R. NACCACHE et R. MORANDOTTI : Characterization of the Photothermal Heating Properties of Nanoparticles by Terahertz Radiation. *In Photonics North 2018 : Biophotonics*, Montréal, Canada, juin 2018.

[8] D. CARAFFINI, A. TOMASINO, Y. JESTIN, A. BUSACCA, R. MORANDOTTI et L. RAZZARI : Nonlinear Frequency Mixing Between Terahertz and Optical Waves in Silica. *In Photonics North 2018 : High Power Laser Technology, Ultrafast Optics and Applications*, Montréal, Canada, juin 2018.

[9] X. JIN, J. DONG, A. ROVERE, R. PICCOLI, D. CARAFFINI, A. CEREA, F. DE ANGELIS, R. MORANDOTTI, R. MACALUSO, A. TOMA et L. RAZZARI : Near-field Enhancement Optimization by Tapering Terahertz Gold Nanoantennas. *In Photonics North 2018 : Photonic Theory Design and Simulations*, Montréal, Canada, juin 2018.

[10] H. BREITENBORN, J. DONG, R. PICCOLI, D. CARAFFINI, L. RAZZARI, FIORENZO VETRONE, RAFIK NACCACHE et ROBERTO MORANDOTTI : Terahertz Subsurface Imaging of Nanoparticle-mediated Plasmonic Heating in Skin. *In Photonics North 2019 : Biophotonics*, Québec, Canada, mai 2019.

[11] J. DONG, H. BREITENBORN, D. CARAFFINI, R. PICCOLI, A. O. GOVOROV, L. RAZZARI, R. NACCACHE, F. VETRONE et R. MORANDOTTI : Investigation of Nanoparticle-Assisted Laser Tissue Soldering by Terahertz Radiation. *In 2019 Conference on Lasers and Electro-Optics Europe European Quantum Electronics Conference (CLEO/Europe-EQEC)*, pages 1–1, Munich, Germany, juin 2019. IEEE.

[12] L. ZANOTTO, R. PICCOLI, J. DONG, D. CARAFFINI, R. MORANDOTTI et L. RAZZARI : Terahertz compressive imaging directly in the time domain. *In 2020 CLEO : Laser Science to Photonic Applications (Accepted)*, San Jose, USA (to be held online due to COVID-19), mai 2020.

[13] V. AGLIERI, X. XIN, A. ROVERE, R. PICCOLI, D. CARAFFINI, S. TUCCIO, F. DE ANGELIS, R. MORANDOTTI, R. MACALUSO, A. TOMA et L. RAZZARI : Improved Near Field Enhancement by Tapering Terahertz Gold Nanoantennas Contribution. *In IEEE International Conference in Nanotechnology*, Montréal, Canada, 2020.

[14] L. ZANOTTO, R. PICCOLI, J. DONG, D. CARAFFINI, R. MORANDOTTI et L. RAZZARI : THz Single-pixel Imaging in Time-domain. *In Photonics North (Submitted)*, Niagara Falls, Canada, 2020.

[15] J. DONG, H. BREITENBORN, R. PICCOLI, L. V. BESTEIRO, P. YOU, D. CARAFFINI, Z. WANG, A. O. GOVOROV, R. NACCACHE, F. VETRONE, L. RAZZARI et R. MORANDOTTI : Dynamic Terahertz Investigation of Nanoparticle-assisted Laser-tissue Interaction. *In International Conference on Infrared, Millimeter, and Terahertz Waves (IRMMW-THz) (Submitted)*, Buffalo, USA, 2020.

List of figures

1.1 Break-down of the most common causes of death in 2016. Cancer was in second place in the World by a good margin, but considering only rich countries the margin is reduced. In the case of Canada, cardiovascular diseases conceded the first place to cancer, even if just by a small margin. 9

2.1 The terahertz radiation range falls right between the infrared and microwave portions of the electromagnetic spectrum. 12

2.2 Optical heterodyne generation employs a high-frequency photomixer to combine the frequencies of two input optical waves ω_1 and ω_2 from the Infrared (IR) region (*e.g.*: 200 THz) in order to generate photons at the much lower difference frequency $\omega_2 - \omega_1$: an appropriate choice of $\omega_{1,2}$ yields a wave in the THz band. 14

2.3 Portion of the conduction band energy diagram of a Quantum Cascade Laser (QCL) device. Electrons leak by tunnel effect into the high energy level E_1 in the quantum well and the slow transition between energy levels E_1 and E_2 causes laser emission (depicted by wavy line). The remainder of the energy goes into a phonon by quickly transitioning to energy level E_3, where it is available to tunnel into the matching level E_1 of the next injector. The energy levels are aligned in this way due to an external polarization field. 17

2.4 Schematic representation of frequency matching (a) and phase matching in the collinear (b) and non-collinear (c) configuration (see eq. (2.6)). Here $\omega_{THz}(k_{THz})$ is the angular frequency (wave vector) of the generated Terahertz, while ω_1 (k_1) and ω_2 (k_2) are the angular frequencies (wave vectors) of the impinging laser and of the laser after the Terahertz is generated. The non-collinear configuration is used, for instance, in tilted-pulse-front generation schemes. 21

2.5 Schematic of Electro-Optic Sampling (EOS): the signal and probe are combined along a common path and traverse at the same time an optical crystal. The THz field alters the refractive index of the crystal and causes a change in the polarization state of the probe, which is measured via balanced photodiodes after separation of the two component polarizations by a Wollaston prism. 22

2.6 (a) Band diagram of a Photoconductive Antenna (PCA): the fast intraband transitions cause emission of the signal until the non-radiative relaxation stops the process. (b) Schematic diagram of a PCA used in 'emitter' configuration: an external bias separates the carriers created by the pump laser, thus giving time for the intraband transitions to develop a THz pulse. (c) Schematic diagram of a PCA used in 'detector' configuration: the THz electric field separates the carriers generated by the pump laser, in turn producing a ΔV at the PCA terminals that can be detected using a lock-in amplifier. 28

3.1 (a) Top view of the TeTechS system. [...] (b) Top view of the TeTechS control box. [...] (c) front panel of the TeTechS control box. [...] 33

3.2 Some of the helper functions developed to rationalize the code: `data_manipulation`, `save_load_data` and `zaber_wrapper`, from left to right respectively. The entries labeled 'constants', 'controls' and 'core' in the `save_load_data` panel represent sub-palettes for functions that are used almost only internally within the library. 36

3.3 User Interface (UI) of the main program. Each panel contains controls for one main functionality (slow scan, fast scan, imaging, plotting), with one panel reserved for grouping the controls for the ancillary features. To keep the UI as clean as possible, seldom used controls are placed in secondary tabs. 39

3.4 Detail of the diagram of the **`Graphing_center`** sub-VI (the initialization part is not shown). [...] The inset at the upper right corner shows the input terminals of the sub-VI. 41

3.5 Detail of the diagram of the **`OutputManager`** sub-VI (the initialization part is not shown). The inset at the upper left corner shows the input terminals of the sub-VI. 43

3.6 Detail of the diagram of the **`slow_scanner`** sub-VI (the initialization part is not shown). [...] The inset close to the upper left corner shows the input terminals of the sub-VI. 45

3.7 Illustration of the sliding window effect on example triangular pulses. To simulate the scan we took the average of the example pulses over a window starting at the measurement time and extending to the left (right) for forward (backward) sweeps, using window widths of $2\,\mathrm{a.u.}$ and $4\,\mathrm{a.u.}$ ($-2\,\mathrm{a.u.}$ and $-4\,\mathrm{a.u.}$). [...] 48

3.8 Diagram of the **`Trigger_Emulator`** sub-VI. The signal is read sample by sample and compared to the **`Threshold`**. When the condition is met, the sub-VI terminates, giving control back to the caller. The data acquisition task is stopped if the **`Stop_task (optional)`** contains the value True (default True, but we pass the value False). The inset in the lower part shows the input terminals of the sub-VI. 48

3.9 Display of the `LongAction` from the main loop of the **`ShakeAndRead`** sub-VI. [...] The inset in the lower left part shows the input terminals of the sub-VI. 52

3.10 Detail of the diagram of the **`fast_scan_procedure`** sub-VI (the initialization part is not shown). [...] The inset close to the lower right corner shows the input terminals of the sub-VI. 54

3.11 Detail of the diagram of the **`Image_scanner`** sub-VI (the initialization part is not shown). [...] The inset close to the lower right corner shows the input terminals of the sub-VI. 57

4.1 Reference measurement of the THz pulse circulating in our system. The arbitrary units of the upper y-axis are actually volts, since we are measuring the analog output of the lock-in: the factor used to convert the reading to the THz electric field is dependent on the sensitivity value. The lower panel shows the power spectrum of the signal: while it contains absorption lines from the non-purged atmosphere, it is otherwise well behaved up to 2 THz. 59

4.2 Plots of the signal offset ***a***, the pulse peak maximum value ***b***, position ***c*** and Full Width at Half Maximum (FWHM) ***d***, the Dark Noise (DN) ***e*** and the Dynamic Range (DR) ***f*** for traces taken with t_{int} ranging from 10 µs to 10 000 µs. The green-shaded range is considered optimal for actual operation. 61

4.3 Comparison between scans performed with t_{int} equal to 10 µs and 100 µs. The smaller t_{int} is not able to filter-out the noise, to the point that the fluctuations at the signal peak fall out of scale (> 10 V, see top panel). The larger t_{int} used for the trace in the lower panel is the one selected by default in the software. 62

4.4 Comparison between the reference measurement from fig. 4.1 and fast scans. For the sake of clarity, only the scans performed at 1 Hz, 5 Hz, 6 Hz and 10 Hz are reported and the traces have been time-shifted to match the respective peak positions. [...] 63

4.5 Stability of fast scan results for $\nu_{\text{PRF}} = 5\,\text{Hz}$. Top: standard deviation of the traces (σE_{THz}) vs. time (delay). Middle: main peak eight (E^{peak}_{THz}) vs. scan number. Bottom: main peak time (t^{peak}) vs. scan number. On the right, histograms of the Y values relative to the plots on the left are shown (the top one has logarithmic scale). 64

4.6 Stability of fast scan results for $\nu_{\text{PRF}} = 6\,\text{Hz}$. Top: standard deviation of the traces (σE_{THz}) vs. time (delay). Middle: main peak eight (E^{peak}_{THz}) vs. scan number. Bottom: main peak time (t^{peak}) vs. scan number. On the right, histograms of the Y values relative to the plots on the left are shown (the top one has logarithmic scale). 65

4.7 Stability of fast scan results for $\nu_{\text{PRF}} = 10\,\text{Hz}$. Top: standard deviation of the traces (σE_{THz}) vs. time (delay). Middle: main peak eight (E^{peak}_{THz}) vs. scan number. Bottom: main peak time (t^{peak}) vs. scan number. On the right, histograms of the Y values relative to the plots on the left are shown (the top one has logarithmic scale). 66

4.8 Mounted pig skin sample before irradiation. The $\otimes$ signs mark the 27 irradiation sites, the visiting order is indicated by the arrows and numbers. 67

4.9 Peak value of the THz traces taken during irradiation along the path shown in fig. 4.8. The three plots correspond to irradiation on the top, center and bottom lines. Note that the center line was measured first, followed in order by the top and bottom ones, hence the trace numbers in the abscissae axes are not consecutive for the three plots. [...] 69

4.10 ***a*** photograph of the skin sample after irradiation following the pattern illustrated in fig. 4.8. ***b*** definitions of the shape parameters extracted from the traces measured by the **`Image_scanner`** sub-VI. [...] 70

4.11 Imaging of the skin sample using various properties of the reflected THz pulses. [...] 71

List of abbreviations

3D three dimensional

ABCD Air Biased Coherent Detection

BS beamsplitter

BWO Backward Wave Oscillator

CSV Comma Separated Values

CT chemotherapy

CW Continuous Wave

DAQ Data Acquisition

DFG Difference Frequency Generation

DN Dark Noise

DNA deoxyribonucleic acid

DR Dynamic Range

EFISH Electric Field Induced Second Harmonic

EM Electro Magnetic

EOS Electro-Optic Sampling

FDL fast delay line

FEL Free Electron Laser

FTIR Fourier Transform Infrared

FWHM Full Width at Half Maximum

FWM Four Wave Mixing

GaAs Gallium Arsenide

GNR Gold Nanorods

IR Infrared

LO local oscillator

LT-GaAs Low-temperature grown Gallium Arsenide

MKRD Measurement Kit for Research and Development

NI National Instruments

NIR near infrared

NP nanoparticles

OR Optical Rectification

OS Operating System

PC Photoconductive

PCA Photoconductive Antenna

PDT Photodynamic Therapy

PMT Photomultiplier Tubes

PRF pulse repetition frequency

PTT Photothermal Therapy

QCL Quantum Cascade Laser

RDX Research Department Explosive

RF Radio Frequency

RMS Root Mean Square

RT radiotherapy

SDL slow delay line

SH Second Harmonic

SNR Signal to Noise Ratio

SRF Scan Repetition Frequency

SSBCD Solid-State Biased Coherent Detection

SUT Sample Under Test

T-GAP THz Gap

TDS Time Domain Spectroscopy

THz/Terahertz Terahertz radiation

THz-TDS Terahertz Time-Domain Spectroscopy

TNT Trinitrotoluene

UI User Interface

UV Ultraviolet

VI Virtual Instument

ZnTe Zinc Telluride

Chapter 1. Motivation

Physics research is not merely a means to satisfy innate human curiosity. Although it may not be apparent to a wide public, there was always synergy between the investigation of natural phenomena and engineering, whose ultimate focus is to provide and improve solutions to practical issues affecting virtually all aspects of human life, from rest (memory foam mattresses) to travel (airplanes). Most important among such aspects is healthcare.

As medical science advances, the incidence and relative severity of diseases shifts and new challenges arise to prominence: a chief example of this process being cancer.

Cancer is the product of an imbalance in the biological process of apoptosis, which upholds body health by the 'programmed' death and subdivision of the cells. When genetic material DNA is damaged during mitosis, the affected cells may start growing and multiply faster than normal, while dying-off later than expected, thereby forming a tumor. Since DNA damage is a random effect, increased life spans make it less likely for any individual to never be affected. In fact, in several countries, cancer ranks as the second most common cause of death following cardiovascular diseases and, with significant improvement in treatment and prevention of the latter, the former is foreseen to rise to prominence in many parts of the World. Already in 2016, Canada saw cancer take prominence over cardiovascular diseases by a small margin (see fig. 1.1) [1], becoming almost twice as frequent in Canada than in the World in general.

These figures are subject to variation from year to year, but they firmly establish cancer as a major deathly disease, causing great suffering to the millions of people that are diagnosed with it around the World, and to their families. Many strategies are under study for the treatment of cancer, but some of the older ones are still considered among the most successful, namely surgery, chemotherapy (CT) and radiotherapy (RT). [2, 3]. These treatments are however quite damaging for the patient, as they entail the ablation or cellular damaging of tissue surrounding the tumor (surgery and RT), or the administration of substances that cause local and systemic intoxication (CT). Therefore, a significant part of the current research effort in cancer therapy is devoted to the reduction of these adverse effects by developing drugs that can attack tumor cells more selectively, either because of their chemistry or through sophisticated delivery systems.

Of special interest to physicists in the domain of optics are the techniques of Photodynamic Therapy (PDT) and Photothermal Therapy (PTT) that use Electro Magnetic (EM) radiation to cause tumor cells disruption. Both rely on

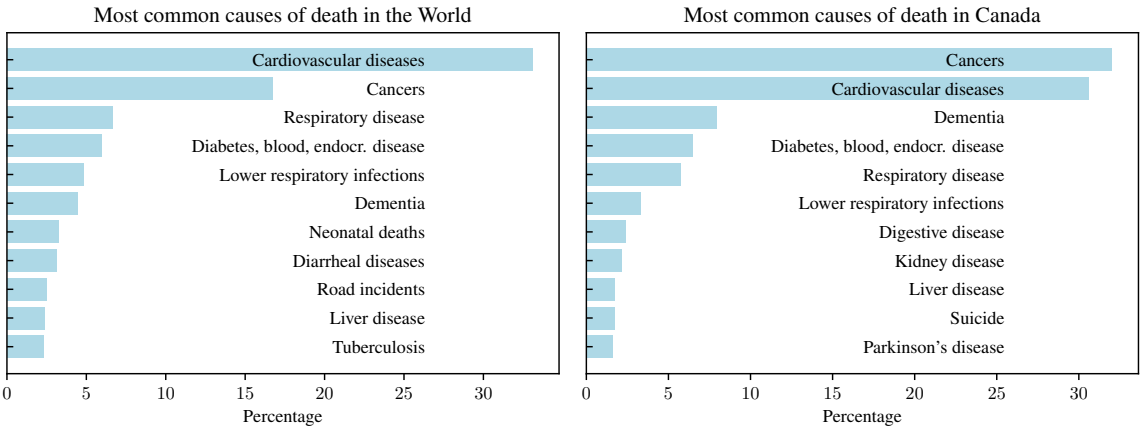

Figure 1.1: Break-down of the most common causes of death in 2016. Cancer was in second place in the World by a good margin, but considering only rich countries the margin is reduced. In the case of Canada, cardiovascular diseases conceded the first place to cancer, even if just by a small margin. [1]

substances that are absorbed preferentially by tumor cells and excited via light stimuli, but differ in that PDT initiates in the active substance a series of photochemical a and photobiologic processes that damage cancer cells, while PTT employs the active substance as a medium to selectively deliver heat in the cancerous tissue. [4,5] The heating is typically obtained by plasmonic excitation of nanoparticles that resonate with Infrared (IR) light and transfer energy to the tissue via a plasmon-phonon relaxation process [6]. The most commonly used plasmonic materials for biomedical applications are noble metals (such as gold and silver) due to their known lower toxicity in bulk form. However, it is possible for their nanoparticle form to behave differently, thus requiring further investigation.

For obvious reasons, this kind of treatment is only applicable for tumors that are not too deep under the epithelium (including that of internal cavities reachable via endoscopy) and are thereby mostly considered as coadjutant to other therapies, either because of scarce availability or limitations to the kind of tissue they can successfully damage [7–9]. It is worth underlining, in relation thereto, that skin cancer is slowly becoming more common among young adults. According to a 2014 review on data collected up to 2006, the most serious histological type of cancer, the melanoma, saw an increase in its incidence of $1.2\,\%$ and $1.5\,\%$ for females and males respectively [10], thus highlighting the urgency of developing PDT and PTT application techniques to their full potential.

The practice of PTT rises the necessity of monitoring the temperature reached by the treated area, since it is the key to the efficacy of the process.

The temperature of the skin can be determined by thermometers [11] based on thermistors or by infrared thermometry and thermography [12–14], but the former require contact with the skin (which increases the risk of contamination), and have poor spatial resolution, hence unable to discern different heating between healthy and cancerous cells. Infrared thermometers on the other hand provide non-contact, non-destructive detection by sensing temperature-dependent infrared radiation in the range of $8\,\mu\mathrm{m}$ to $13\,\mu\mathrm{m}$. Such thermal radiation emanates from warm objects, and allows for the reconstruction of two-dimensional thermal images [12, 15, 16], however, its accuracy quickly deteriorates with the depth beneath the surface of the skin at which the heat is being delivered.

To achieve a non-contact measurement of sub-surface skin temperature, with sub-micrometer resolution, it is possible to employ temperature-sensitive, fluorescent nanoparticles (NP) [17–22]. Those provide intracellular thermal sensing capabilities, although the selection of the materials should be well thought out, since they must be injected in addition to the substances required to perform the therapy.

An alternative to fluorescent NP is the exploitation of the properties of Terahertz radiation, which is non-ionizing and thus causes minimal harm to biological tissues. Terahertz radiation generation and detection will be discussed in detail in Chapter 2. Here it will suffice to mention that the extraction of several optical properties of the tissues themselves (*e.g.*: the complex refractive index [23, 24]) at different depths with a sub-millimeter spatial resolution becomes possible by using polarized THz pulses. The latter typically propagate through, or are reflected by, tissues, being subsequently retrieved and characterized via coherent detection techniques.

Knowledge regarding temperature-dependent refractive index changes of water in the THz regime [25, 26] can be applied to infer the (more medically relevant) temperature and hydration level of the skin and be of assistance during PTT sessions, to verify that the proper amount of heat is delivered within the relevant area.

Moreover, since non-polar, nonmetallic dielectrics such as textiles and plastics are transparent in the THz range [27], the hydration level and temperature can be determined under obstructed conditions [28], such as gauze dressings.

So far, few studies exist on the application of laser-excited NP as contrast agents to image cancerous cells with the help of Terahertz Time-Domain Spectroscopy (THz-TDS) [29–31], or to heat aqueous NP suspensions while characterizing temperature dynamics using Terahertz [32, 33]. The reported studies have predominantly *i*) focused on two-dimensional THz imaging of tumors in excised organs or *ii*) characterized the heat distribution

of NP dispersions injected into skin tissue. However, the above-mentioned studies have not exploited Terahertz to the full extent of its capabilities, for instance in retrieving amplitude and phase information which can be used for precise Time-of-flight analysis.

This thesis work is part of a project whose ultimate aim is to utilize the information that can be gathered via Time Domain Spectroscopy (TDS) to perform three dimensional (3D) mappings of THz thermal imaging to visualize the trans-dermal distribution of NP [34] injected or drop-cast in different skin tissue samples with and without excitation by laser illumination, in analogy to what has been shown in recent studies involving the subcutaneous distribution of a drug within biological tissue [33, 35]. Although the initial characterization will be performed on aqueous solutions and porcine skin, the final setup is intended for use as a complement to clinical treatment of patients, so the focus of this thesis is the development of a fast and reliable data acquisition setup, with an interface aimed at personnel that is not necessarily familiar with the inner details of a THz-TDS system. The requirements and implementation details will be discussed in chapter 3.

Chapter 2. Introduction to Terahertz

All EM radiation is essentially the same physical phenomenon, described by the formalism of wave propagation, but depending on the wavelength/frequency, it exhibits a great variety of generation processes and peculiar ways to interact with matter. For this reason, it is customary to refer with conventional names to specific portions of the spectrum comprising frequencies that show similar behaviour. Most of the names are descriptive ones, such as Ultraviolet (UV), Visible, IR, Microwave and Radio Frequency (RF).

Around the boundary between Microwaves and IR there is an especially interesting region that is often referred to as Terahertz radiation (THz or Terahertz), or Terahertz. Specifically Terahertz is named after its characteristic frequency of $0.1\,\mathrm{THz}$ to $10\,\mathrm{THz}$ (fig. 2.1), which means $30\,\mu\mathrm{m}$ to $3000\,\mu\mathrm{m}$ in terms of wavelength and corresponds to photon energies of ~$0.4\,\mathrm{meV}$ to $41\,\mathrm{meV}$. Due to this localization, both generation and detection of Terahertz pose particular challenges when tackled with the tools and methods available for the two neighbouring ranges. In fact, frequencies exceeding $10^{11}\,\mathrm{Hz}$ are beyond the capabilities of conventional electronics (Microwaves), while normal optical technologies rely on processes involving photon energies much higher than the typical THz energy of ~$1\,\mathrm{meV}$. For a long time, the expression THz Gap (T-GAP) has been used to highlight the comparative lack of applications in this frequency domain, when compared with Microwaves and IR, due to the necessity to develop *ad hoc* solutions for the generation, manipulation and detection of Terahertz. This hindered the adoption of THz-based technological solutions, a condition that has steadily changed over the past couple of decades, as the development of ultrafast optics and semiconductor physics enabled the design or the improvement of several kinds of reliable detectors, sources and measurement techniques (*e.g.*: [36–38]) that opened-up the interesting possibilities this wavelength range has to offer.

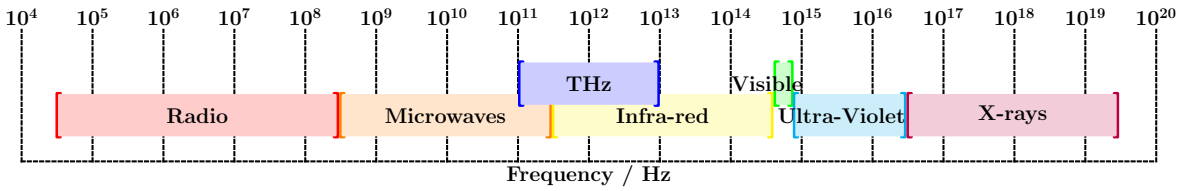

Figure 2.1: The terahertz radiation range falls right between the infrared and microwave portions of the electromagnetic spectrum.

Terahertz radiation frequencies, in fact, match the rotational and vibrational transitions in molecules, collective vibrational or torsional modes [39–41] in condensed matter, as well as low-energy excitations and carrier dynamics in electronic materials [42–44]. Therefore, by performing spectroscopic measurements on a sample, it is possible to identify such key excitations by searching for their unique signature in the absorption spectrum. In this respect, the technique called THz-TDS [45], makes Terahertz especially effective and versatile, because it allows the measurement of the electric field vector ($\mathbf{E}$) rather than recording its intensity ($E = |\mathbf{E}|$) as it is usually the case in optics, *e.g.*: with Fourier Transform Infrared (FTIR) spectroscopy [46]. THz-TDS has been used in the characterization of several polymers such as Polyethylene, Polypropylene, Polycarbonate etc. [47], as well as for the study of small bio-molecules (*e.g.*: amino acids, polypeptides) [48], bio-macromolecules (*e.g.*: DNA, ribonucleic acid, proteins) [49] and for the identification of explosives such as Trinitrotoluene (TNT) and Research Department Explosive (RDX) [50].

Moreover, Terahertz can be manipulated by refraction diffraction and reflection, just like visible light, making it suitable for imaging applications at a typical resolution that is comparable to that of the human eye. Furthermore, several materials (besides air) commonly used in industry, such as plastic, paper, ceramic, textile and wood [51–54] have a fairly good degree of transparency to Terahertz, enabling non-contact measurements to be performed on hidden objects and packaged goods (*e.g.*: quality assurance at a production line [55], cultural heritage diagnostics [56]). Conversely, other established techniques require contact (Ultrasounds) or are hindered by intervening material (IR thermography). In the case of X-rays there is also the health hazard due to ionization, which is avoided using Terahertz, given the small amount of energy ($O(\mathrm{meV})$) carried by its photons. The intrinsic safety of Terahertz makes it suitable for probing living tissues, even though the penetration depth *in vivo* is reduced by the presence of large amounts of water with respect to the case of dielectrics, limiting its use to sub-dermal applications (to achieve detection at a depth of about $5\,\mathrm{mm}$ a Signal to Noise Ratio (SNR) of 10000 is required [57]). All these unique properties make terahertz a highly attractive candidate for sensing and monitoring systems in the biological and biomedical fields, as well as for material inspection, security and defense applications [58–62].

In the next section we expose a non-exhaustive review of the principal techniques available to date for the generation and detection of Terahertz radiation, that will form the basis for the selection of the most suitable approach for our intended task.

2.1 Review of generation and detection methods

Throughout the last few decades, research addressed to a good extent the issues related to the generation and detection of Terahertz, progressively filling the T-GAP with several solutions, by borrowing techniques and devices commonly used in the neighbouring domains of microwaves and photonics, as well as by developing domain specific solutions. The advances in semiconductor technology and ultrafast optics, have been of special importance, leading to the development of techniques based on microwaves manipulation, photomixers [63], Photoconductive (PC) antennas [64], electro-optic crystals [37], Backward Wave Oscillators [65] and thermal detectors [66].

Broadly speaking, both generation and detection techniques fall typically into three regimes:

1. Narrow-band/Continuous Wave (CW).
2. Broadband.
3. Ultra-broadband.

In the first category we have, for the generation of THz (THz), photomixers, nonlinear crystals (2^{nd} order non-linearity) [67, 68], quantum cascade lasers [38] etc., while thermal detectors and heterodyne measurement systems are commonly used for the detection part. Some of these CW sources are also suited for THz wave imaging (see [69–71]). The pulsed emission/detection of Terahertz is covered in the two remaining regimes; these are listed as separate cases because the techniques employed to measure broadband pulsed are hardly able to work for frequencies past $4\,\mathrm{THz}$, where the radiation resonates with the phonons of the transducer crystal (for instance, Zinc Telluride (ZnTe) has $5.3\,\mathrm{THz}$ phonons [72]), and is therefore heavily distorted, so special equipment is required to treat ultra-broadband signals.

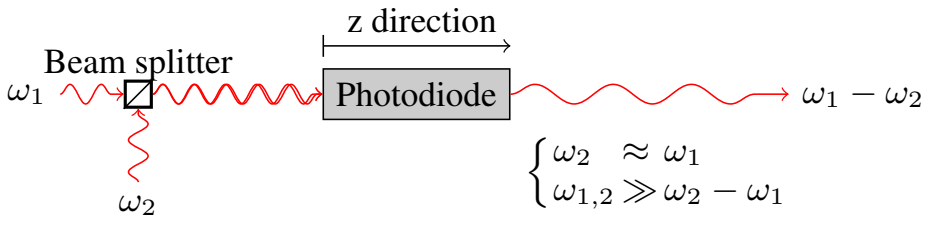

Figure 2.2: Optical heterodyne generation employs a high-frequency photomixer to combine the frequencies of two input optical waves ω_1 and ω_2 from the IR region (*e.g.*: $200\,\mathrm{THz}$) in order to generate photons at the much lower difference frequency $\omega_2 - \omega_1$: an appropriate choice of $\omega_{1,2}$ yields a wave in the THz band. [73]

2.1.1 CW sources

a) Photomixing

Photomixing, also known as optical heterodyne down conversion, mixes two lasers with slightly different frequencies (ω_1 and ω_2) inside a nonlinear medium (*e.g.*: photoconductor or superconductor) to generate EM radiation at the lower frequency corresponding to the difference between those of the inputs ($\omega_{beat} = \omega_1 - \omega_2$). With a suitable choice of $\omega_{1,2}$, the process will then produce Terahertz radiation.

Typically, the input frequencies are made collinear with a Beamsplitter (BS) (see fig. fig. 2.2), so that they can beat together along the common path to a device consisting of a semiconductor substrate with an antenna deposited on it. Such a device acts as PC switch (the geometry can vary, *e.g.*: logarithmic spiral [63, 74], inter-digitated array [75]).

If a voltage is applied on the antenna electrodes, the induced photocurrent oscillates at the beat frequency (ω_{beat}) of the two incident laser beams, thus emitting CW Terahertz at the corresponding frequency. Besides tuning the beat frequency, the choice of substrate material is also important: generally, Low-temperature grown Gallium Arsenide (LT-GaAs) is used due to the high mobility and short life time of the charge carriers it generates in this process. The typical output power of this technique is on the order of microwatts, which is lower than other CW THz sources.

b) Far infrared gas lasers

There is a distinct possibility to produce Terahertz using *traditional* laser technology, by selecting a suitable gain medium. For instance, molecular gases such as CH_3F, CH_3OH, NH_3 and CH_2F_2 have permanent dipole moments, with rotational transitions lying in the THz region.

For example CH_3OH is capable of laser emission at frequencies of $0.245\,\mathrm{THz}$, $0.525\,\mathrm{THz}$, $2.52\,\mathrm{THz}$, $4.25\,\mathrm{THz}$, $4.68\,\mathrm{THz}$, $7.1\,\mathrm{THz}$ and $8.0\,\mathrm{THz}$ with a recorded output power of nearly $10\,\mathrm{mW}$, $40\,\mathrm{mW}$, $100\,\mathrm{mW}$, $100\,\mathrm{mW}$, $20\,\mathrm{mW}$, $10\,\mathrm{mW}$ and $10\,\mathrm{mW}$, respectively [76], but many other molecules are available for other frequencies, up to $7.9\,\mathrm{THz}$ [77]; however there are several alternative methodologies to implement THz lasers as we will see in the following.

c) P-type germanium lasers

The p-type germanium lasers are interesting because they are electrically pumped, solid-state devices, hence relatively compact. In cryogenic conditions ($T < 40\,\mathrm{K}$), applying crossed electric and magnetic fields to a p-doped germanium crystal (typically with beryllium), results in carriers circling in confined cyclotrons trajectories, that exhibit quantization of kinetic energy (Landau levels).

The presence of the electric field accelerates the Heavy Holes of the crystal, promoting them to an excited state whose dominant decay mode is the emission of optical phonons. After such emission, the hole occupies a pseudo-stable Landau level that is progressively filled, causing population inversion and ultimately lasing by stimulated transitions between two of such levels (for further details see [66]).

The resulting Terahertz radiation is produced in pulses of several μs (effectively CW for most applications) with a pulse energy of few μJ and average output power reaching up to a few W. Despite the requirement for cryogenic temperatures, there is the advantage that the frequency is tunable from $1\,\mathrm{THz}$ to $4\,\mathrm{THz}$ by changing the electric and magnetic field strengths [78].

d) Free Electron Laser

Free Electron Laser (FEL) use a beam of accelerated electrons as the medium. The electron beam is generated using a particle accelerator and is propagated through a series of magnets oriented so that the magnetic field is perpendicular to the beam and has periodically alternating polarity. Such an arrangement causes the electrons to oscillate at a set frequency, emitting monochromatic and coherent EM radiation. To fully explain the physics behind such a system, it is necessary to use a relativistic treatment that is beyond the scope of this thesis; more details can be found in reference [66].

Since this approach requires a full-blown particle accelerator (although on the low energy end), THz FEL facilities are very large and extremely costly. Therefore, THz FEL are only available at dedicated multi-user sites, yet they can deliver more power than all other sources.

Examples of facilities are FIREFLY, located at Stanford CA (USA), that generates Terahertz radiation in the range $4\,\mathrm{THz}$ to $20\,\mathrm{THz}$ and CLIO, located at Laboratoire de Chimie Physique in Orsay (France), working in the range from $2\,\mathrm{THz}$ to $100\,\mathrm{THz}$ [66].

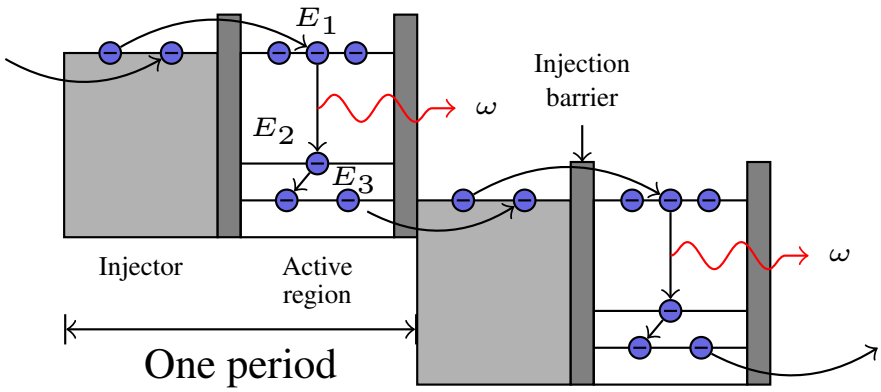

Figure 2.3: Portion of the conduction band energy diagram of a Quantum Cascade Laser (QCL) device. Electrons leak by tunnel effect into the high energy level E_1 in the quantum well and the slow transition between energy levels E_1 and E_2 causes laser emission (depicted by wavy line). The remainder of the energy goes into a phonon by quickly transitioning to energy level E_3, where it is available to tunnel into the matching level E_1 of the next injector. The energy levels are aligned in this way due to an external polarization field.

e) Backward Wave Oscillator

The Backward Wave Oscillator (BWO) (also known as carcinotron) is a vacuum tube system that generates Terahertz from the interaction between an electron beam and a periodic structure placed inside the BWO, process similar to the one of FEL, where the alternating magnetic field is replaced by a mechanical grating (see reference [79] for detailed description). The electron beam gains kinetic energy from a voltage bias applied in the BWO and interacts with the periodic structure producing radiation traveling backwards with respect to the electron beam. The frequency of the Terahertz emitted can be tuned by changing the bias voltage on the BWO: the model described in reference [79] can operate from $0.03\,\mathrm{THz}$ to $1\,\mathrm{THz}$. The output power reaches up to $100\,\mathrm{mW}$ below $200\,\mathrm{G/hertz}$ and falls down to $1\,\mathrm{mW}$ at $1\,\mathrm{THz}$.

f) Quantum Cascade Lasers

The Quantum Cascade Laser (QCL) is a type of device that is being studied intensely because it holds promise for a THz source that is very compact and relatively inexpensive to produce once it reaches the mass market phase. It is based on semiconductor heterostructures built by alternating layers of different semiconductors (superlattice structure). The layers determine a 2D confinement of carriers, resulting in an array of coupled quantum wells,

which induces a potential stairwell of discrete energy levels called subbands (see fig. fig. 2.3). Applying an external bias, the electron migrates from one well to the next according to the tunneling probability and lifetime of each level. Under the right combination of parameters, this may cause a population inversion and consequent laser emission [80].

Given the periodic structure, the same electron undergoes multiple intersubband transitions while traversing the superlattice (cascading) therefore generating several photons, whose features are defined by the quantum confinement properties of the potential wells, rather than the material employed [81–84].

In the literature, one of the first optimized THz QCL based on chirped superlattice was reported in 2002 [38]. Presently, commercial QCLs capable of producing a peak power level $> 20\,\mathrm{mW}$ and average power levels $> 1\,\mathrm{mW}$ at frequencies between $1.8\,\mathrm{THz}$ and $5\,\mathrm{THz}$ are available in the market [85]. In most cases these devices need cryogenic temperature (on the order of $40\,\mathrm{K}$) to operate; however, research is progressively lifting this requirement and devices operating at temperatures as high as $150\,\mathrm{K}$ are reported in the literature [86].

g) Microwave frequency multipliers

Most techniques based on electronics devices or the manipulation of microwaves give rise to narrowband terahertz pulses, obtained via higher harmonic generation [87] or using a driving microwave to produce sidebands in a CW laser that are pulled further apart by Four Wave Mixing (FWM) and then mixed again to produce a signal with twelve times the microwave frequency [88], just inside the THz region.

Another possibility is the use of a Schottky diode-based frequency multiplier which is a microwave analogue of nonlinear optical crystals. A Schottky diode can therefore produce harmonics of the incoming microwave frequencies and emit Terahertz. For example, a frequency tripler based on microwave technology can generate CW THz sources with $22\,\mathrm{mW}$ to $25\,\mathrm{mW}$ output power in the $0.552\,\mathrm{THz}$ to $0.645\,\mathrm{THz}$ range [89].

2.1.2 CW detectors

a) Heterodyne detectors

Often the same processes employed for Terahertz generation can also be adapted for the detection part of systems: heterodyne detection is based on frequency down conversion in a nonlinear device, in analogy to the generation

by photomixing, the incident Terahertz radiation (ω_{THz}) is mixed with a reference radiation (also known as local oscillator) at a fixed frequency ω_{LO}, for a sum field intensity of:

$$I \propto \left(E_{\mathrm{THz}} e^{-\mathrm{i}\omega_{\mathrm{THz}} t} + E_{LO} e^{-\mathrm{i}\omega_{LO} t}\right) \cdot \left(E_{\mathrm{THz}} e^{\mathrm{i}\omega_{\mathrm{THz}} t} + E_{LO} e^{\mathrm{i}\omega_{LO} t}\right) = \\ E_{\mathrm{THz}}^2 + E_{LO}^2 + E_{\mathrm{THz}} E_{LO} \cos\left(\omega_{\mathrm{THz}} - \omega_{LO}\right) t + E_{\mathrm{THz}} E_{LO} \cos\left(\omega_{\mathrm{THz}} + \omega_{LO}\right) t. \quad (2.1)$$

In the last line of eq. (2.1), the first two terms are constants, thus easily filtered out, while the last two oscillate at the difference (I_-) and sum frequency (I_+), respectively. The sum frequency is too high for the electronic equipment and I_+ contributes with its average of zero to the detection, while, if the local oscillator (LO) frequency is close enough to the signal one, I_-, will show up as an oscillating term with amplitude proportional to E_{THz}:

$$I_{det} \propto \left(E_{LO} \cos\left(\omega_{\mathrm{THz}} - \omega_{LO}\right) t\right) E_{\mathrm{THz}}. \quad (2.2)$$

This argument also holds when the mixing of LO and signal is non-linear and higher harmonics are present in the output, together with the inputs themselves. The advantage of this technique is that even feeble THz signals can be detected by increasing the intensity of the local oscillator. While gas lasers are generally used as local oscillators to detect radiations greater than 1 THz, solid-state emitters such as QCLs are considered as promising local oscillator in the region 0.1 THz to 1 THz. Some of the most sensitive mixers for THz detection are cryogenic detectors (hot electron bolometers) based on indium antimonide (InSb) [90] or niobium (Nb) and niobium nitride (NbN) in a superconductor phase [91, 92].

b) Thermal detectors

The simplest detection systems for CW Terahertz employ thermal detectors. These consist of a radiation absorber, that converts incident THz power into heat. The change in temperature is measured via a thermometer. To ensure detection of small variations in the signal, the heat capacity of the absorber must be small, and a heat sink is required to avoid heat pileup and keep the detector responsive. To determine the absorbed radiation energy, the detector must be calibrated as a function of temperature. Detectors of this class come in different kinds, differing in the scheme used to measure the change in temperature *e.g.*: bolometers, pyroelectric detectors and Golay cells.

A bolometer employs a material whose electrical resistance depends on temperature (*e.g.*: Si or Ge) and requires temperatures below that of liquid helium to achieve maximum sensitivity [68, 69]. Therefore, they are generally bulky and expensive. In a pyroelectric detector, the sensing element is a capacitor, filled with a pyroelectric material, so that changes in temperature are converted spontaneously to electric polarization, thus altering the capacity.

Golay cells consist of an absorbing film adjacent to a gas chamber. The thermal expansion of the gas can then be measured via an optical setup (reflectivity of the cell) to determine the rise in temperature. Pyroelectric detector and Golay cells are normally operated at room temperature, though some care must be taken to account for environmental fluctuations.

The advantage of thermal detectors is their sensitivity over a broad spectral range. However, they have response times of the order of $0.1\,\mathrm{s}$ for cryogenic bolometers and typically around $1\,\mathrm{s}$ for models operating at room temperature. More details can be found in reference [66].

2.1.3 Broadband pulsed sources and detectors

a) Terahertz generation by an electro-optic crystal

The polarization of a material ($\mathbf{P}$) due to the electric field ($\mathbf{E}$) can be expressed in the most general case as a Taylor series expansion in $\mathbf{E}$ with coefficients $\chi^{(n)}$ known as the n-th rank electrical susceptibility tensors of the material:

$$P_i(t) = \chi^{(1)}_{ij} E_j(t) + \chi^{(2)}_{i,j,k} E_j(t) E_k(t) + \chi^{(3)}_{i,j,k,l} E_j(t) E_k(t) E_l(t) + \dots \tag{2.3}$$

The term containing the second order susceptibility $\chi^{(2)}$ gives rise to a phenomenon called Optical Rectification (OR) that can be used to produce Terahertz radiation. This technique, also called Difference Frequency Generation (DFG), requires *i*) an electro-optic crystal without inversion symmetry (non-centrosymmetric), so that its $\chi^{(2)}$ is not identically zero, and *ii*) an intense laser source, to make the second order term of eq. (2.3) non negligible. Since the electric field can be expressed as a Fourier integral over the set of all plane waves (using Einstein's sum convention):

$$E_i(t) = \int_{-\infty}^{\infty} E_i(\omega) e^{-\mathrm{i}\omega t} \mathrm{d}\omega, \tag{2.4}$$

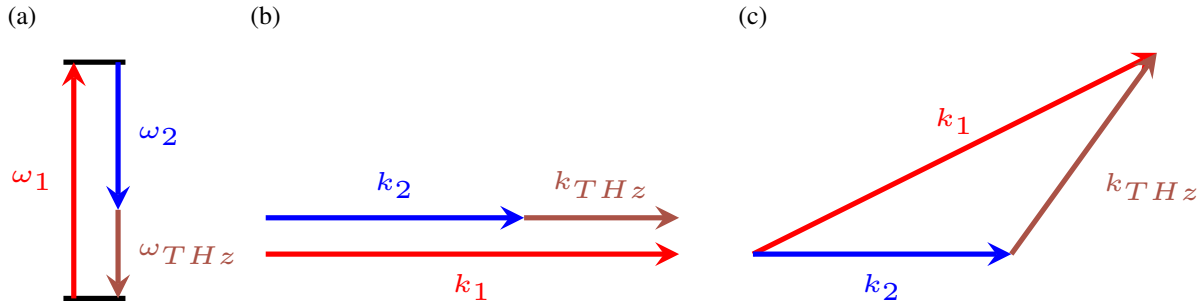

Figure 2.4: Schematic representation of frequency matching (a) and phase matching in the collinear (b) and non-collinear (c) configuration (see eq. (2.6)). Here $\omega_{THz}(k_{THz})$ is the angular frequency (wave vector) of the generated Terahertz, while ω_1 (k_1) and ω_2 (k_2) are the angular frequencies (wave vectors) of the impinging laser and of the laser after the Terahertz is generated. The non-collinear configuration is used, for instance, in tilted-pulse-front generation schemes [93].

substituting eq. (2.4) into the second term of eq. (2.3), we obtain a double integral where the integrand describes a process analogous to the photomixing discussed in section 2.1.1.a). In this case, however, we obtain a difference frequency (Ω) for every pair of plane waves from the input field. The difference term that contributes to the OR polarization $\mathbf{P_{OR}}$ is then:

$$P_i = \epsilon_0 \chi^{(2)}_{i,j,k} \iint E_j(\omega_1) E^*_k(\omega_2) e^{-\mathrm{i}(\omega_2-\omega_1)t} \mathrm{d}\omega_1 \mathrm{d}\omega_2 = \epsilon_0 \chi^{(2)}_{i,j,k} \iint E_j(\omega+\Omega) E^*_k(\omega) e^{-\mathrm{i}(\Omega)t} \mathrm{d}\Omega \mathrm{d}\omega. \quad (2.5)$$

The polarization vector obtained from this tensor formula, is not necessarily parallel to the electric field and this mechanism of intra-pulse DFG is only efficient if the input and output photons respect the frequency and phase matching condition:

$$\begin{cases} \omega_1 - \omega_2 = & \Omega_{THz} \\ k_1 - k_2 = & k_{THz} \end{cases} \quad (2.6)$$

where $\omega_{THz}(k_{THz})$ is the angular frequency (wave vector) of the generated Terahertz, while ω_1 (k_1) and ω_2 (k_2) are the angular frequencies of the impinging laser and of the laser after the Terahertz is generated. Since the second line of eq. (2.6) involves vectors, it can be satisfied by photons that do not propagate collinearly (see fig. 2.4), however, eq. (2.6) as a whole cannot hold for all frequency combinations at once, so the involved photons will progressively get out of phase matching as they propagate and the process will be reversed once

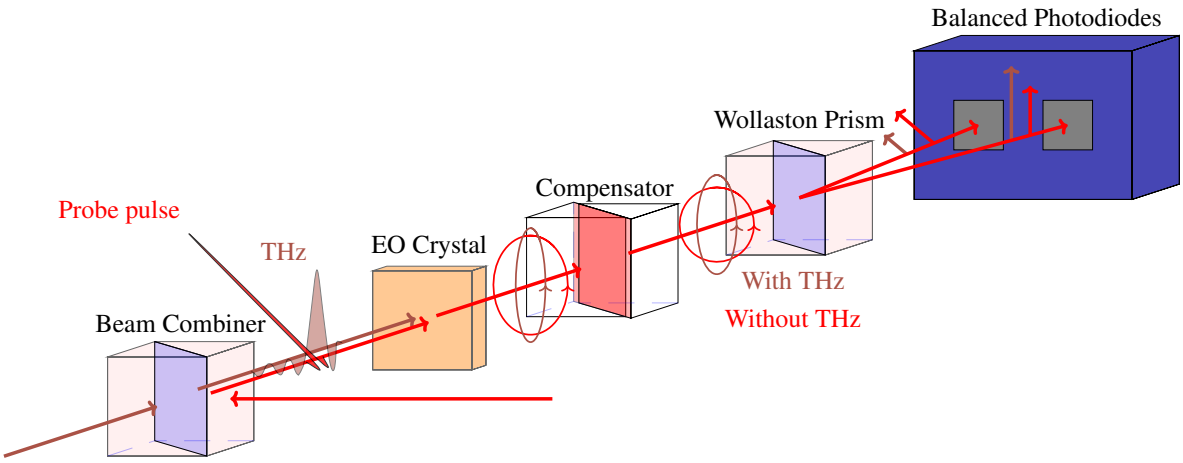

Figure 2.5: Schematic of Electro-Optic Sampling (EOS): the signal and probe are combined along a common path and traverse at the same time an optical crystal. The THz field alters the refractive index of the crystal and causes a change in the polarization state of the probe, which is measured via balanced photodiodes after separation of the two component polarizations by a Wollaston prism.

they propagate enough to accumulate a phase delay of π (this condition defines the coherence length): the latter consideration imposes a limit to the extension of the crystal used for the conversion. More details on the principle can be found in [27, 93]. Since these methods rely on polar materials, they are also affected by optical phonon resonance that suppresses the emission in the region ~5 THz to 10 THz [94]

b) Terahertz detection by an electro-optic crystal

Optical crystals are also suitable for Terahertz detection, although exploiting a different phenomenon, namely the linear electro-optic effect [95, chap. 11]. This is also a second-order nonlinear effect that manifests in non-centrosymmetric media as a variation in the refractive index that is linearly proportional to an externally applied (quasi) static electric field. An optical beam oscillates at frequencies much higher than the Terahertz radiation and sees the latter as a (quasi) static field, so when traversing together a non-centrosymmetric medium, the components of the laser field parallel and orthogonal to the THz field experience different refractive indices and accumulate a relative phase shift proportional to the THz field. To perform a detection, the THz beam and an optical pulsed laser are combined on the same optical path (typically using an off-axis mirror with a hole for the laser to pass through). The technique, called Electro-Optic Sampling (EOS), is schematized

in fig. 2.5. The laser should initially have components in the two directions, parallel and orthogonal to the THz beam, and emerge from the optical crystal with circular polarization when Terahertz is not present. This is usually obtained using an initial linear polarization at $45°$ with respect to the THz beam and a $\lambda/4$ plate after the crystal (a compensator can optionally be installed to help ensure this condition). Then, a Wollaston prism is used to separate the optical beam into two, with polarization parallel and orthogonal to the polarization of the THz beam. The two beams are sent to a pair of balanced photodiodes for detection. Adding the THz field, the electro-optic effect will change the polarization state from circular to elliptic, causing imbalance between the photodiodes, which will allow recovery of the phase shift and, consequently, of the THz field. If the laser has a pulse width of a few tens of fs, the much longer THz pulses ($O(\mathrm{ps})$) can be sampled at different times by changing the relative delay of the two beams along the optical path of the setup, so that the probe traverses the crystal in correspondence to different sections of the signal. The efficiency of the EOS process depends on the phase matching between the probe and the THz field. A good approximation of the phase-matching condition is obtained when the group velocity of the probe pulse equals the phase velocity of the THz beam:

$$v_{gr}(\nu_{probe}) = v_{ph}(\nu_{THz}). \tag{2.7}$$

This means that, as the two pulses propagate through the crystal, individual THz frequencies will *i*) experience a temporal walk-off with respect to the probe and *ii*) be detected with lower efficiency. When the crystal thickness is close to an integer multiple of the corresponding THz wavelength, the response of the detector is suppressed [96]. The thickness of the crystal is also important because using thinner crystals increases the detectable bandwidth at the expense of a lower output. For further details on the physical principle underlying the use of $\chi^{(2)}$ crystals as THz sources and detectors, see references [27, 64, 66, 79].

c) Terahertz generation in air

Terahertz radiation can be generated by focusing high power laser pulses, strong enough to produce an air plasma filament in the region of the beam waist. The free charge carriers of the plasma are acted upon by the laser field own ponderomotive force and, as they are pulled apart, Terahertz radiation is generated together with a wide spectrum of other EM frequencies. The resulting field can be evaluated using a linearised

hydrodynamic model for the plasma dynamics in most common laser configurations [97]. A secondary contribution from photomixing of the remaining parts of the plasma spectrum is also present, with a relative weight that increases with gas pressure [98]. The strength of the THz signal generated in this process can be further enhanced by inducing nonlinear effects in the plasma using a strong bias field [99], whose energy can then be transferred to the THz pulse. Alternatively, by focusing into the interaction region the second harmonic of the pump laser [100], it is possible to produce in the plasma high photocurrents that emit Terahertz at an angle with respect to the forward direction [101–104]. There are contributions from other nonlinear processes, concentrated in the forward direction, but they are much weaker than what is generated by the primary process mentioned above.

The variant of THz generation by second harmonic enhanced air plasma, easily produces field amplitudes greater than $100\,\mathrm{kV\,cm^{-1}}$ achieved with $20\,\mathrm{mJ}$ optical pulses [103] and can reach values as high as $4.4\,\mathrm{MV\,cm^{-1}}$ after careful optimization of the setup (see reference [105]). The described technique of generation by photo-currents in transient gas plasmas remains among the most promising sources of ultra-broadband THz pulses [106–108]. However, it requires high power regenerative amplifiers, which makes it quite expensive to set-up and is definitely not portable. The same considerations apply to recent developments that realize a similar generation scheme using single color filaments in liquids [109, 110].

d) Biased coherent detection technique

Just like optical crystals, Air Plasma can be harnessed to also perform detection in the same spectral range. This is done by exploiting the phenomenon called Electric Field Induced Second Harmonic (EFISH) generation in centrosymmetric materials. In the presence of a strong static component in the electric field $E = E_{st} + E_{dy}$, the third order term of the polarization vector expansion, $P^{(3)} \propto (\chi^{(3)} E^3)$, contains a term $\propto \chi^{(3)} E^3$ which enables Second Harmonic (SH) generation via the effective second order electric susceptibility $\chi^{(2)}_{eff}$, that is proportional to the static field [70]. Since the THz electric field is practically constant over the duration of the ultrafast laser pulses of the probe, it plays the role of E_{st} and the intensity of the probe's SH is modulated by the envelope of the THz pulse. If a periodic bias field is added on top of the THz one, the SH intensity $Y_{2\omega}$ takes the form [76, 78]:

$$I_{det} \propto \left(\chi^{(3)} I_\omega\right)^2 \left(E_{THz} + E_{bias}\right)^2 = \left(\chi^{(3)}\right)^2 I_\omega^2 \left(E_{THz}^2 + E_{bias}^2 \pm 2 E_{THz} E_{bias}\right). \tag{2.8}$$

The SH intensity, measured via standard photo-detectors such as Photomultiplier Tubes (PMT) or photodiodes, is sent to a lock-in amplifier using the bias source as the reference oscillator (*e.g.*: a unipolar square wave with frequency one half of the THz pulse repetition). The lock-in will then filter out all terms in eq. (2.8) but the mixed product, which is proportional to:

$$I_{det} \propto \pm \left(\chi^{(3)}\right) I_{\omega}^{2} E_{THz} E_{bias}. \tag{2.9}$$

The most commonly used medium is a two color, laser induced plasma produced in air by focusing the THz and probe beams between two electrodes, a technique called Air Biased Coherent Detection (ABCD). Here, the low dispersion of air allows detection over the whole THz spectrum. However, large pulse energies (about $100\,\mu\mathrm{J}$) are required to compensate for the low value of $\chi^{(3)} \approx 1.68 \times 10^{-25}\,\mathrm{m^2\,V^{-2}}$ in air, since the bias field is already close to the discharge threshold and cannot be raised. The use of pure nitrogen, argon or krypton to increase the threshold is attested in literature but it gains at most a factor of ~7 while complicating the setup with gas cells and flux/dilution control mechanisms [89].

Since eqs. (2.8) and (2.9) only require for the medium to be centrosymmetric, a suitable solid could be used too, making for a better transducer medium, due to both a higher $\chi^{(3)}$ and dielectric strength in the active region. Prof. Morandotti's group is actively conducting research to implement such a biased scheme, dubbed Solid-State Biased Coherent Detection (SSBCD), into an affordable and compact solid state terahertz transducer [111–113]. The first design was based on silica (SiO_2, $\chi^{(3)} \approx 2 \times 10^{-22}\,\mathrm{m^2\,V^{-2}}$, breakdown field $\approx 200\,\mathrm{kV\,mm^{-1}}$) with deposited gold metallizations for the electrodes, later changed to a thin film of silicon nitride (SiN) with a much higher susceptibility ($\chi^{(3)} \approx 8 \times 10^{-21}\,\mathrm{m^2\,V^{-2}}$). The latter medium, featuring a $1\,\mu\mathrm{m}$-wide slit separating two metal electrodes, allows operation with a bias of $10\,\mathrm{V}$ to $100\,\mathrm{V}$ switching on and off at $10\,\mathrm{kHz}$: such switching can be produced with standard, low cost electronics and prospects the opportunity to more affordable high repetition rate laser oscillators ($E_{pulse} < 100\,\mathrm{nJ},\ \nu_{rep} > 1\,\mathrm{MHz}$) as the pump [114], rather than lab-grade, extremely costly, high power lasers.

e) Terahertz generation and detection by Photoconductive Antenna (PCA)

A Photoconductive Antenna (PCA) for Terahertz radiation consists of a highly resistive direct band-gap semiconductor thin film, most commonly realized out of a III-V compound like GaAs, with two electric contact pads. The film is epitaxially grown on a highly resistive semi-insulating substrate, usually of the same chemical

compound, only differing on the doping (defects). Each photon with energy $\hbar\omega$ larger than the semiconductor gap (E_g) that is absorbed in the film, creates a free electron in the conduction band and a hole in the valence band of the film, making it electrically conductive until the carriers are recombined after a time determined in large part by the density of the crystal defects (fig. 2.6a): with appropriate doping of the film, such time interval can be made significantly shorter than $1\,\mathrm{ps}$. [115, 116]. If a short laser pulse (pump) with duration comparable to the relaxation time is focused onto the inter-electrode gap of the PCA while it contains a bias electric field, a charge distribution becomes available and is accelerated into a pulse of current that lasts at most for the duration of the pulse plus the recombination time, corresponding to a bandwidth of the order of a few THz. As long as a variable current passes through the PCA, it can be considered as a dipole of length L which is in resonance with the electromagnetic wavelength λ_n inside the semiconductor. In particular, the following condition is satisfied:

$$L = m\frac{\lambda_n}{2}, \tag{2.10}$$

where n is the refractive index of the material and $m = 1, 2, 3, \ldots$ is an integer, while the wavelength in the material can be approximated by $\lambda_n \approx \lambda/n$. This, in turn, makes Photoconductives Antennas suitable for both emission and detection of THz pulses. If the bias is provided by an external DC power supply (voltage V), the interplay between the pump shape and the carrier recombination modulates the charge density and the bias voltage accelerates it into a substantial current, causing the emission of EM radiation in the THz range, specifically:

1. Before illumination (fig. 2.6b (1)), the semiconducting antenna gap (of width g) is depleted of free electrons in the conduction band by the bias V, thus establishing an electric bias field of strength $E = V/g$. With a typical supply voltage of $10\,\mathrm{V}$ and a gap distance of $5\,\mu\mathrm{m}$ the electric field strength is, therefore, $E = 2 \times 10^6\,\mathrm{V\,m^{-1}}$. The optical pulse must be focused onto the semiconducting antenna gap in such a way that the spot diameter is slightly larger than the gap distance, so that the metal lines are also illuminated.
2. When the pump meets the antenna gap, the optical energy is absorbed and free carriers are created in the semiconductor material (fig. 2.6b (2)) corresponding to the number of incident photons. The free carriers follow the electric field, creating a short current pulse $j(t)$ in the semiconducting gap material. Typical values for the optical pulse are: Pulse duration $\tau \approx 100\,\mathrm{fs}$, Pulse energy $E_{pulse} \approx 100\,\mathrm{pJ}$, Pulse repetition rate $\nu_{rep} \approx 100\,\mathrm{MHz}$, Average optical power $P_{av} \approx 10\,\mathrm{mW}$.

3. The dipole associated with $j(T)$ emits an electric field as long as the current pulse changes with time (fig. 2.6b (3)). At first, the current increases during the illumination of the gap and emits the first portion of the THz pulse. If the current decreases because the electric field is subsequently compensated by the transferred carriers then the second portion of the THz pulse is emitted with a reverse polarization. The polarization direction of the bias electric field parallel to the dipole axis is imparted to the emitted THz field. Most of the electromagnetic energy is emitted towards the semiconducting substrate material with high refractive index.

The THz electric field radiated by the PCA, can be modelled using the laws of classical electrodynamics, resulting in the following, simple equation:

$$E_{\mathrm{THz}} = \frac{1}{4\pi\epsilon_0}\frac{A}{c^2 Z}\frac{\partial J(t)}{\partial t} = \frac{A}{2\pi\epsilon_0 c^2 Z}\frac{e\mu E_b \partial N(t)}{\partial t} \tag{2.11}$$

where:

$$J(t) = e\mu E_b N(t) \tag{2.12}$$

is the time dependent current density. In these equations, A is the area in the gap illuminated by the laser light, ϵ_0 is the vacuum permittivity; c is the speed of light in vacuum; Z is the distance between the field point and the THz source; N is the density of the photo carriers (which depends on the laser pulse shape and carrier lifetime of the semiconductor substrate); e is the electronic charge; μ is the electron mobility, and E_b denotes the electric field bias. A detailed study on the effect of the pump power and bias voltage on the THz field emitted by different kinds of PCAs is available in reference [117]: for example, it reports the generation of THz radiation with a power of $0.6\,\mu\mathrm{W}$ from a strip line PC antenna that was biased with $100\,\mathrm{V}$ and excited by a $15\,\mathrm{mW}$ pump laser. By increasing the power of the pump beam or by increasing the voltage bias, the strength of the THz field generated by a PC antenna can be increased. However, in the case of PC antennas on a semi-insulating GaAs substrate, the power of the emitted THz radiation saturates with the increase in power of the pump beam [117] due to the screening of the bias field by the induced photo-carriers. Also, a PC antenna cannot be biased beyond the breakdown voltage of the substrate. For example, a LT-GaAs has a breakdown voltage of $500\,\mathrm{kV\,cm^{-1}}$ [117]. Hence, in order to prevent a PC antenna with a gap size of $100\,\mu\mathrm{m}$ and grown on LT-GaAs from getting damaged, it should not be biased beyond $5\,\mathrm{kV}$.

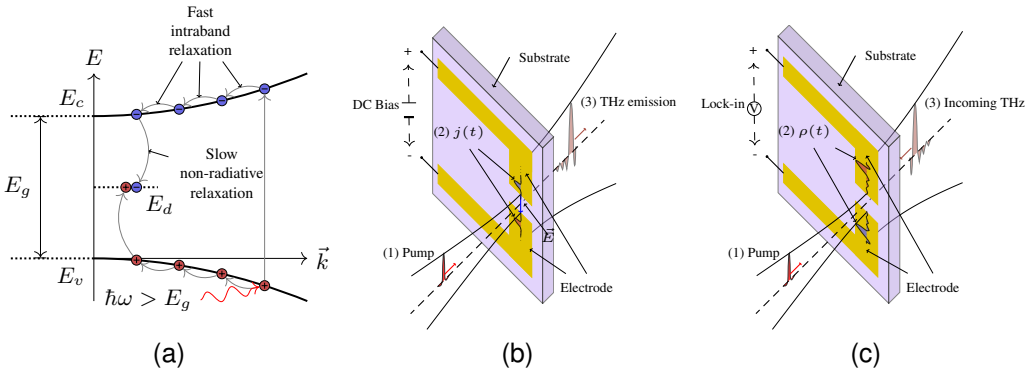

Figure 2.6: (a) Band diagram of a Photoconductive Antenna (PCA): the fast intraband transitions cause emission of the signal until the non-radiative relaxation stops the process. (b) Schematic diagram of a PCA used in 'emitter' configuration: an external bias separates the carriers created by the pump laser, thus giving time for the intraband transitions to develop a THz pulse. (c) Schematic diagram of a PCA used in 'detector' configuration: the THz electric field separates the carriers generated by the pump laser, in turn producing a ΔV at the PCA terminals that can be detected using a lock-in amplifier.

As mentioned earlier (page 22), the THz field is practically static with respect to the frequency and the width of the probe pulse, so we can set up the antenna in such way that the THz field plays the role of the bias.

1. Before illumination, the semiconducting antenna gap (of width g) contains no free electrons or bias field. Both optical (fig. 2.6c (1)) and THz (fig. 2.6c (3)) pulses must be focused onto the semiconducting antenna gap, coming from opposite directions, in such a way, that the spot diameter is slightly larger than the gap distance, so that the metal lines are also illuminated.
2. When the pump meets the antenna gap, the optical energy is absorbed and free carriers are created in the semiconductor material (fig. 2.6c (2)) as in the emission case. Since no bias field is applied, the free carriers can now drift only if the THz pulse overlaps the semiconductor gap material at the same time, moving positive and negative carriers apart towards the electrodes and creating a small ΔV proportional to the instantaneous THz electric field.
3. The voltage between the PCA terminals, roughly behaves as a train of pulses, with height proportional to the probed THz field and repetition frequency equal to the one of the excitation laser. Since this is a periodic signal, lock-in amplifiers are the perfect choice to perform the measurement, using as reference either the pump laser clock or an additional chopper. In case the emitter is also a PCA, the 'chopper' can be provided by modulating the emitter bias using a square wave pattern.

Every technique and device discussed throughout the current chapter is employed to realize THz systems for a diverse range of applications: in order to choose one over the others, one must consider what are the requirements of the application to strike a balance between the strong and weak points of each technique, so that the intended result can be achieved, without building an overly complex and costly system. In the next chapter we will identify the requirements for our project and describe the system we envisioned and used in our laboratory.

Chapter 3. Description of the setup

The project which this work is part of, is still in its infancy, where our intent is to provide a proof of concept for the use of THz radiation as a probe for temperature in biological tissue (a technique also referred to as Teramometry). Although previous experiences show that this can indeed be done [33, 35], further investigation is required, to provide a complete and reliable model for the heating of skin during Photothermal Therapy, before Teramometry can be used on patients.

To carry out the experiment that are necessary to perform the study, we developed a dedicated system, capable of delivering the IR heating beam and to measure the interaction of THz pulses with the heated surface. In our design we considered all the types of measurements that were envisioned in the initial experimental plan. However, the necessity to change the procedure to perform a measurement may arise, following further experiments. In addition, new types of measurements may be introduced. Therefore, we had to avoid design choices that would pose difficulties for modifications that are likely to be necessary in the future. Several requirements for the design stem from the decision to perform our experiments in conditions that are as close as possible to those that would be encountered in the intended use of the system in a clinical environment. The control software followed similar principles to allow easy maintenance, extensibility and to present an interface that makes performing standard measurements easy and customizations possible.

As mentioned in chapter 1, the ultimate aim is to use the system in real time, on oncologic patients during treatment, so the optimal system would have to be compact, mechanically self contained and stable, to allow easy placement in the proximity of the treated part. Ideally the THz emitter and receiver should reside in a module separated from the laser for ease of positioning, but given that we are still operating on skin samples from a porcine model, at this point it is premature to solve these kinds of issues. What really cannot be worked around is the requirement that measurement needs to be fast, otherwise it would not be possible to demonstrate a real time monitoring application. At the same time, we must ensure accurate reconstruction of the THz pulses to extract depth from the delay between pulse and reflections, as well as temperature information from the modification of its features. This implies the use of a THz-TDS system for the measurement, with its ability to retrieve the shape of the pulse with sub-picosecond accuracy.

Although normal operation with patients needs to be fast, there may be a necessity to verify that the THz source is in good condition or recalibrate the detector after maintenance. Thus, another desired feature is the ability to switch from a fast scanning mode to a 'slow' or, better yet, 'accurate mode', so that such operations can be carried out on site. Such operation should not require too much extra equipment and should be possibly performed within a couple of tens of minutes. The latter is not strictly necessary during the current proof-of-concept phase, but it is still quite convenient to speed-up and make the characterization of the model samples more accurate with less effort: this implies the use of two different delay lines for the THz-TDS, each targeting a different working mode. It should also be noted that a slow, precise delay line could be used to frame the pulse within a fast, less precise one, which can in principle cover a shorter span and require more careful positioning.

With regard to the THz source and detector, the requirement for a compact and easily positionable system essentially rules out most detectors, except Photoconductives Antennas. Since the physics of the antenna will limit the detectable THz band to about $4\,\mathrm{THz}$ to $5\,\mathrm{THz}$, it would be pointless to implement a source with a broader spectrum, so the natural choice is to use a PCA emitter, which also helps in keeping the system compact.

With these considerations in mind, we choose to base our system on the *Measurement Kit for Research and Development* (MKRD) [118] commercialized by TeTechS, a Canadian company that manufactures THz equipment for industry and research. The kit in its base configuration is a complete time-resolved THz-TDS system that already fulfills several of the requirements exposed above and can be modified by incorporating custom components as the need arises. Moreover, since we expected to customize the system over time, having a well-established reference setup would allow us to purchase hardware upgrades as required in the future.

Let us proceed to the description of the system and how it was implemented.

3.1 Optical path

Figure 3.1a is a photograph of the optical path of the THz-TDS taken from above after customization.

The box marked with 1 is the bench top laser module providing excitation beams to operate the antennas. It has a wavelength of $785\,\mathrm{nm}$, average output power of $40\,\mathrm{mW}$ at a $100\,\mathrm{MHz}$ pulse repetition frequency (PRF), and a nominal pulse width of $100\,\mathrm{fs}$. The beamsplitter at F.3.1a-2 separates the laser in two equal beams that are routed to the THz emitter (model T-Era-100A-800-air) on the THz branch, and to the receiver (model T-Era-20D40P-800-air) on the

probe branch at F.3.1a-3 and F.3.1a-4, respectively. Due to losses, the average optical power reaching each PCA substrate is about $15\,\mathrm{mW}$, resulting in a typical THz emission power of $90\,\mathrm{mW}$ at peak and $5\,\mathrm{mW}$ on average.

After the emitter, the THz branch propagates the THz pulses towards the receiver via a series of parabolic off-axis mirrors and includes two sample holders for measurements in both transmission and reflection (located at F.3.1a-5 and F.3.1a-6 respectively). The probe branch ensures that the laser reaches the back side of the receiver in time with the signal, where it provides a time window of $100\,\mathrm{fs}$ to sample a section of the THz pulse. The slow delay line (SDL) placed at F.3.1a-8 is used to perform accurate Time Domain Spectroscopy (TDS) measurements. It consists of a Zaber motorized translation stage (model T-LSM050A), with travel range of $5\,\mathrm{cm}$ and spatial resolution of $0.1\,\mu\mathrm{m}$, allowing to safely change the relative time position of THz and probe pulses in steps of $5\,\mathrm{fs}$.

One of the upgrades required by our application is the fast delay line (FDL) placed in the probe branch at F.3.1a-7. This is a magnetically operated oscillator that can perform several sweeps per second as opposed to the SDL at F.3.1a-8, that takes at best a couple of minutes to complete one sweep[1]. The two delay lines emphasize different aspects of the measurement: the SDL allows long sweeps with precise readings of the THz field, resulting in a more faithful and detailed representation of the temporal and spectral features of the pulses, while the FDL sacrifices some accuracy to achieve the kind of fast operation needed for the intended application.

The parabolic mirrors at F.3.1a-9 and F.3.1a-10 were added to deliver THz radiation onto the sample and pick up the reflection at angles of $45°$, while leaving a clear line-of-sight in front of the sample holder for the near infrared (NIR) laser at F.3.1a-11, used to simulate PTT on our samples. The sample holder itself, is mounted on a X-Y motorized stage at F.3.1a-12[2] specifically added to perform raster scans of the target area and obtain a map of the area that has been heated, with a complete spectral analysis performed at each pixel in the scan.

The MKRD comes with a control box containing the essential electronics for the operation of the system, with the exception of the controllers for the Thorlabs motors used in the X-Y raster-scan subsystem, that sit on the table top and are connected directly to the computer via USB. A view from the top and of the front panel of the control box are shown in fig. 3.1b and 3.1c, respectively. The power supply unit, feeding the laser module and the rest of the box components from a standard $160\,\mathrm{V}$, $60\,\mathrm{Hz}$ outlet, is integrated and is visible below the rest of the equipment at the F.3.1b-1 mark. To ensure safety, the laser power line contains two additional switches and a

[1] The FDL shown in fig. 3.1a was replaced later with a different model, without affecting the argument of the current paragraph.

[2] The XY-stage is made by combining two stages by Thorlabs at right angles between them: a MTS25B-Z8 with MTS25B-Z8 travel range for the X direction and a MTS50B-Z8 with $5\,\mathrm{cm}$ travel range for the Y direction.

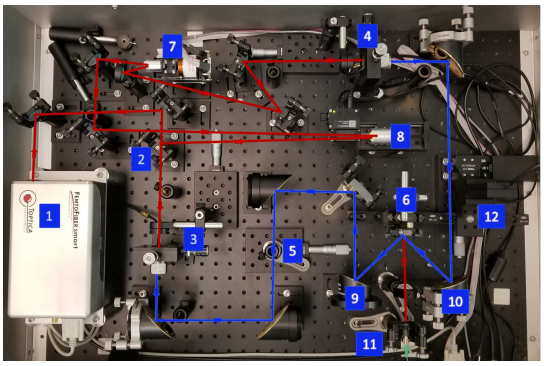

(a)

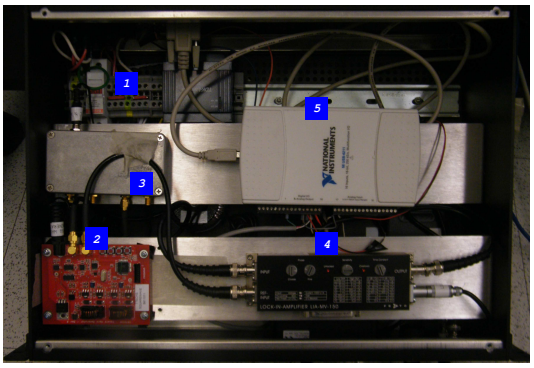

(b)

(c)

Figure 3.1: (a) Top view of the TeTechS system. a-1: Femtosecond laser. a-2: Beam splitter. a-3: THz emitter (typical peak/average power of $5\,\mathrm{mW}/5\,\mathrm{mW}$). a-4: THz detector. a-5: Sample holder in transmission geometry. a-6: Sample holder in reflection geometry. a-7: Fast optical delay line (FDL). a-8: Slow optical delay line (SDL). a-9, a-10: $45°$ off-axis gold mirrors. a-11: NIR laser diode. a-12: Motorized imaging stage. (b) Top view of the TeTechS control box. b-1: Power supply unit (in the background). b-2: Square pulses generator for Bias timing and lock-in reference. b-3: Amplifier that turns the square wave clock into the Bias. b-4: Integrated lock-in amplifier. b-5: Integrated USB National Instruments (NI) Data Acquisition (DAQ) unit for signal sampling and FDL control. (c) front panel of the TeTechS control box. c-1: Safety switch and adjustment knob to regulate the power supplied to the laser module at a-1. c-2: USB output to connect the DAQ to a computer. c-3: Square Pulses output for use as reference with an optional external instrument. c-4: Signal output for use with optional external lock-in.

regulation knob on the front panel, marked with F.3.1c-1. Since one of the two switches is operated via a key, it is impossible to turn the laser on by mistake.

The red board marked with F.3.1b-2 emits a continuous train of square, unipolar pulses split over two outputs. The first is amplified by the module marked with F.3.1b-3 to provide the bias to the emitter. Thanks to its temporal structure, the bias effectively turns on and off the antenna at each pulse, effectively modulating the output and serving as an electronic chopper. The second pulse train is sent to the integrated lock-in amplifier to be used as the reference oscillator. Normally we operate the bias at a PRF of ~$1.314\,159\,\mathrm{kHz}$[3], with a peak value matching the one required by the antenna in use, namely $\pm 50\,\mathrm{V}$ for the T-Era-100A-800-air, but the board has buttons that allow the tuning of the square pulses parameters. Although this requires opening the box, it is not a concern since there is little reason to change the repetition frequency or the bias level except in the infrequent case of the emitter being replaced.

The lock-in (marked with F.3.1b-2) is directly connected to the receiver antenna via the front panel connector F.3.1c-4. Since the emitter bias is chopped and the probe enables the receiver over a narrow window, the amplifier can lock on the bias frequency and produce an output voltage proportional to the average value of the THz field inside the probe window[4] that is rerouted to a Data Acquisition (DAQ) card produced by National Instruments (NI), marked with F.3.1b-5 and connected to a computer, that is responsible for the actual measurement, via the USB port at F.3.1c-2.

The lock-in is a compact device, well suited for integration and, just like the bias board, its settings are changed via built-in physical switches. For the measurements planned in developing our project, this is inconvenient, since we need to characterize our samples with different settings of the lock-in, from coarsest to finest, in order to have an accurate description of the system response and determine how much the quality of the measured signal can be lowered before functionality is lost. As it turns out, it is quite simple to bypass the integrated lock-in and use an external module, just by unplugging the input, reference and output cables from the integrated module and connecting them to the corresponding ports in the external amplifier. We used a Stanford Technology SR865 as the external lock-in, to exploit its high sensitivity ($1\,\mathrm{nV}$) and low noise ($2.5\,\mathrm{nV\,Hz^{0.5}}$ at $11\,\mathrm{kHz}$ with $10\,\mathrm{mV}$ input range) to establish the 'actual' response of the sensors in our setup.

[3] Originally the bias PRF was 1 kHz, but it caused some anomalous readings at times, because it is an integer sub multiple of the laser PRF The final value was chosen as $(1 + 0.1\cdot\pi)$ kHz to reduce the chance that in the future it would match the PRF of an hypothetical replacement laser module.

[4] Note that the much higher PRF of the probe means that one bias cycle contains samplings of many signal pulses. The lock-in is essentially performing an average of the input: as long as the signal pulses are produced equally, the output is still proportional to the THz field inside the 100 fs time window.

Since all the data analysis required for the intended use of the system involves the ratio of two readings, we did not perform an absolute calibration of the instrument and expressed the THz field in arbitrary units instead.

3.2 The software

TeTechS provided a program written in LabView (a so called Virtual Instument (VI)) to operate the system, offering the basic functionalities to position the SDL. It is possible to perform a scan and save it or, alternatively to save an undetermined number of subsequent scans to the same file. Such software was originally intended for use in routine measurements for the characterization of materials or to perform spot-checks in a production line. However, the type of measurements we would perform on a daily basis required a higher degree of flexibility of operation and the ability to handle a much higher volume of data than the one envisaged by the original developer. By inspecting the source code, we identified several possible avenues for improvement and proceeded to implement the ones that were deemed more useful for us at the moment.[5]

LabView code, rather than a textual description, is represented as a metaphor for a virtual electronic instrument, with a "front panel" visually depicting the graphical User Interface (UI) and a circuit schematic called the "diagram", with "wires" connecting the blocks that represent operators, function calls and the "terminals" that connect implicitly to the input and output fields on the front panel (called "controls" and "indicators", respectively). This kind of representation is intuitive and relieves the programmer from caring about several low-level details, but has the downside of requiring relatively large portions of the screen to lay out even moderately complex algorithms and make searching the code for patterns somewhat more difficult than in text-based languages.

The principal issues we found in our inspection were the monolithic structure of the program, with most operations fully spelled-out at multiple locations in the code (*e.g.*: conversion from position to time delay and *vice versa*, and the value of constants) and the overuse of indicators as replacement for variables.[6]

Besides increasing the overall complexity of the diagram, each of the repeated code snippets constituting the first issue can have a significantly different layout, making it difficult to recognize all instances when changing how an operation should be performed or applying a correction.

[5] We could inspect and modify the original software under the agreement that all improvements would be made available to TeTechS for use in subsequent releases.

[6] Strictly speaking, LabView does not have the concept of variable.

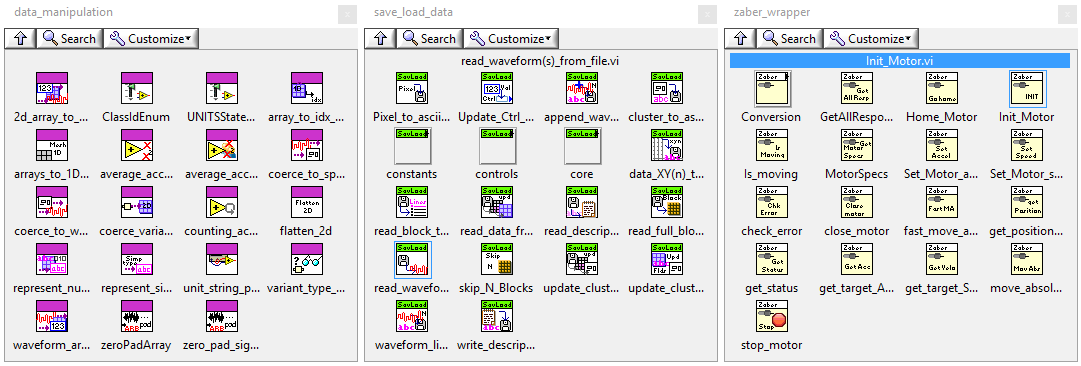

Figure 3.2: Some of the helper functions developed to rationalize the code: `data_manipulation`, `save_load_data` and `zaber_wrapper`, from left to right respectively. The entries labeled 'constants', 'controls' and 'core' in the `save_load_data` panel represent sub-palettes for functions that are used almost only internally within the library.

This is especially aggravating when dealing with motion control and data acquisition routines that are composed by several low-level instructions for relatively simple operations and require several parameters to be passed around correctly.

The use of controls as variables, instead, poses a problem in terms of efficiency, because the latency for accessing a front panel control is significantly larger than the one for using data structures in the diagram.

The inefficiency is negligible when performing routine operations involving a few tens of consecutive scans, but quickly adds-up when the data volume scales by one or more orders of magnitude. Moreover, the code required to access the controls produces additional repeated code snippet, thus compounding the previous issue.

The first step was a code review with the aim to identify repeated code and factorize it out in a set of well-defined sub-VI, especially for the interface with the motors. We identified a few key areas where Sub-VI would be beneficial and built corresponding dedicated libraries (fig. 3.2). The most important are: *i*) the wrapper libraries for the operation of the Zaber and Thorlabs motors in the setup (`zaber_wrapper`, `thorlabs_wrapper`), *ii*) the library for saving data to ASCII files and reading them back (`save_load_data`) and *iii*) the generic `data_manipulation` library; these ensure structured interaction with the hardware and standardized data treatment. The `graph_handling` library was useful to simplify the management of the plot areas, while the VIs that do not fit in any of the other libraries, or are not ready to be split into their own, are placed in the `utilities` library.

Table 3.1: Indicators of complexity of the code before and after the initial refactoring.

Metric	Original	Refactored
Size of diagram (pixels)	14124×7744	5042×1281
Local variables	545	61
Diagram depth	12	8
Nodes	1715	340
Controls	47	26
Indicators	102	13

After this cleanup, the new program, renamed to **`THz_imaging_center`**, had the exact same behaviour as before, but the code was considerably less complex, visibly more responsive and more amenable to further modularization (see table 3.1). While the libraries extracted from the original code were beneficial, there is still some degree of repetition for common tasks, which is a problem for future modifications. Also, it does not affect the necessity to reference the same controls in several places throughout the program: this, in turn, either involves the use of many wires (visual clutter) or references (slower execution).

LABVIEW has the peculiarity that all top-level loops are executed concurrently, so we can have one loop dedicated to each task, as long as they can share controls or send data and instructions to each other. However, for the sake of clarity, we also want to limit the screen area occupied by the diagram and the number of wires that must be drawn to represent variables.

We address the first constraint by encapsulating the operations specific to each task (and only those) inside a dedicated sub-VI that can get as complex as needed without expanding the area taken in the main diagram. These task-oriented VIs can require many parameters (*e.g.*: the scanning procedures can have up to nine parameters each, plus the configuration of the DAQ). To address the second constraint, the controls corresponding to the parameters have been grouped into clusters defined in a master copy (a so called TypeDef), so that any change on the master is automatically propagated throughout the software. In this way, it is easy to replicate elements of the sub-VI interface on the panel of **`THz_imaging_center`** and only one wire is necessary to transport the data. Communication between sub-VIs running in parallel is achieved through the LABVIEW built-in queue data structure: once a queue is created, a reference to it can be passed to several sub-VIs, giving them the possibility to put/get data of a predetermined type in/from the queue. For instance, the three VI that implement scanning

procedures use a certain queue to send data into the plotting module.

In short, our strategy involved the identification of major functionalities that could be implemented as separate sub-VIs, running in parallel and exchanging data according to a pre-determined protocol. In this way, no matter how complex one of the operations may become, the others can still use it the same way or with very little change, making the software easier to modify and extend with new functionality. We identified six areas to work on, namely:

1. the User Interface,
2. the plotting of data,
3. the writing of data to disk,
4. the slow scan procedure,
5. the fast scan procedure,
6. the image scanning procedure.

3.2.1 User Interface

The main acquisition program purpose is to present an interface for users to perform specific operations, such as setting the parameters that govern a scan procedure (either the slow or the fast one), start and stop the scan, display the resulting measurement(s) as the scan progresses, save the scan to a file. Most of those tasks are performed by separate modules coordinated by the main program UI, according to the actions of the user.

Each module is assigned an area of the front panel that contains its user-facing controls in a tabbed panel, so that seldom used controls are available, but hidden behind the ones that are employed more frequently. To provide visualization of the signal and its spectrum (plotting module), two plotting area indicators are placed in the center, flanked on the right by the controls for output file management at the top (F.3.3-3), image scanning in the middle (F.3.3-4) and fast scanning at the bottom (F.3.3-5). The controls for the slow scanning are located at the top of the right side (F.3.3-6). In fact, the assignment of one area per one module is not rigorously true: for instance, the "**`Save Scan`**" button in the slow scan interface can be used to save the last fast scan too, and the fast scan itself is actually implemented as two cooperating modules.

To help in the measurement preparation phase, we also implemented some ancillary features, such as the ability to perform single shot and continuous measurements of the THz field at a single position, to perform basic

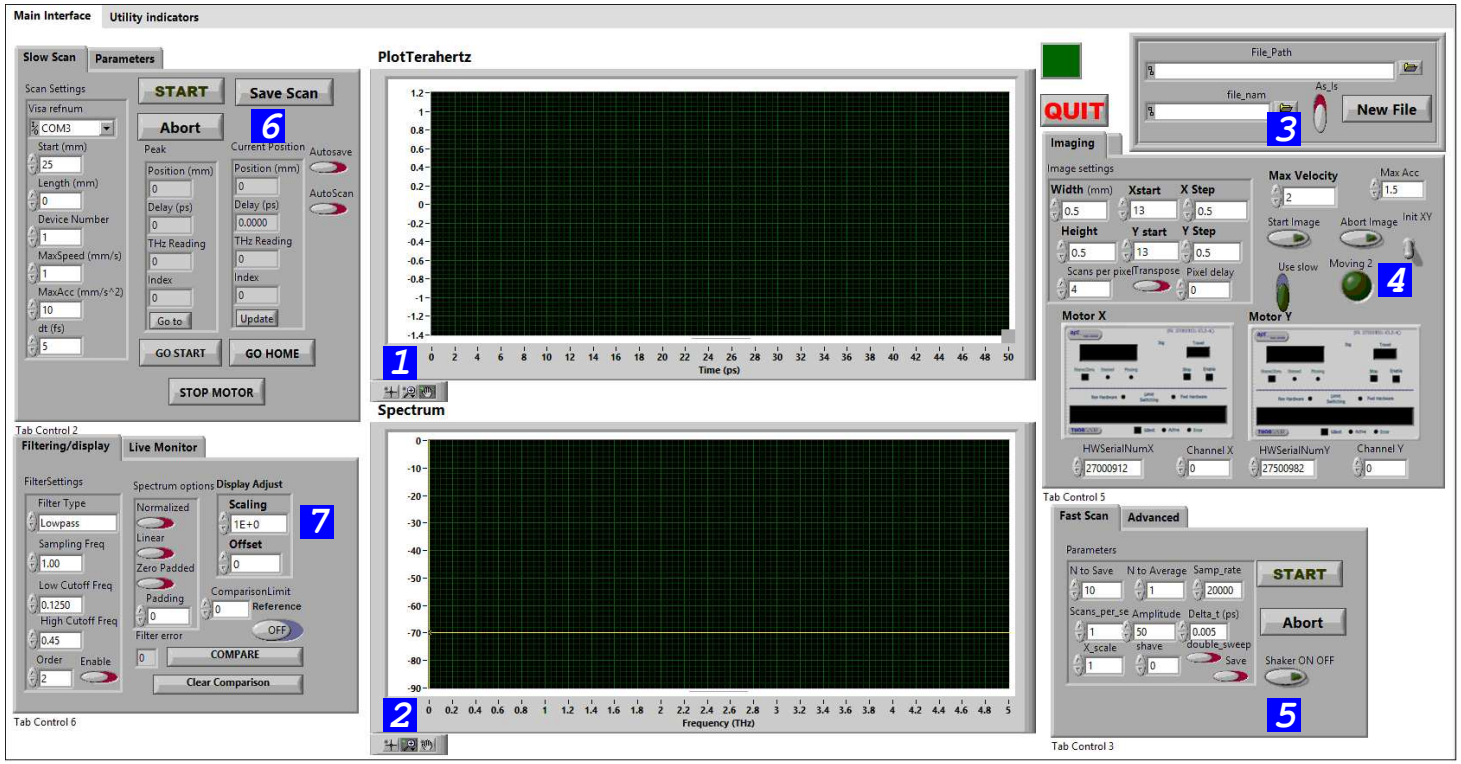

Figure 3.3: User Interface (UI) of the main program. Each panel contains controls for one main functionality (slow scan, fast scan, imaging, plotting), with one panel reserved for grouping the controls for the ancillary features. To keep the UI as clean as possible, seldom used controls are placed in secondary tabs.

filtering of the signal and load previous data for comparison. These are grouped together in a dedicated panel at the bottom of the right side (F.3.3-7) and will not be discussed in depth; suffice to say that in their default settings they have no effect on the output.

Behind the scenes, user interaction with a control creates what is called an event, that is transmitted to a specialized LABVIEW structure without need of a wire to be handled. The structure receives a reference to the control that generated the event and the data it carries and can perform any operation, including create new events programmatically. The diagram of **THz_imaging_center** contains two such structures, one to handle the long-running actions of the scanning procedures, the other dedicated to actions that are completed immediately, such as checking that the new velocity of a motor is safe or sending data/instructions to the other modules. This separation was kept to allow performing operations such as opening a new output file or saving the data measured so far, while the slow scan is ongoing, without apparently "freezing" the UI. The rest of the diagram just handles initialization and runs in parallel the modules implemented as sub-VIs.

3.2.2 Graphing module

The sub-VI named **Graphing_center** is responsible for preprocessing and plotting scan data. It consists of two loops (see fig. 3.4): the first (upper) waits for data to be available in the input queue (**PlottingQueue**) and places it inside a custom event that is sent to the second (lower) loop where it is preprocessed and plotted. This extra step allows the event handler to monitor the filter settings and plot again the last data when changes are detected. As shown in the inset of fig. 3.4, besides the reference to the communication queue (named **Queue in**), **Graphing_center** receives as input references to the two plotting areas, to the plot options and to the filter settings that are present on the front panel of **THz_imaging_center**.

The queue passed to **Graphing_center** accepts data in the LABVIEW type called waveform, so any other module with access to the same queue, can bundle its own data into a waveform using standard tools, add it to the queue and rest assured that it will be filtered and plotted together with its power spectrum.

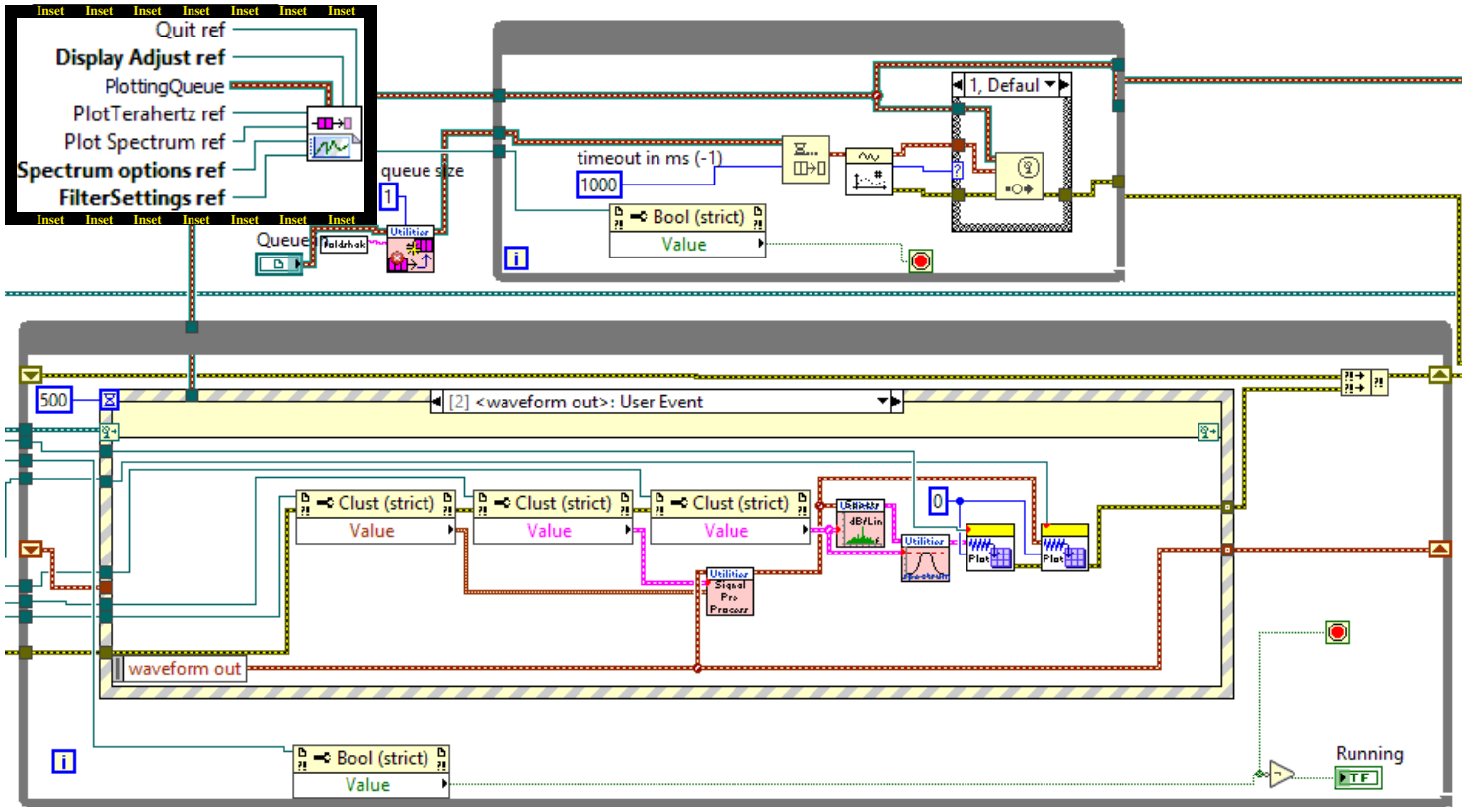

Figure 3.4: Detail of the diagram of the **`Graphing_center`** sub-VI (the initialization part is not shown). The upper loop is responsible for waiting on the input queue: as soon as data become available, they are extracted and sent to the lower loop via a custom event. In the lower loop the data are filtered (by default using the null filter) and plotted alongside their power spectrum. The inset at the upper right corner shows the input terminals of the sub-VI.

3.2.3 Output file management module

The only required input of the sub-VI named **`OutputManager`** is the data queue reference (see inset in fig. 3.5). However it is fairly complex, since it manages the critical task of writing data to disk correctly. It consists of a main loop (fig. 3.5) that polls the input queue for data and performs different actions depending on what it receives (in contrast to **`Graphing_center`**, which performs the same set of operations every time).

The queue is configured to accept data consisting of a cluster containing an instruction and its accompanying data; the latter can be of any type and can be optional for some commands. Combining these commands, it is possible to save data in a structured ASCII file, according to a format described in Appendix A. Some of the command are almost only used internally by **`OutputManager`**. The most commonly employed in the other modules (and possibly in code added by future users) are as follows:

`New`: the optional argument represents a file system path. Reception of this command causes **`OutputManager`** to close the currently open file, if any, then open a new one; if the optional argument does not contain a valid path, a prompt is displayed so that the user can provide one.

`OpenGroup`: starts a structured data block in the current file. The argument is mandatory and consists of a string array of two elements, representing the opening and closing tag of the block: if only one string is provided, the second is assumed to be the empty string (“”). The opening tag is immediately written to file, the closing tag is stored in a stack for later use.

`CloseGroup`: closes the innermost open data block, the argument is ignored. The latest closing tag is retrieved from the stack and written to the current file, thus closing the block.

`Write`: writes the data from the mandatory argument to the current file. The argument is converted to a string with an appended newline. If the argument is an array of numbers, it is converted to a Comma Separated Values (CSV) table, if it is a waveform it is first converted to a two-dimensional array, then to a CSV table. This command is used internally by `OpenGroup` and `CloseGroup`, so they imply a newline.

`Close`: closes all currently open data blocks and the currently open file, if any, ignoring the argument.

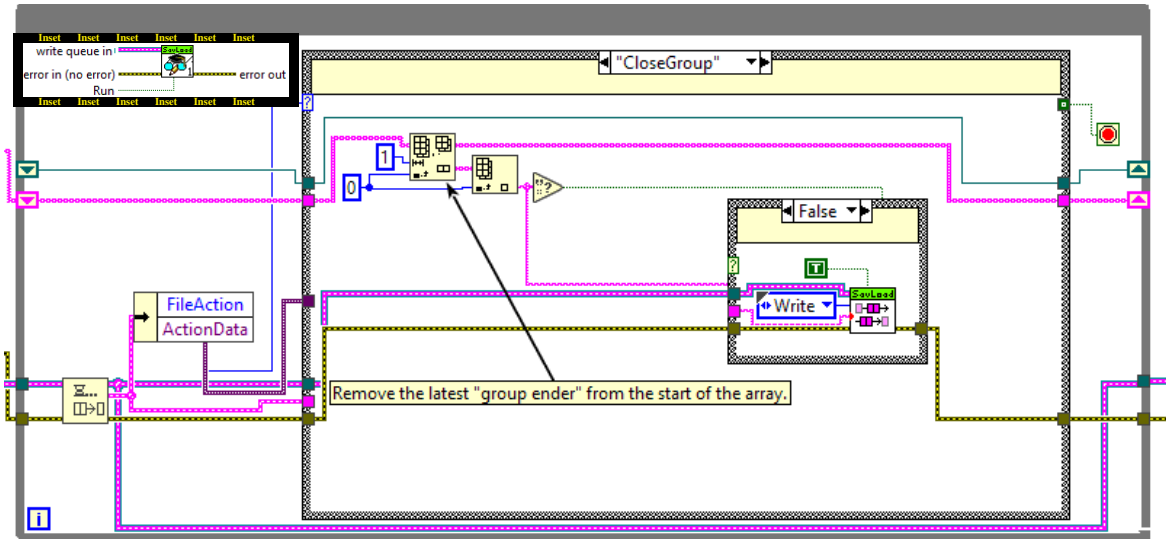

Figure 3.5: Detail of the diagram of the **`OutputManager`** sub-VI (the initialization part is not shown). The inset at the upper left corner shows the input terminals of the sub-VI.

3.2.4 The slow scan procedure

The measurement of THz pulses is the most fundamental task of our system and the general procedure to scan a THz pulse using a PCA has been described on page 22 in the context of EOS. Although the physical process is different (see page 28 for details), it is still activated by a probe laser pulse overlapping a short portion of the signal, and the relative position of the overlap is set by changing the length of the optical path followed by the probe using a retro reflector on a motorized stage (delay line); in our case the stage is mounted so that a positive displacement of d would produce a positive time delay $t = {}^{2d}/_{c}$ of the probe as it travels to the reflector and back.

Ideally, to perform the measurement, the delay line would stop at a given position and wait for the DAQ to clear his buffer and collect enough new data to average out random fluctuations. For a lock-in, it is common to wait three integration times (t_{int}) to allow clearing the buffer and one more to perform the actual measurement: a typical scan containing thousands of samples can easily take several minutes to complete and this is not good for an application meant for use on patients. To save time, we move the delay line at constant speed (v_{dl}) and sample the output of the lock-in at a given rate ν_s, chosen so that to each sample corresponds the desired delay step $\mathrm{d}t$.

It should be noted that using this scanning mode, the lock-in is not averaging data collected only at the planned sampling position, but also from neighboring parts of the pulse positioned before or after the sampling position, depending on the direction of motion of the delay line. Since this 'sliding window' effect depends on the scanning speed, it will be discussed further when describing the fast scanning procedure (section 3.2.5).

The sub-VI in charge of the procedure is **slow_scanner**, whose main loop is displayed in fig. 3.6. The parameters for the motion and the DAQ (see inset) are sent to **slow_scanner** directly from the **Scan Settings** and **DAQ settings** TypeDefs in the front panel of **THz_imaging_center** (see fig. 3.3)[7], where the correct value of ν_s has been evaluated during the consistency checks performed on the data as they are entered by the operator[8], according to the formula:

$$\nu_s = \frac{2v_{dl}}{\mathrm{d}t \cdot c}. \tag{3.1}$$

The DAQ is configured to sample the output of the lock-in continuously, then the data acquisition is started at the same time the motor begins moving by the sub-VI **Initiate_slow_scan**, (marked with F.3.6-1) just outside the loop. Since the motor controller stops autonomously at the end of the scan, the loop is configured to run while the delay line is in motion. At each iteration, the data available in the DAQ buffer is retrieved, appended to what was previously collected and sent to **Graphing_center** via the dedicated **PlottingQueue** at point F.3.6-2, F.3.6-3 and F.3.6-5, respectively. The conditional structure marked with F.3.6-4 is only relevant during the last few cycles, since it checks that the number of samples collected so far does not exceed the expected amount[9] and trims the waveform accordingly.

A reference to the input queue to **OutputManager** (**write queue in**) can, optionally, be passed to **slow_scanner** (see inset on fig. 3.6) along with a boolean switch named **Save (optional)**. If the queue is passed and **Save (optional)** is set to True (default False), the data are sent to **OutputManager** at the end of the scan, and, there, written to file: this is useful in combination with the **AutoScan** and **Autosave** controls in the front panel of **THz_imaging_center** (see fig. 3.3) that cause a slow scan to be repeated indefinitely and the collected data to be saved to file, respectively.

[7] The DAQ settings are not visible in fig. 3.3 since they are in the secondary tab.
[8] It seems better to have the scan parameters inspected and corrected as they are entered, rather than fail when a scan is requested.
[9] This is possible because the DAQ buffer is being autonomously filled by the hardware in between iterations of the main loop of **slow_scanner**.

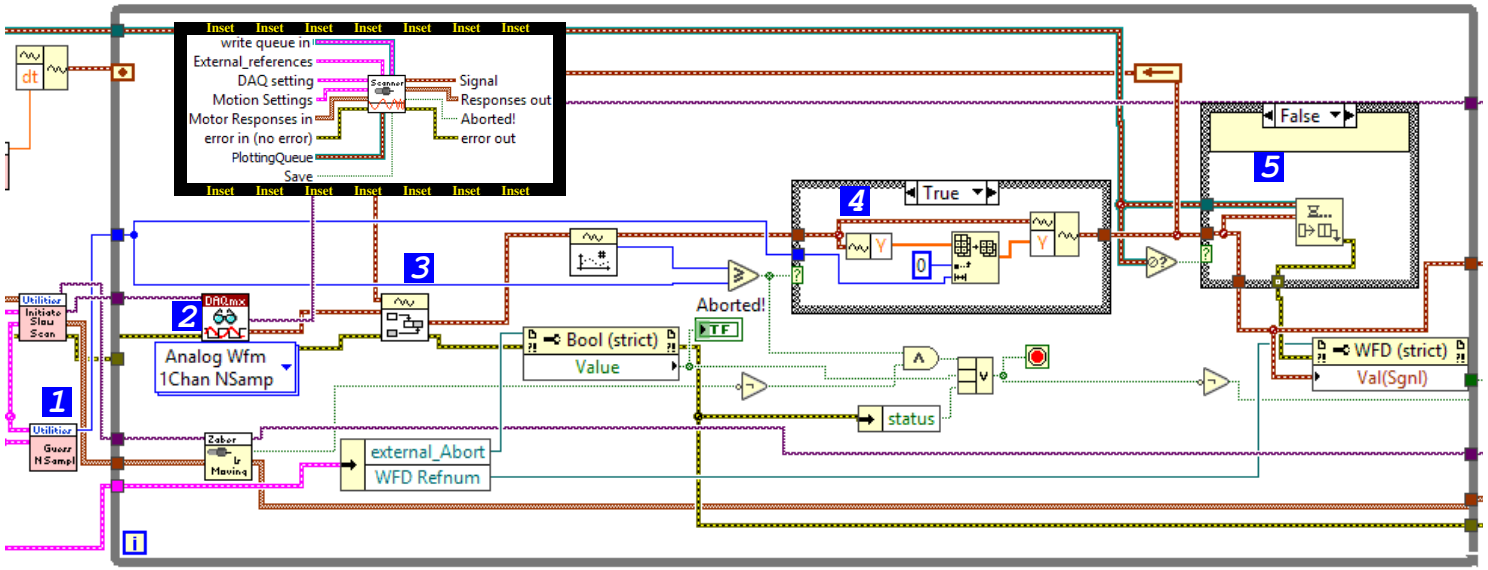

Figure 3.6: Detail of the diagram of the **`slow_scanner`** sub-VI (the initialization part is not shown). 1: Sub-VI **`Initiate_slow_scan`** starts the delay line motion and the acquisition by the DAQ hardware. 2: The available data are retrieved from the DAQ buffer. 3: The new data are appended to what was retrieved previously. 4: Data exceeding the expected waveform size are trimmed (this is only required at the last cycle of the main loop). 5: Data gathered so far are sent to **`Graphing_center`** to be plotted. The inset close to the upper left corner shows the input terminals of the sub-VI.

3.2.5 The fast scan procedure

The maximum scanning speed of the SDL is about $9\,\mathrm{mm\,s^{-1}}$, which is insufficient to achieve the desired scanning rate of $1\,\mathrm{Hz}$ or more. Besides, it is generally not recommended to operate "worm gear" stages like the Zaber installed in our setup at their maximum speed for long periods of time. To achieve fast scanning, we employ stages operated via electromagnetic actuators, where changing the current in a coil alters a magnetic field, forcing the retro-reflector to move accordingly. The position can be evaluated from the current circulating in the coil, as the mirror oscillates between the extremes of the scan range.[10]

The motion during the scan cannot be at constant speed, because the sudden inversion at both ends of the scan would transfer a significant impulse to the mount, causing a quick deterioration of the delay line alignment (which requires at least a daily check): the simplest and safest solution is to drive the mirror in a sinusoidal oscillation.

Since the DAQ can only sample the signal at uniform time intervals, the corresponding delay values are now spaced unevenly and to perform a Fourier analysis the spacing needs to be regularized by interpolating at the desired delay interval $\mathrm{d}t$. This interpolation is in itself a filtering operation that cannot be avoided, but its impact on the data can be minimized by having the pulse close to the middle of the oscillation, where the spacing is close to uniform, and thus subject to minimal alterations. By sampling at the maximum rate allowed by our DAQ, $20\,\mathrm{kHz}$, while the FDL oscillates at $1\,\mathrm{Hz}$ over a range corresponding to $50\,\mathrm{ps}$, we obtain an average delay step of:

$$\mathrm{d}t \approx \frac{2 \times 50\,\mathrm{ps}}{20\,\mathrm{kHz}} = 5\,\mathrm{fs}. \tag{3.2}$$

The initial FDL model (shown at F.3.1a-[illegible]) was a MEsaPhotonics ODL:160804B, that is operated by directly applying voltages to dedicated pins on the control electronics; the actual position is encoded in a voltage level that can be read out from another pin. The original FDL was automatically positioned at the middle of its travel range (rest position) as soon as it was turned on, without the possibility to check for its actual position beforehand, resulting in abrupt start and stop of motion, with the same detrimental effects on alignment, although over a longer time. The practice of bringing the mirror to the rest position at the end of each scan proved to be insufficient, since it is not effective in case of power outage or computer crashes,

[10] The inertia of the mirror and the latency in its reaction to magnetic field changes can be neglected for frequencies below $10\,\mathrm{Hz}$.

which we experienced a few times, resulting in full swings at maximum speed on restart. In the end, we replaced the ODL:160804B with a ScanDelay USB, produced by APE (Angewandte Physik & Elektronik GmbH). Its mirror is mounted inside a spring-loaded suspender, rather than a rail, that naturally goes back to the rest position when the power goes off, regardless of the cause.

Additionally, the ScanDelay USB comes with its own controller, fully configurable via USB port, that provides the correct control voltages to drive the FDL in harmonic motion over a range nominally equivalent to a delay of $50\,\mathrm{ps}$ at an arbitrary frequency (up to $20\,\mathrm{Hz}$). The control box encodes the current position in a voltage level emitted via a BNC labelled **`Delay`**, which is verified using the DAQ. To ensure that the two devices are properly synchronized, the DAQ generates a sinusoidal signal that is sent to the control box input labelled **`Trigger in`**, where it is used as the common time base, thus avoiding relative drifts due to factory tolerances in the internal oscillators.

Once started, both the DAQ and FDL keep doing their respective jobs indefinitely and since they are independent pieces of equipment, we must ensure the proper association of each DAQ sample with its corresponding FDL position, also taking into account that the latter is scanning in both forward and backward directions. Rather than re-calculating the association for each batch of data, we perform an initial synchronization of the two processes such that the individual scans can be retrieved by simply splitting the raw sample array at fixed positions. This requires the use of an integer value N for the scanning frequency, so that the whole array contains $2N$ scans that are trivially split apart, with the caveat that every second sub-array needs to be reversed, since it was measured during the backwards swing of FDL.

Although the splitting is correct and stable (at least until the mirror inertia stays negligible), the scans taken in opposite directions will not have the same shape, because of the sliding window effect mentioned on page 44.

In any sweeping scan, the lock-in does not have time to flush samples associated with previous positions from its buffer. Since the lock-in is averaging data taken at least within the last integration time, a scan at speed v_{dl} would result in mixing data that belongs to a delay window of amplitude:

$$t_w = \frac{2t_{int}v_{dl}}{c}. \tag{3.3}$$

This windowing, when applied to a pulse, has the effect of lowering the peak value, since it can never be

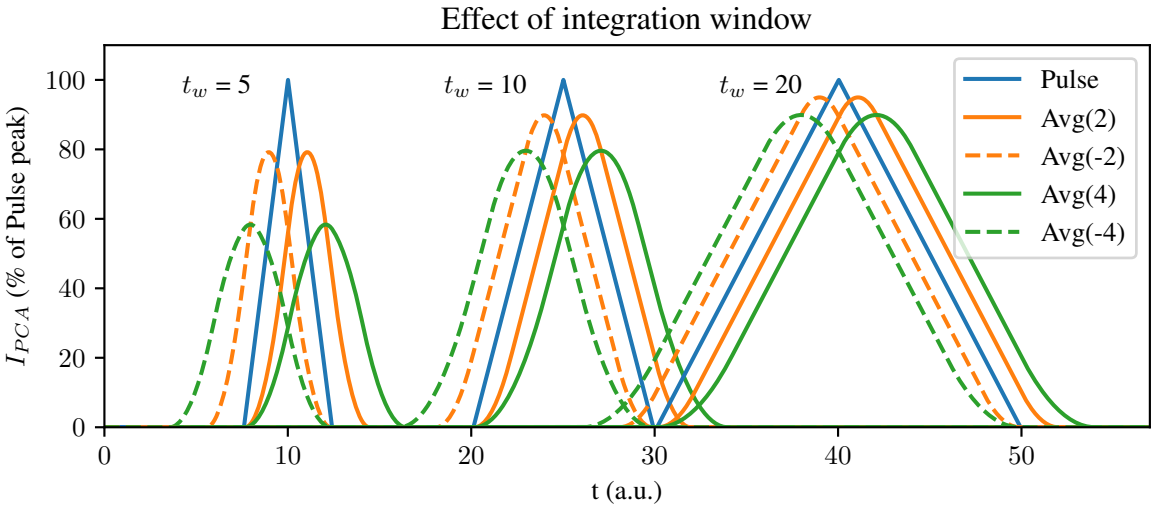

Figure 3.7: Illustration of the sliding window effect on example triangular pulses. To simulate the scan we took the average of the example pulses over a window starting at the measurement time and extending to the left (right) for forward (backward) sweeps, using window widths of 2 a.u. and 4 a.u. (-2 a.u. and -4 a.u.). All pulses had the same peak value and width of 5 a.u., 10 a.u. and 20 a.u. and the amplitude is in percent of the peak value. The time shift is correlated to the window width, but does not seem to be affected much by the slope of the peak. The amplitudes also correlate with the window width, but show anti correlation with the slope of the peak.

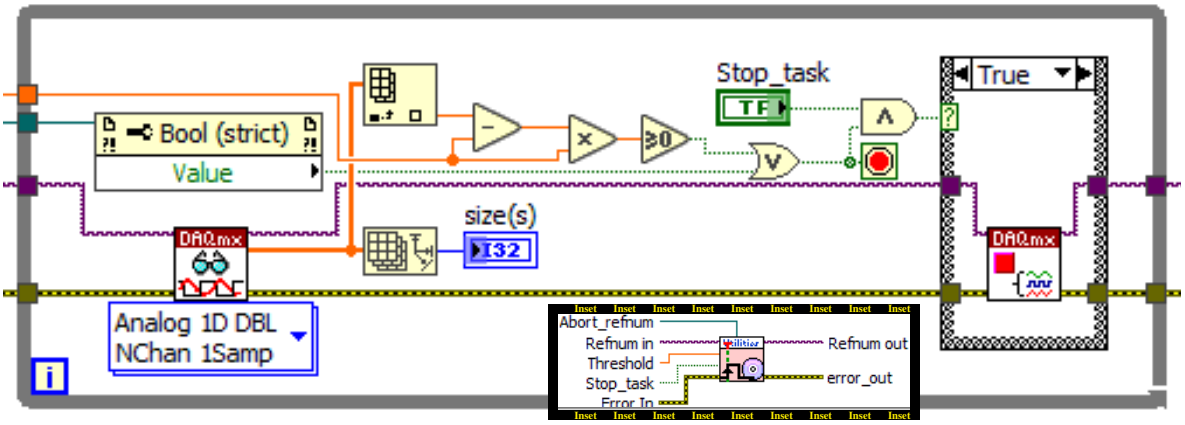

Figure 3.8: Diagram of the **`Trigger_Emulator`** sub-VI. The signal is read sample by sample and compared to the **`Threshold`**. When the condition is met, the sub-VI terminates, giving control back to the caller. The data acquisition task is stopped if the **`Stop_task (optional)`** contains the value True (default True, but we pass the value False). The inset in the lower part shows the input terminals of the sub-VI.

mixed with larger ones, but also causes the detected pulse to shift with respect to the true one. In fact, when the window lays completely outside the pulse, it makes little difference that the values come from different parts of the signal, because they are all random fluctuations of the PCA thermal noise. However, as the window approaches the slope of the pulse, the old values in the buffer cause the average to rise more slowly than the signal: this smooths-out small features (*i.e.* it filters higher frequencies) and makes the signal rise later. On the falling slope of the pulse, we have the opposite, with new (lower) values overwhelmed by higher ones from previous samplings, postponing the falling edge and therefore the pulse as a whole. In an oscillating scan, the role of rising and falling edge of the pulse for a forward and backward sweep are reversed with respect to each other, so that the shift will be positive (towards larger values of the delay) for a forward sweep, and negative (towards smaller delays) for a backward one. A simulation of the effect is shown in fig. 3.7 using simple triangular pulses of different slopes, for both sweep directions, and different window widths. The decrease of the peak value is much more pronounced with sharper pulses and larger windows (as one would expect), while the magnitude of the shift seems to depend only on the window width; this model, however, is only meant as an illustrative example and cannot substitute for direct observation. Since the sign of the shift depends on the sweep direction, the forward pulse shapes will not exactly match the backward ones and the two data sets should be treated differently if we want to use them together. The sub-VI in charge of splitting the one-second-long data arrays into individual scans offers the option to discard the backward scans to simplify data analysis during the initial phase of the project (proof of concept). Introducing appropriate treatment for the backward sweeps would double the effective scanning rate of the device.

a) Motion-DAQ synchronization

The synchronization (see fig. 3.8) is performed by measuring the 'Delay' signal from the ScanDelay USB and looking for the first sample such that its value satisfies $(V - Thr) \cdot V \geq 0$, where Thr is a threshold value chosen to be slightly smaller than the value for the maximum elongation. The extra multiplication by V makes the condition also suitable for use with negative thresholds, to synchronize with the minimum. When the condition is met, the sub-VI stops the DAQ task that measures the 'Delay' unless the control **`Stop_task (optional)`** is passed the value False and returns control to its caller, thus informing it that FDL is at the starting position for a forward scan. The threshold value passed as input to **`Trigger_Emulator`** is calibrated to give the caller

the time to start collecting data from the lock-in exactly at the start of the swing. This synchronization is stable because the DAQ and the ScanDelay USB share a common time base as just explained, however the time between the moment **Trigger_Emulator** ends and the start of data taking is subject to a small jitter caused by the scheduling of the Operating System (OS): while this is not a concern, because it happens in the region of the scan that contains no signal, it is crucial that all scans are correctly aligned, at least within the same measuring session (especially when performing an image scan), because a shift could be wrongly interpreted as a feature introduced by the sample. To avoid this issue, the fast scan functionality is split between two sub-VIs, one charged to initialize and perform the actual measurement continuously (**ShakeAndRead**), the other to pick the latest scans and send them to be plotted or saved to disk on-demand (**fast_scan_procedure**).

b) Continuous readout

The **ShakeAndRead** sub-VI takes as input the reference to a queue (**Raw_data_Queue**) that will be used to send data to other sub-VIs, as well as references to several external controls that allow its main loop to receive commands and configuration directly from the front panel of **THz_imaging_center**[11].

The scan configuration is contained in the control named **Parameters** (a TypeDef), in particular **ShakeAndRead** makes use of:

N to Average: the number of consecutive sweeps to average into one scan,

N to Save: the number of scans to perform in the next run,

Samp_rate: the acquisition rate the DAQ should use,[12]

Amplitude: the value in Volt corresponding to the maximum elongation of the line.[12]

Upon start, the main loop of **ShakeAndRead** enters the default `Idle` state, that is to wait for further instructions without starting the FDL. When the control referenced by **ShakerONOFF_ref** is set to True, *i*) the state machine transitions into the `Initialize` state, where the hardware and DAQ task configuration takes place, *ii*) then it transitions into the `Start` state, where the FDL is started, the maximum elongation is determined and **Trigger_Emulator** synchronizes the DAQ to the motion, *iii*) and finally it enters into the `LongAction` state.

[11] In the inset of fig. 3.9 the names of those terminals contain explicitly the word “controls”, “references” or the suffix “**_ref**”.

[12] This item is required by **ShakeAndRead**, but there is normally little reason to change it at all and could probably be hidden from the user in future versions.

The actual data taking is performed inside `LongAction` (see fig. 3.9) by reading one second worth of DAQ samples and selecting the part from the lock-in (labeled 'input') at the F.3.9-1 mark; the raw data are split into segments, each containing a raw scan, by the **shaker_pattern_folder** sub-VI at the F.3.9-2 mark[13]; finally each scan is inserted into the **write queue in** queue, that is configured to discard the previous scan when a new one is inserted, in order to avoid data pile-up when **fast_scan_procedure** is not running.

The main loop handles two further states: `Stop` for the suspension of the motion and data taking (*e.g.*: to change configurations) and `Quit` for the termination of the sub-VI.

c) Scan procedure

The gathering of data for the purpose of visualization and storage is handled by the **fast_scan_procedure** sub-VI. It receives as input *i*) the reference to the same **Raw_data_Queue** (page 50) that is being filled inside **Shake-AndRead**, *ii*) the reference to the same **Queue in** used in **Graphing_center** to receive the data to be plotted (page 40), and *iii*) the scan parameters from the front panel of **THz_imaging_center** (**Parameters**).

To help keep the diagram clean and simple, the loop that retrieves the data from **Raw_data_Queue** is implemented in a sub-VI visible at F.3.11-1 in fig. 3.10. This sub-VI called **fast_data_picker** requires an additional queue to communicate with the main loop of the sub-VI **fast_scan_procedure**, but it also handles the optional averaging of consecutive scans, governed by the **N to Average** value of **Parameters**, that is likely to become increasingly complex once in-depth treatment of the windowing effect discussed at section 3.2.5 is implemented.

In the main loop, upon successful extraction of an averaged scan from the auxiliary queue at 2, the data are interpolated at uniform intervals corresponding to the value **Delta_t (ps)** from **Parameters**; the non uniform delay values that correspond to the samples in the averaged scan are pre-computed by **fast_scan_procedure** during the initialization (not shown in fig. 3.10), by means of the **Amplitude**, **Scans_per_second** and **Samp_rate** values from **Parameters**. The interpolated scans are then transmitted to **Graphing_center** (at F.3.10-4) and, if required via the **Save** control, to the **OutputManager** sub-VI by mean of **write queue in** (at F.3.10-5), until the number of averaged scans (tracked by the sub-VIs

[13]The encapsulation of the procedure in a sub-VI facilitates its reuse elsewhere in the software, making it easy and safe to add extra checks and functionalities to the operation.

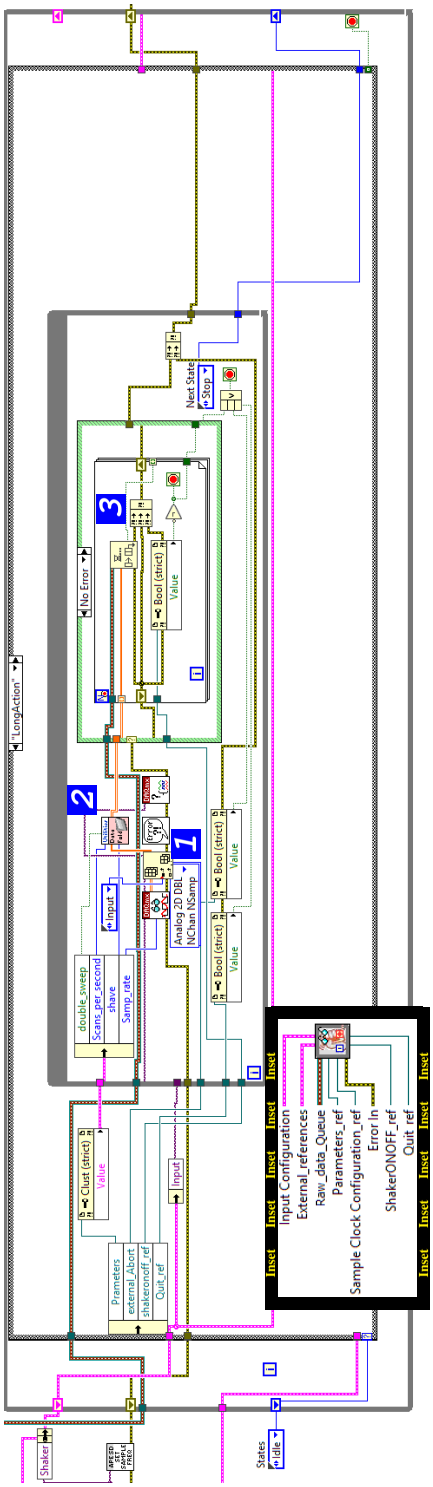

Figure 3.9: Display of the `LongAction` from the main loop of the **`ShakeAndRead`** sub-VI. The group of sub-VIs directly above the F.3.9-1 mark are responsible for the retrieval of raw samples from the Data Acquisition (DAQ) module in batches covering one second each, discarding the position information, since it can be deduced thanks to the synchronization performed during the `Start` state. The raw sample array is given to the helper sub-VI **`shaker_pattern_folder`** at marker F.3.9-2 to be split into individual scans, according to the oscillation frequency. The loop with the mark F.3.9-3 inserts all individual scans in the queue for transmission to other modules. The inset in the lower left part shows the input terminals of the sub-VI.

around the F.3.10-6 mark) reaches the value of **N to Save**.

By keeping the averaging and the interpolating loops separated from each other and from the DAQ reading loop in **ShakeAndRead**, as well as from the writing of data to disk performed in **OutputManager**, LABVIEW will assign the four phases of data acquisition to different processor cores and execute them in parallel whenever possible, speeding up the process. Before this asynchronous architecture was implemented, if any of the operations were to slow down due to latency in the OS, the DAQ would eventually fill up and cause a crash of the program, especially for long acquisitions. This kind of malfunction was observed sporadically, resulting in the loss of data and measurement time. However, with the adoption of the asynchronous scheme, the issue was no longer observed.

3.2.6 Image scanning

As the name of the **Image_scanner** sub-VI implies, its role is to handle the process that builds a raster image of the Sample Under Test (SUT), with each pixel holding at least one complete THZ scan and, therefore, the spectral fingerprint at that specific location, from which we can extract the temperature. This task is quite important because the methods used today for monitoring skin temperature during PTT, allow for imaging, but, as mentioned in chapter 1, are limited, as they either require contact or lack at least one among penetration depth and spatial resolution [11, 12, 15, 16], all issues that can be addressed using a THZ-based approach.

The **Image_scanner** module builds upon **slow_scanner** and **fast_scan_procedure**, which can deliver scans in slow and fast mode respectively, with different degrees of precision, so that it only has to provide the additional X-Y motion control and coordinate it with the THZ scanners and the **OutputManager**. The capability to use both modes at this stage was considered a desirable feature, since the system was primarily meant as a proof of concept and a research tool, rather than a fully optimized and automatic product. As a consequence, the interface of **Image_scanner** has to replicate most of the inputs required by **slow_scanner** (at F.3.3-6) and **fast_scan_procedure** (at F.3.3-5) as well as the references to **PlottingQueue**, **Raw_data_Queue** and **write queue in**.

The controls in the tab at F.3.3-4 are all specific to the **Image_scanner** sub-VI, in particular, the two

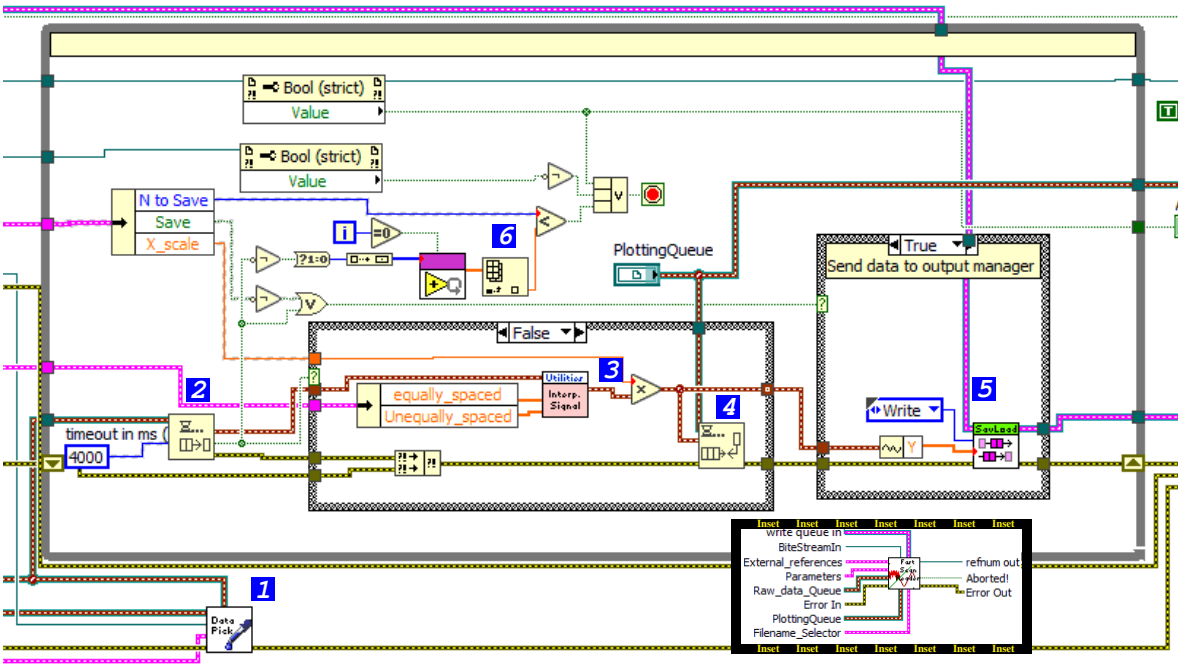

Figure 3.10: Detail of the diagram of the **fast_scan_procedure** sub-VI (the initialization part is not shown). 1: The **fast_data_picker** sub-VI is responsible for retrieving the individual scans produced by the **ShakeAndRead** sub-VI, for evaluating the average over groups of **N to Average** consecutive scans and for inserting it in an auxiliary queue, to be extracted in the main loop at 2. 3: The interpolation to make the scan **Delta_t (ps)**-spaced takes place after the average to save execution time. The values of the original inhomogeneous spacing are evaluated in the initialization part according to the scan parameters in the **Parameters** control. The interpolated scan is transmitted to **Graphing_center** (at 4) and to **OutputManager** (at 5). 6: A counter tracks how any scans were retrieved from the auxiliary queue and the main loop terminates when the count reaches **N to Save**. The inset close to the lower right corner shows the input terminals of the sub-VI.

controls labelled **Motor X** and **Motor Y** give full control on the motors, but are generated by the producer-provided drivers (using the serial and channel number from the controls immediately below them), rather than LABVIEW, which can use them via references that are passed to **Image_scanner** and the VIs in the utility library `thorlabs_wrapper`.

Above **Motor Y** we find the controls used to set the maximum speed and acceleration (**Max Velocity** and **Max Acc**) for both motors, two buttons that start and stop the image acquisition (**Start Image** and **Abort Image**), and two switches, one to select whether the slow or fast THZ scan should be used (**Use slow**, default False) and the other to enable the X-Y stage (**Init XY**, default False). Upon

initialization, the Thorlabs motors seek their home position, thus bringing a previously aligned SUT out of the THz beam. It is therefore better to only enable them when a raster scan is required and the position of the sample is noted down.

The parameters that characterize the raster scan are grouped inside a TypeDef cluster (**Image_settings**) that holds the values in mm for the dimensions of the area to be scanned (**Width** and **Height**), the pixel dimension, or step, in the two directions (**Xstep** and **Ystep**) and**Scans per pixel**, which determines how many times the THz scan at each pixel is performed. The remaining two controls of **Image_settings** are seldom used. The function of **Transpose** was to change the layout of the raster image for storage purposes, which is not necessary with the latest format for the image data (see section A.5), while the **Pixel delay** control inserts a wait time between the time a pixel is reached and the start of the THz scan, and it should always be set to 0 s unless there is a good reason to wait extra time.

The values contained in **Image_settings** are suitable to describe a raster scan, where each pixel on a grid is visited by scanning each line in sequence. Instead of using two nested loops to perform the scan one step at a time, we chose to prepare a list of the pixel positions and cycle through them all with one loop (see fig. 3.11). The pixels are generated inside a sub-VI called **Make_Pixel_sequence** (at F.3.11-1) allowing for a more compact diagram and the possibility to visit the pixels in any order just by changing the implementation of **Make_Pixel_sequence**.

Inside the main loop, the X-Y motors are instructed to move to each pixel position, waiting for the motion to stop at mark F.3.11-2, then a description of the pixel is sent to **OutputManager** (at F.3.11-3). After waiting the additional time from **Pixel delay** (at F.3.11-4), the THz scan takes place using **fast_scan_procedure** or **slow_scanner** (not shown in fig. 3.11), according to the value assumed by the **Use slow** control. Whichever sub-VI is used is also responsible for sending the scans to **OutputManager** via **write queue in**. The format of the resulting data file is illustrated in section A.5.

Presently, with default settings for speed, acceleration and oscillation frequency of the FDL, the acquisition of a pixel takes 1.3 s so an image of one thousand pixels can be completed in ~21 min 40 s. In analogy to the THz scan, it would be possible to speed up the process by measuring a whole scan line without stopping, but this would come at the cost of a more complex data analysis, because each of the THz scans (**Scans_per_second**) taken at each pixel would then contain information from different locations on the SUT. Therefore, it seemed better to

implement it after a solid analysis routine is established for the stepping case. Another possibility would be to exploit the flexibility in the order pixels are visited that **`Make_Pixel_sequence`** provides. At the moment, the pixels are simply ordered so that even and odd-numbered rows are scanned in opposing directions to save roughly $40\,\%$ of the scanning time, but in principle **`Make_Pixel_sequence`** could generate sequences of pixels that do not lie on a regular grid, opening the way to sparse and adaptive scanning strategies in future developments.

In this chapter, we gave a thorough description of the hardware and software components of the system we built in our laboratory with the intention of developing a proof of concept apparatus for the use of THz radiation as a probe for temperature in biological tissue, without sacrificing too much in terms of experimental flexibility, but accounting as much as possible for the foreseeable issues that could arise in connection with its actual use on patients. The next chapter will be dedicated to carrying-out a quantitative assessment of the system performance with respect to signal quality in different hardware/software setting configurations.

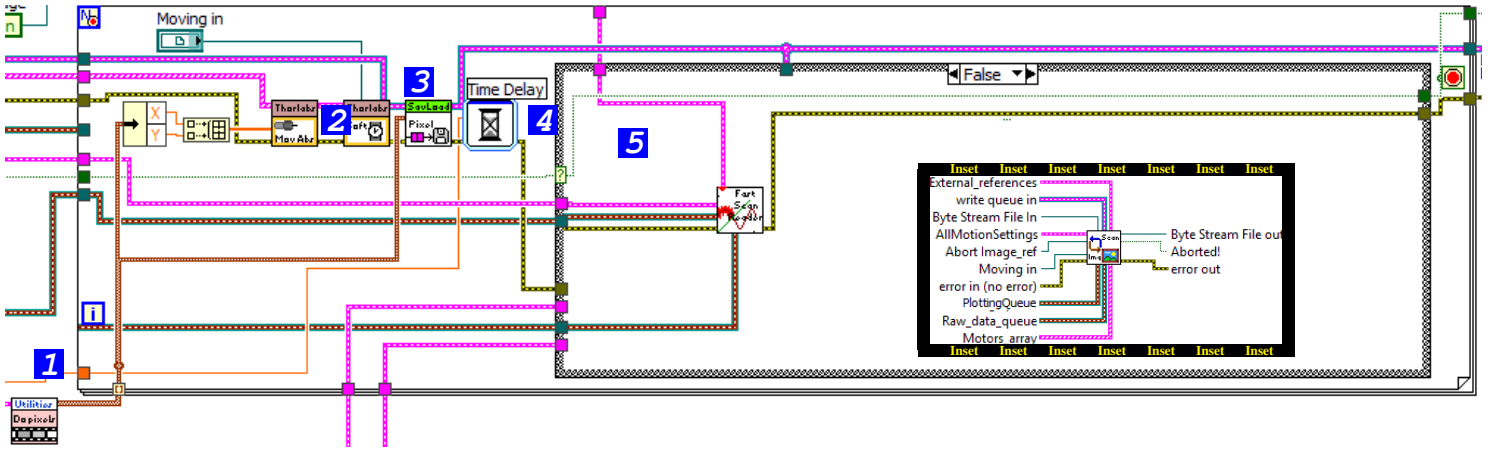

Figure 3.11: Detail of the diagram of the **`Image_scanner`** sub-VI (the initialization part is not shown). **1**: Sub-VI **`Make_Pixel_sequence`** generates a list of pixels (positions) to visit during the scan, based on the values in the **`Image_settings`** control received from the front panel of **`THz_imaging_center`** (see fig. 3.3 on page 39). Although the pixels currently form a simple grid with fixed **`Xstep`** and **`Ystep`** (visited following each row in alternate directions), they could be generated at arbitrary positions, in arbitrary order. **2**: Inside the main loop, the Thorlabs motors are instructed to move the X-Y stage on the position encoded in each pixel (VI on the left), waiting for the motion to be completed (VI on the right). **3**: Once in position, the pixel coordinates are recorded in a file in both motor and image reference system units (see A.4 for details). **4**: Before proceeding with the THz measurement, there is a pause of **`Pixel delay`** s (default 0 s). **5**: The THz scan is performed either using **`fast_scan_procedure`** (default) or **`slow_scanner`** (hidden in the figure), according to the boolean control **`Use slow`** on the front panel of **`THz_imaging_center`**. The scan is automatically saved to the disk right after the pixel specification and is repeated the number of times specified in the **`Scans per pixel`** control. The inset close to the lower right corner shows the input terminals of the sub-VI.

Chapter 4. Assessment of the setup

After having discussed the hardware and software components of the experimental system, their arrangement and intended interrelations, we used a quantitative approach and verified the quality of the THz measurements performed using our setup with different values of various configuration variables. For this assessment we initially used a mirror, rather than an actual sample, so that the expected result of the measurement would be the unperturbed THz pulse. This allowed us to appreciate any distortion that is caused by the current configuration.

4.1 Slow scan

In our setup, the SDL is primarily intended to perform a preliminary scan, used to *i*) find the exact position of the THz pulse, *ii*) adjust it so that it falls in the middle of the FDL and *iii*) calibrate the system by recording the shape of the pulse with an accuracy higher than what is possible with the FDL. This calibration, rather than being a cutting-edge measurement, only needs to be good enough to enable the correct operation of the system in its intended use as a real time monitor for PTT sessions.

Due to the fact that we use an SR865 as external lock-in and digitize its analog output via a DAQ board, the lock-in sensitivity setting also plays a role. The sensitivity (i_{sens}, in units of nA) that can be set via front panel buttons, does not change the way the instrument performs the measurement internally, but rather affects the way the measured signal is mapped onto this range. The analog output of the SR865 is limited in the range from $-10\,\mathrm{V}$ to $+10\,\mathrm{V}$ and the values that are actually measured are scaled so that the full-scale output of $10\,\mathrm{V}$ corresponds to the value of i_{sens} itself [119]. As a result, the value of i_{sens} should be chosen to make the peak value of the THz peak as close as possible to the full-scale of the output signal, effectively changing the proportionality factor between the DAQ-sampled voltage and the THz field.

To establish the sensitivity that best matches the unperturbed THz peak to the $10\,\mathrm{V}$ limit, we performed a measurement at very low speed $v_{dl} = 0.1\,\mathrm{mm\,s^{-1}}$, and extremely high integration time $t_{int} = 30\,\mathrm{ms}$. As mentioned in section 3.2.4, and further discussed at page 47, an important cause of inaccuracy when scanning in non-stop-mode is the windowing effect that mediates contributions from neighbouring parts of the pulse, where

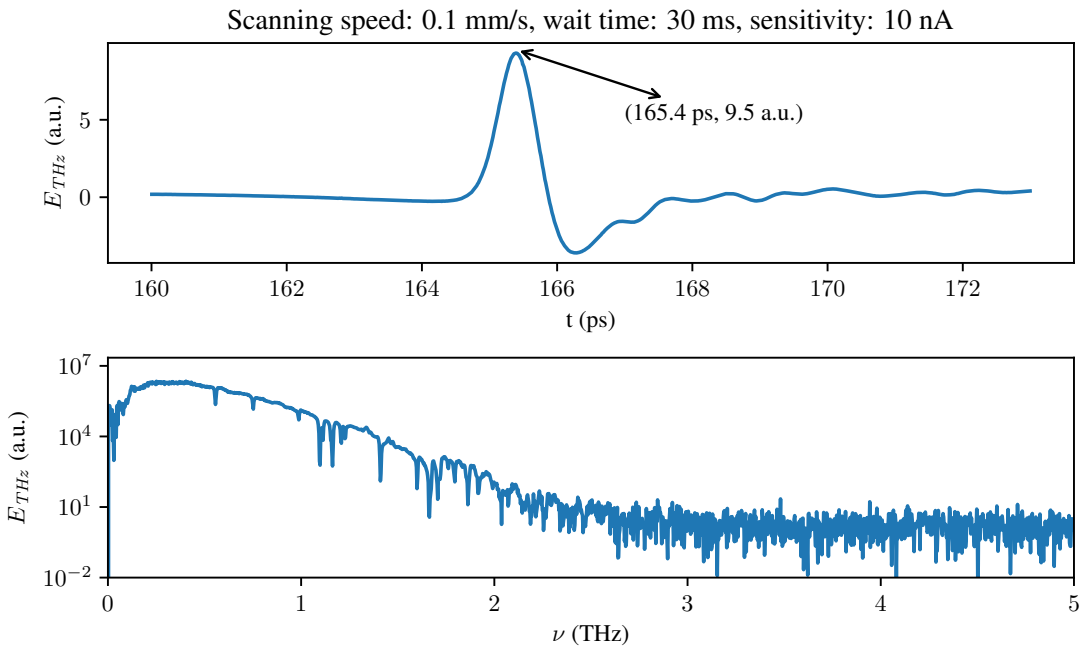

Figure 4.1: Reference measurement of the THz pulse circulating in our system. The arbitrary units of the upper y-axis are actually volts, since we are measuring the analog output of the lock-in: the factor used to convert the reading to the THz electric field is dependent on the sensitivity value. The lower panel shows the power spectrum of the signal: while it contains absorption lines from the non-purged atmosphere, it is otherwise well behaved up to 2 THz.

the severity of the deformation is determined by the values of the wait time (t_{int}) and scanning velocity (v_{dl}). These quantities determine the window width t_w: according to eq. (3.3), by selecting a lower v_{dl} the effect of a longer t_{int} is compensated and we can obtain a fairly low value for $t_w = 20\,\mathrm{fs}$, which allows precise and accurate measurement of the THz field even in non-stop mode. The measurement corresponding to the sensitivity that best matched the peak of the pulse and the full-scale of the output ($i_{sens} = 10\,\mathrm{nA}$) is shown in fig. 4.1: the spectrum in the lower panel is well behaved up to almost 2 THz, apart from the absorption lines due to a non-purged atmosphere.

Since this extremely slow measurement is very close to a step-by-step scan, the peak value is practically guaranteed to be lower at any other scanning speed, so we can use $10\,\mathrm{nA}$ as the standard value for lock-in sensitivity, thus ensuring that the same arbitrary unit is used to express all the following scans, making them

directly comparable across sessions.[1] To change i_{sens} every time a new scan is performed is also possible, gaining up to a factor of ten in resolution for smaller signals, but at this stage of development, the pay-off from the implementation of an adaptive sensitivity scheme seemed too small compared to the effort. To keep the duration of the scan below a reasonable time, we also decided that the minimum scanning speed should be $v_{dl}\ \ 1\,\mathrm{mm\,s^{-1}}$ when operating on a patient[2], thus leaving only t_{int} as the last parameter we can play with for optimization.

To estimate a recommendation for the integration time, we performed a series of measurements, sweeping the values of t_{int} allowed by the SR865 while keeping i_{sens} and v_{dl} at their standard values. In particular, we evaluated some properties of the measured pulses as indicators of the alteration induced by the changing parameter, namely: the signal offset, the pulse peak maximum value, position and Full Width at Half Maximum (FWHM), the Dark Noise (DN) and the Dynamic Range (DR) of the instrument. I will now briefly illustrate the operating definition of these quantities.

For the offset, I evaluated the fast Fourier transform of the signal, set to zero all components but the zero-frequency one, and did the anti-transformation:

$$F = \mathrm{fft}(Signal), \tag{4.1}$$

$$F(\lambda) = 0 + 0\mathrm{i},\ \text{for}\ \lambda \neq 0, \tag{4.2}$$

$$Off = \mathrm{ifft}(F). \tag{4.3}$$

The result of these operations is a vector with all elements equal to the offset; this method is simpler to implement than a direct approach.

The peak value (E^{peak}_{THz}) and position (t^{peak}) could be simply evaluated by looking for the highest value in the data vector, but this method is sensitive to unusually large fluctuations around the 'true' peak. Instead I selected a relatively narrow zone around the maximum value in the data and fitted that selection to a function. If the selection is narrow enough, a simple Gauss function can provide a good estimate for the position and amplitude of the main peak, and the fluctuation of one sample is not enough to move the result much.

Since the THz peak is not symmetric, the fit quickly becomes inadequate for points further away from the peak, so for the width parameter I decided not to use the gaussian standard deviation, but rather the FWHM, which

[1] It would be safe, during clinical trials, to change i_{sens} between patients, since all measures involve ratios, as stated on page 34

[2] This value is somewhat arbitrary and can be changed after the development of automated analysis routines.

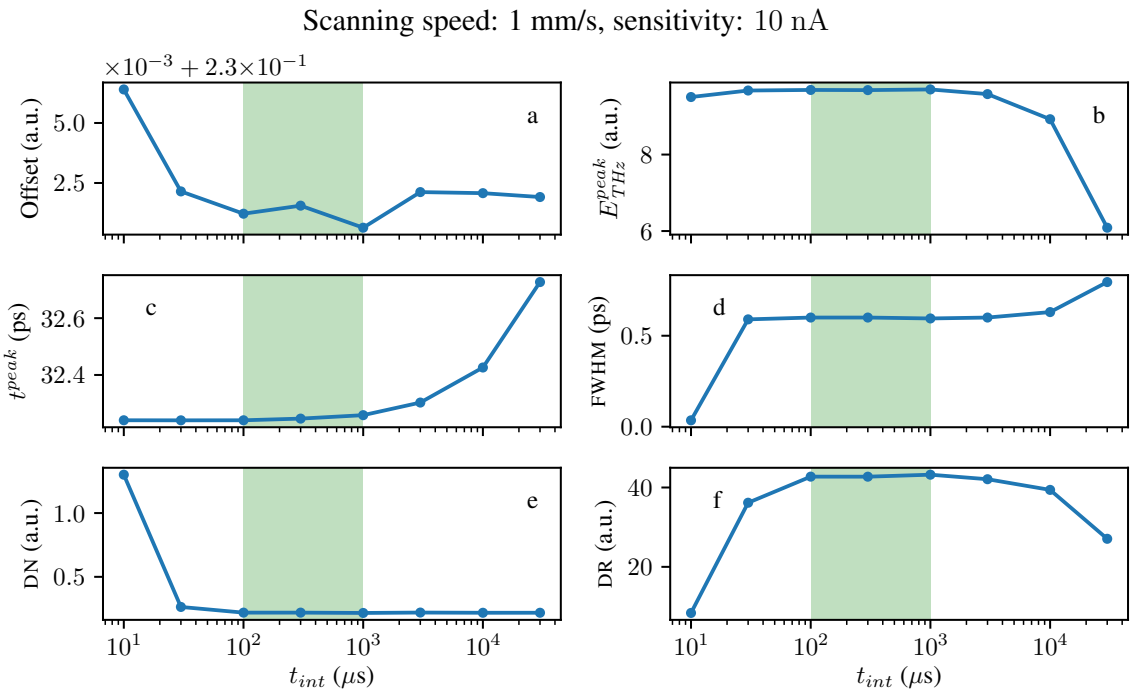

Figure 4.2: Plots of the signal offset ***a***, the pulse peak maximum value ***b***, position ***c*** and FWHM ***d***, the Dark Noise (DN) ***e*** and the Dynamic Range (DR) ***f*** for traces taken with t_{int} ranging from 10 µs to 10 000 µs. The green-shaded range is considered optimal for actual operation.

is straightforward to evaluate without peak shape approximations.

The last two quantities, are evaluated according to the definitions found in reference [120]. In particular, the DN is defined as the standard deviation of the samples taken outside of any signal. Operatively, I select the initial part of a scan, before the pulse starts, subtract the offset from all samples and then evaluate the Root Mean Square (RMS):

$$\mathrm{DN} = \sqrt{\frac{(Signal - Off)^2}{len(Signal)}}. \tag{4.4}$$

Since there is no signal, mixing samples from different delays is equivalent to measuring one fixed point multiple times. For the DR, we use instead the formula:

$$\mathrm{DR} = \frac{E^{peak}_{\mathrm{THz}}}{\mathrm{DN}}, \tag{4.5}$$

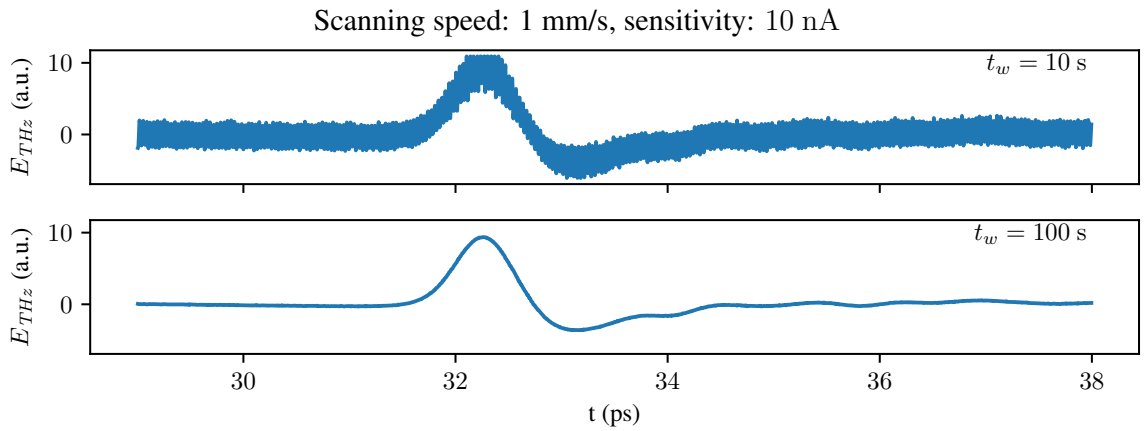

Figure 4.3: Comparison between scans performed with t_{int} equal to 10 µs and 100 µs. The smaller t_{int} is not able to filter-out the noise, to the point that the fluctuations at the signal peak fall out of scale (> 10 V, see top panel). The larger t_{int} used for the trace in the lower panel is the one selected by default in the software.

to relate the dark noise to the maximum detectable variation of the signal.

The results of the parametric sweep are shown in fig. 4.2. As expected, E^{peak}_{THz} and t^{peak} (panel ***b*** and ***c*** respectively) increase linearly[3] with t_{int}, while *Off* and FWHM (panel ***a*** and ***d*** respectively) tend to be relatively stable[4], with prominent exceptions towards low values of t_{int} that result in less effective filtering of the noise by the lock-in. In the case of $t_{int} = 10$ µs, the noise is so high that fluctuations overshoot the full-scale output of 10 V (see fig. 4.3 for a comparison with a trace taken with the default t_{int}). In fact, the poor DN (panel ***e***) at very low t_{int} is the cause of the corresponding reduction in DR (panel ***f***), while the smaller dip for high values of t_{int} is due to the increased reduction of E^{peak}_{THz} due to the windowing effect. Overall, values of t_{int} in the interval from 100 µs to 1000 µs (shaded in fig. 4.2) seem to provide the best results, therefore we adopted t_{int} = 100 µs as the default value.

4.2 Fast scan

To assess the performance of the fast scan procedure, we measured again the Terahertz reflected by the mirror, setting the integration time to the default value chosen in section 4.1 (t_{int} = 100 µs), with the same value of sensitivity used to perform the reference measurement displayed in fig. 4.1 (i_{sens} = 10 nA), but changing the

[3] Notice the logarithmic x scale.
[4] The variations in *Off* are smaller than 2 %, but the zoomed-in y-scale makes them appear larger.

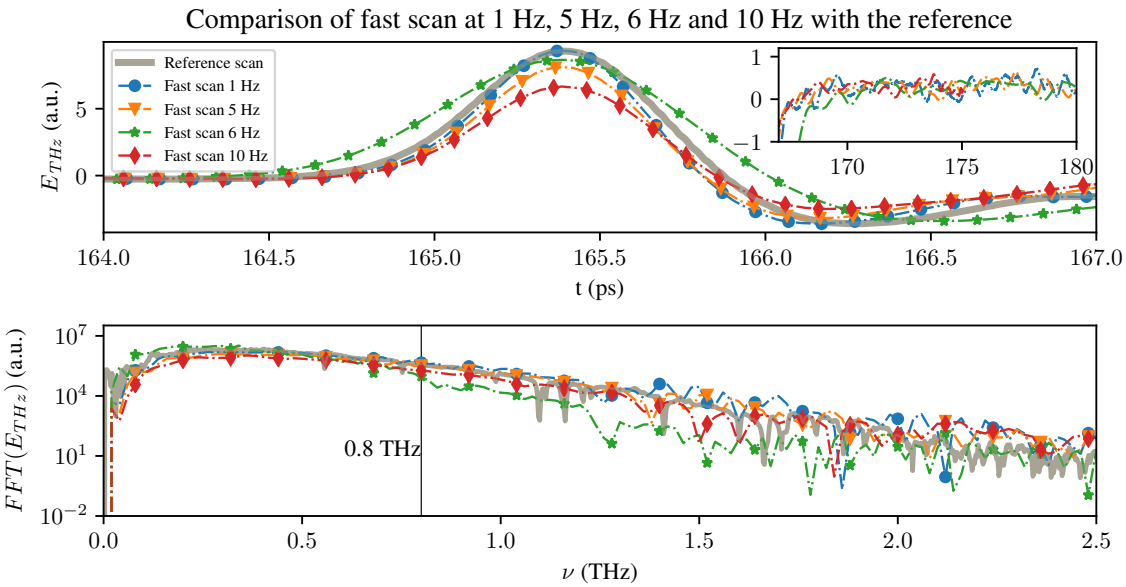

Figure 4.4: Comparison between the reference measurement from fig. 4.1 and fast scans. For the sake of clarity, only the scans performed at 1 Hz, 5 Hz, 6 Hz and 10 Hz are reported and the traces have been time-shifted to match the respective peak positions. The agreement deteriorates progressively with higher scan frequencies that are associated with longer t_w, up until 5 Hz. The measurements from 6 Hz to 9 Hz are visibly worse than expected after allowing for an increased t_w, with spurious features appearing just past 0.8 THz, but at 10 Hz the result falls-back in line with the trend of the lower scanning frequencies.

Scan Repetition Frequency (SRF) in the range from 1 Hz to 10 Hz.

The comparison between the resulting traces and the reference is displayed in fig. 4.4, but only for some of the more significant values of ν_{PRF} to avoid cluttering the plot (see legend for identification). Moreover, the traces have been realigned so that the respective main peak positions match each other. The deformation of the pulse produced by the higher speed of the FDL is not very pronounced at low SRF: for ν_{PRF} = 1 Hz. There is only a decrease in both pulse height and width, due to values from the first valley being still within $t_w$while measuring the main peak.

The difference grows steadily larger in the ringing region at the tail of the trace, see inset in fig. 4.4, where the oscillations are smaller and are mixed to a larger extent by the windowing. As expected, the discrepancy becomes progressively larger with increasing ν_{PRF}. However the general shape of the spectra seems to be reasonably preserved, at least for ν_{PRF} up to 5 Hz (the *regular group*). Starting at ν_{PRF} = 6 Hz (the *anomalous group*), the traces are deformed more than one would expect from the increased t_w and the

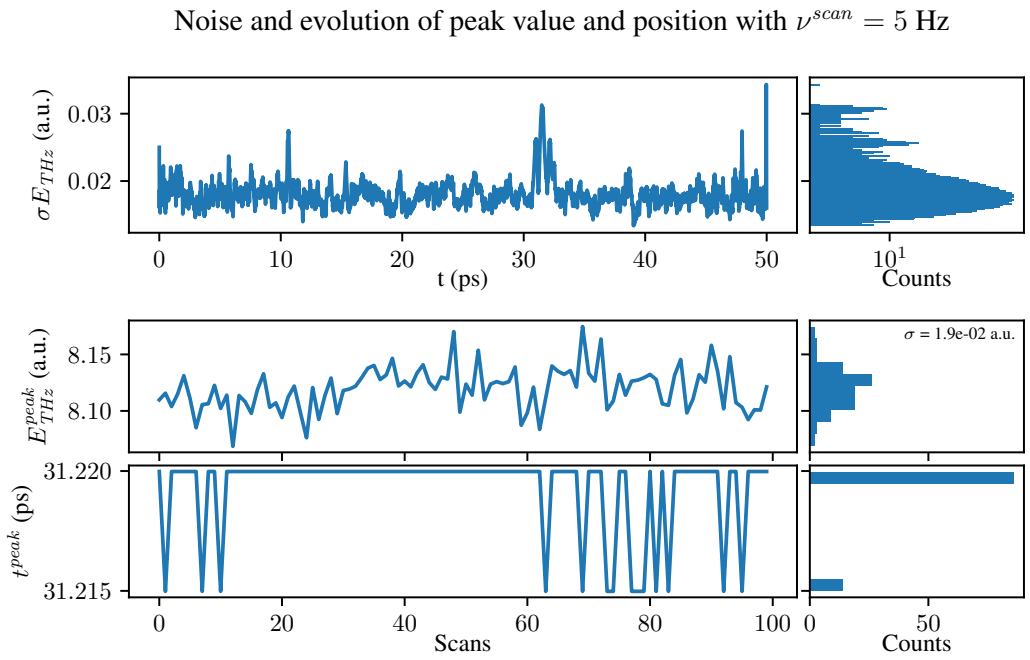

Figure 4.5: Stability of fast scan results for $\nu_{\text{PRF}} = 5$ Hz. Top: standard deviation of the traces (σE_{THz}) vs. time (delay). Middle: main peak eight (E^{peak}_{THz}) vs. scan number. Bottom: main peak time (t^{peak}) vs. scan number. On the right, histograms of the Y values relative to the plots on the left are shown (the top one has logarithmic scale).

spectrum gains spurious features above 0.8 THz.

This behaviour has been verified all the way to 19 Hz, the resonant frequency of the ScanDelay USB oscillating mirror, however, at $\nu_{\text{PRF}} = 10$ Hz the trace and spectrum revert to following the expected trend observed in the regular group.

A clue to the reason for this change of regime is obtained by studying the stability of the measurement between successive traces measured with the same settings we just used. For each value of ν_{PRF}, we measured 100 consecutive traces and plotted the standard deviation of each point in the trace (σE_{THz}) as a function of the delay (t) and the main peak eight and position (E^{peak}_{THz} and t^{peak} respectively) as a function of the scan number. The result for $\nu_{\text{PRF}} = 5$ Hz and 6 Hz are displayed in figs. 4.5 and 4.6 as representative of the behaviour in the regular and anomalous group, respectively.

In fig. 4.5 the σE_{THz} taken at 5 Hz SRF (in the top strip chart) correlates with the absolute value of the electric field (E_{THz}), peaking together with the signal. Only a few, isolated samplings in the regions before and after the

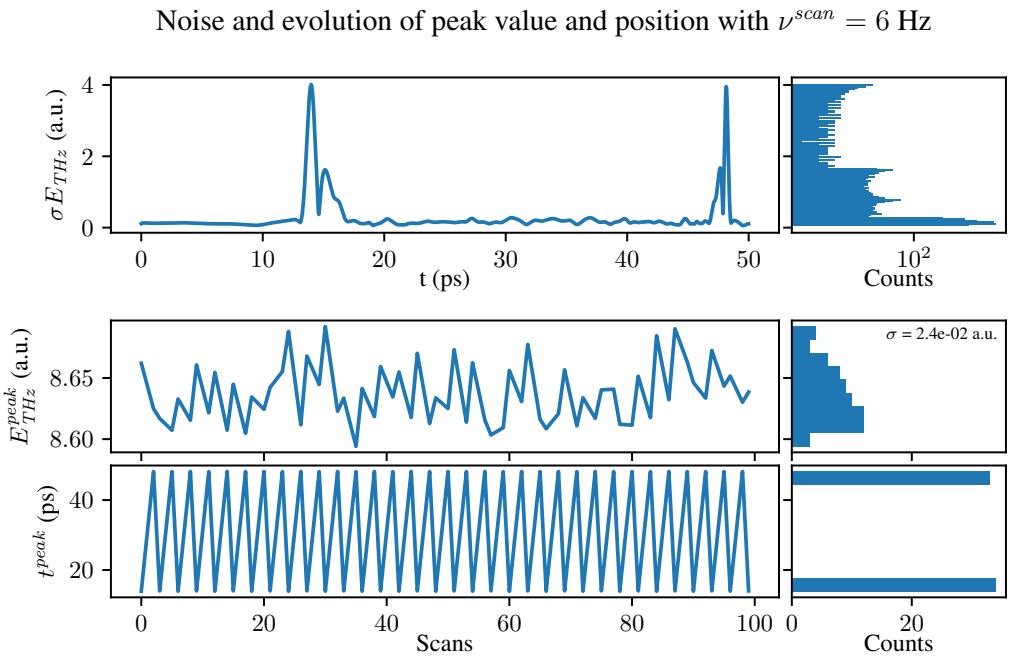

Figure 4.6: Stability of fast scan results for $\nu_{\text{PRF}} = 6$ Hz. Top: standard deviation of the traces (σE_{THz}) vs. time (delay). Middle: main peak eight (E^{peak}_{THz}) vs. scan number. Bottom: main peak time (t^{peak}) vs. scan number. On the right, histograms of the Y values relative to the plots on the left are shown (the top one has logarithmic scale).

THz signal feature a very large σE_{THz}, as attested by the top histogram (notice the logarithmic scale). The value of E^{peak}_{THz} in the middle strip chart is also very stable with a standard deviation $\sigma = 2.4 \times 10^{-2}$ a.u. that is among the highest along the trace and the sole cause of the oscillations of t^{peak} between two adjacent interpolation points.[5] The 6 Hz SRF results, displayed in fig. 4.6 are very different in that t^{peak} alternates between positions roughly 35 ps apart at every other scan, indicating problems in the synchronization between the DAQ and the FDL. The alternating position of the pulse results in artificially high σE_{THz}, however, the values outside of the pulses are compatible with those observed at other scanning frequencies, so data would be usable if not for this instability. In this configuration, the DAQ performs measurements at 20 kHz, and each one-second-long sequence is split into twelve segments. The even numbered segments are supposed to contain the backward sweeps and are discarded, but from the mirrored shapes shown in the σE_{THz} plot, we see that we alternatively get forward and backward sweeps, as if the mirror were oscillating at about half the configured frequency.A visual inspection of the mirror confirms that between 5 Hz

[5] Remember that an interpolation is necessary due to the sinusoidal motion of the FDL (see page 46).

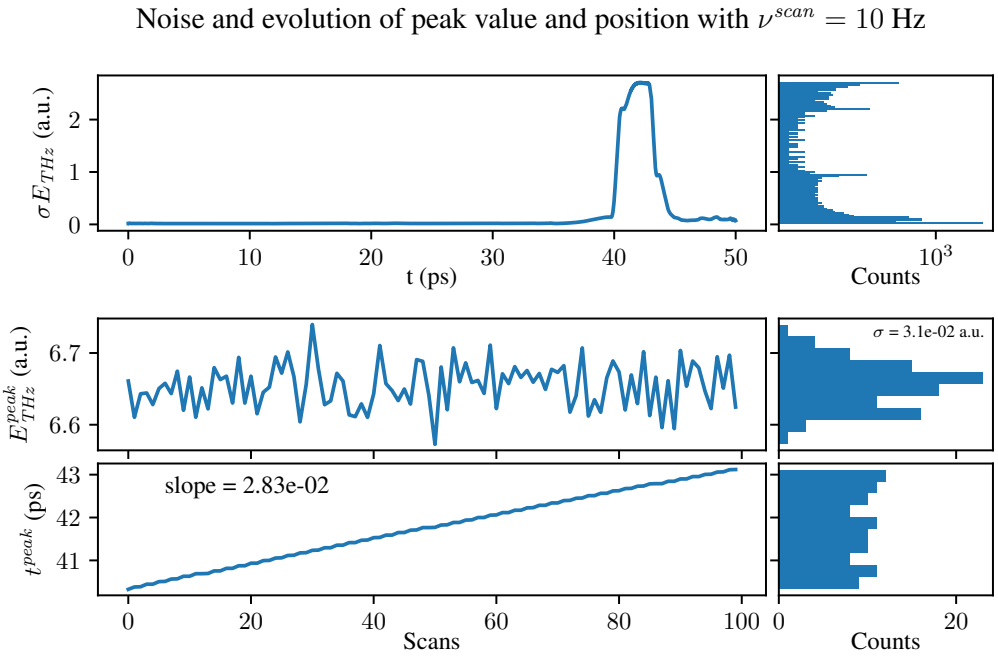

Figure 4.7: Stability of fast scan results for ν_{PRF} = 10 Hz. Top: standard deviation of the traces (σE_{THz}) vs. time (delay). Middle: main peak eight (E^{peak}_{THz}) vs. scan number. Bottom: main peak time (t^{peak}) vs. scan number. On the right, histograms of the Y values relative to the plots on the left are shown (the top one has logarithmic scale).

and 6 Hz the oscillation seems to slow down. One possible explanation is that, past 5 Hz, the mechanical damped oscillator, constituted by the mirror and its spring mount, does not follow the electromagnetic stimulus provided by the ScanDelay USB controller, as the manual itself acknowledge to be possible.[6] Another possibility is that a subtle bug in the sub-VI that configures the FDL causes a distortion in the reference clock sent to the ScanDelay USB controller, changing the effective scanning frequency. This hypothesis is under active investigation.

Either way, it is apparent that in the case of ν_{PRF} = 10 Hz the effective frequency is very close to the intended value, and the only distortion that is observed in fig. 4.7, is a drift of the pulse from one scan to the next at a constant rate of $2.83 \times 10^{-2} \frac{\text{ps}}{\text{scan}}$, causing the plateau in the σE_{THz} plot as the pulse moves over and out of zones with (almost) zero signal in successive scans, moving σE_{THz} away from the values found in the *regular group*.

Since the drift is constant, it would be possible to account for it in the software with negligible computational overhead, allowing for 10 Hz operation, however, the very presence of the drift points to a possible, slight

[6] The manual states that once the driving force is set, the mirror will follow it within the limitations of mechanical systems.

compression of the time scale that needs to be calibrated and taken into account during data analysis.

4.3 Imaging

To test the raster scan imaging function of the setup without an actual skin sample does not make much sense. We are interested in the ability to discern features and variations over time, which simply are not present when scanning a mirror. To make the assessment more compelling, we used a sample of pig ear skin, as it is acknowledged as a good clinical model for human skin, due to the similarity of the respective histological and physiological properties. [121]

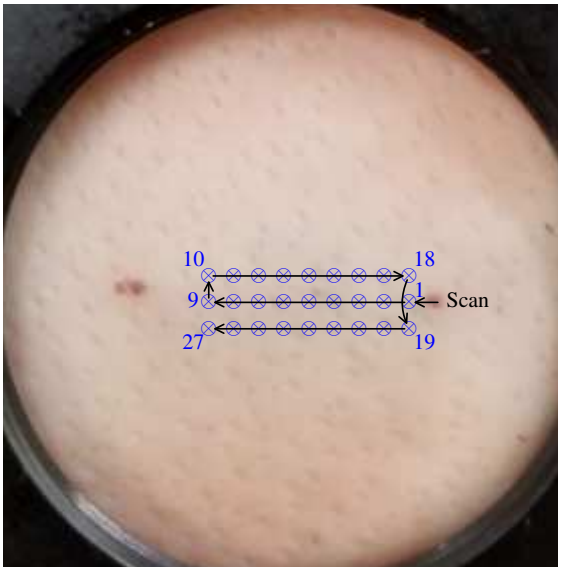

Figure 4.8: Mounted pig skin sample before irradiation. The ⊗ signs mark the 27 irradiation sites, the visiting order is indicated by the arrows and numbers.

The skin for the sample was procured at a local store and mounted on a holder that keeps it taut and suitable for installation in the THz branch of the setup, as shown in fig. 4.8. To induce temperature changes in the skin sample, we injected $50\,\mu\mathrm{l}$ of a $10\,\mathrm{nm}$ by $41\,\mathrm{nm}$ Gold Nanorods (GNR) suspension in its central part, that was then illuminated using a NIR laser diode of wavelength $786\,\mathrm{nm}$, set to an output power of $650\,\mathrm{mW}$. The light was delivered upon a series of spots[7] using the fiber coupled to the diode at the factory. The spots were arranged on three lines of nine points each, forming a $1\,\mathrm{mm}$ grid over the injected area (marked with ⊗ in fig. 4.8). The chosen wavelength has minimal interaction with skin, and caused no significant effect when irradiating the sample without GNR. The locations on the central line were the first to be illuminated, for $120\,\mathrm{s}$ each, followed by locations on the upper and lower lines for $60\,\mathrm{s}$ each (the visiting order is illustrated by the arrows in fig. 4.8).

Each irradiated spot was monitored for the whole time it was exposed to the laser, by using the setup in fast scan mode at $1\,\mathrm{Hz}$ PRF. The recorded maximum value of each measured THz trace is plotted in fig. 4.9 as a function of the trace number; this was done for the three scan lines separately. The discontinuities in the plots clearly identify

[7] No irradiation was performed while moving from one spot to the next.

the data belonging to each of the nine irradiation points. Further, we note that there is a common behaviour in the center and bottom line, in that the reflected THz signal first increases as the temperature rises, then either stabilizes or slightly increase owing to the diminishing hydration of the skin sample caused by the heat [122].

At the beginning of the middle scan line (first heating point), the recorded reflectivity is much larger, increases a little and then falls sharply to a value that is approximately maintained in the irradiation points that follow. It is likely that the sharp decrease is caused by the quick loss of water experienced as the temperature starts rising on the first point. Given the relatively long time of exposure ($120\,\mathrm{s}$), this dehydration affects the nearby areas, thus changing their response. Irregularities in the structure of the skin sample and inhomogeneity in the diffusion of the injected GNR account for additional variations.[8] The behaviour depicted in the top line is more complex than for the others: most irradiation points feature an initial sharp decrease in reflectivity, with a slight rise in the second half of the exposure. This could be interpreted similarly to the first irradiation point (fast decrease of hydration), but the behaviour is sufficiently different from the other two cases, that further investigation beyond the scope of this work would be required to shed full light on the results.

After completion of the simulated PTT session, the skin sample was visibly burned in the irradiated area, as shown in fig. 4.10, panel ***a***, and we inspected it again using the **`Image_scanner`** module covering the irradiated area with a 40×34 pixel grid, retrieving an image of dimensions $19.5\,\mathrm{mm} \times 16.5\,\mathrm{mm}$, where each pixel is a TDS scan of the THz pulse reflected from the skin sample. To identify the locations where the skin had been altered, and to what extent, we extracted from each trace a set of properties that describe the shape of the pulse (described in fig. 4.10, panel ***b***) and using each parameter we produced an image of the skin sample.

In detail, in each trace we identified the main peak and the valleys that immediately lead (front) and trail (tail) it, and for each we evaluated the value of the electric field (E^{peak}_{THz}, E^{front}_{THz}, E^{tail}_{THz}) and the corresponding width of the feature (Δt^{peak}, Δt^{front}, Δt^{tail}). The images are reported in fig. 4.11, where the first line of panels contains pulse-width-related images, and the second line contains the field-magnitude-related ones. From panel ***a*** to ***c*** it is shown that Δt^{front} is more sensitive to alterations than Δt^{peak}, which seems to have a lower contrast. Furthermore, Δt^{tail} is even more sensitive, to the point that it can hardly be used on its own, although it can still be used in combination with other information *e.g.*: panel ***d***, showing the ratio between Δt^{front} and Δt^{tail}, a

[8] The uniformity of the injection was on a 'best effort' basis, but, in living tissue, the GNR would be captured by nearby cancer cells.

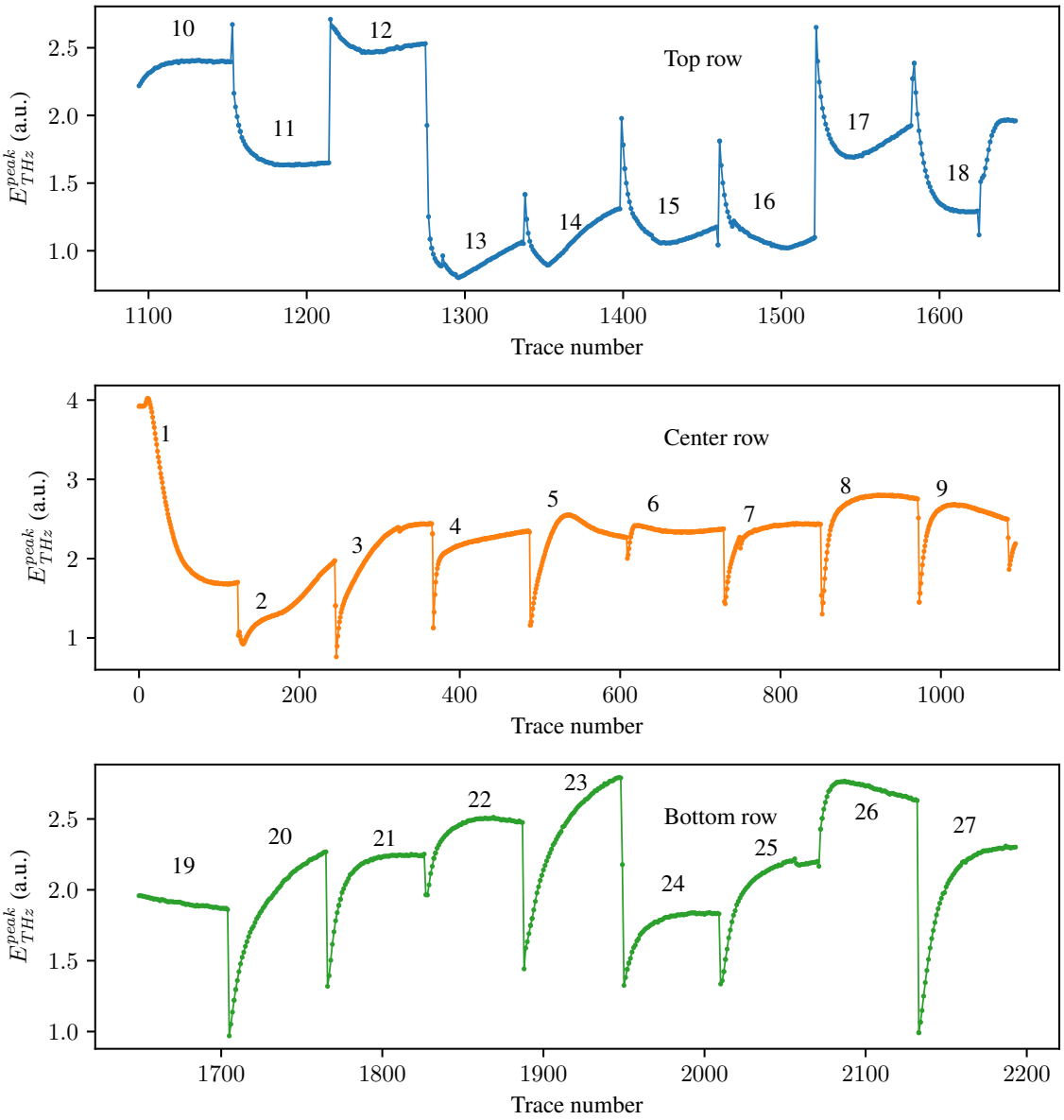

Figure 4.9: Peak value of the THz traces taken during irradiation along the path shown in fig. 4.8. The three plots correspond to irradiation on the top, center and bottom lines. Note that the center line was measured first, followed in order by the top and bottom ones, hence the trace numbers (one per second) in the abscissae axes are not consecutive for the three plots. The groups of traces related to each position are clearly identifiable (indicated by the position number in the figure) and show a good degree of consistency in their evolution through time. The difference observed at position one in the middle line can be explained by the onset of dehydration, while the irregularities of the points in the top line require further investigation — beyond the scope of this work.

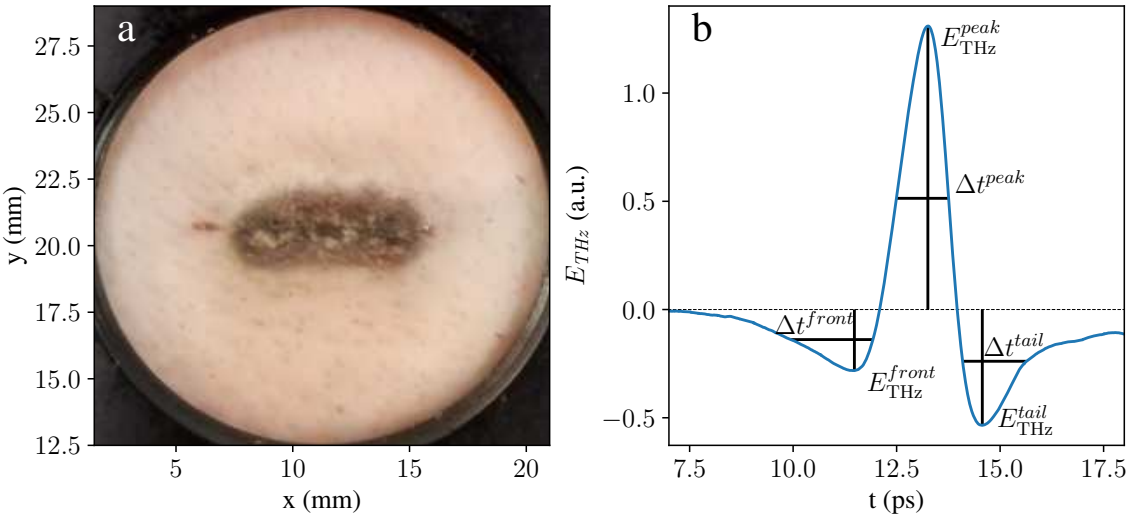

Figure 4.10: ***a*** photograph of the skin sample after irradiation following the pattern illustrated in fig. 4.8. ***b*** definitions of the shape parameters extracted from the traces measured by the **`Image_scanner`** sub-VI. These are: the amplitudes of the main peak (E^{peak}_{THz}), of the leading valley (E^{front}_{THz}) and of the first trailing valley (E^{tail}_{THz}), as well as their respective pulse width (Δt^{peak}, Δt^{front} and Δt^{tail}).

clear improvement with respect to the untreated Δt^{tail}. The small, brighter spots at the bottom right are outside the irradiated area and can be attributed to reflections on the sample holder.

The field magnitude data seem to follow the same general trend, with E^{front}_{THz} (panel ***e***) providing slightly more contrast than E^{peak}_{THz} (panel ***f***) and E^{tail}_{THz} (panel ***g***), consequently producing overall less recognizable images of the burn. However in this case, the information provided by the main peak and the leading valley seem to be a better complement to each other than the pulse-widths were among themselves. Finally, we remark that E^{tail}_{THz} is strikingly similar to the $\Delta t^{front}/\Delta t^{tail}$ ratio of panel ***d***.

In panel ***h*** is displayed the peak-to-peak value of the THz pulse, defined as:

$$E^{pk2pk}_{\mathrm{THz}} = E^{peak}_{\mathrm{THz}} - \min\left(E^{front}_{\mathrm{THz}}, E^{tail}_{\mathrm{THz}}\right). \tag{4.6}$$

The peak-to-peak value seems not to be very effective at improving the image with respect to the other field-related parameters; in fact it is only marginally more defined than the main peak value. All the images from panel ***e*** to ***h*** have a particularly luminous spot just to the right of the burned area that is too far from the holder for

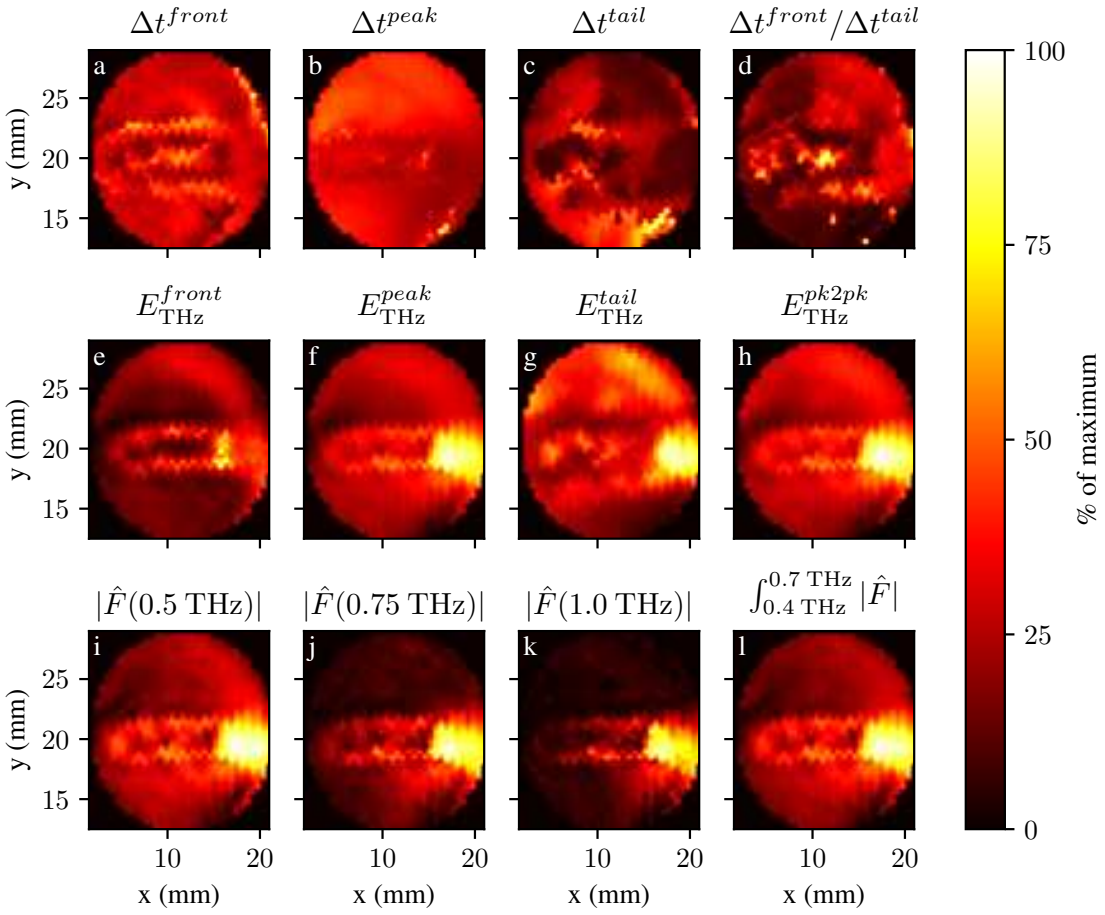

Figure 4.11: Imaging of the skin sample using various properties of the reflected THz pulses. ***a*** Width of the leading valley (Δt^{front}), ***b*** width of the main peak (Δt^{peak}), ***c*** width of the first trailing valley (Δt^{tail}), ***d*** ratio between the widths of the leading and trailing valley ($\Delta t^{front}/\Delta t^{tail}$), ***e*** magnitude of the field at the leading valley (E^{front}_{THz}), ***f*** magnitude of the field at the main peak (E^{peak}_{THz}), ***g*** magnitude of the field at the first trailing valley (E^{tail}_{THz}), ***h*** peak to peak value of the THz pulse (E^{pk2pk}_{THz}), ***i*** spectral density at $0.5\,\mathrm{THz}$, ***j*** spectral density at $0.75\,\mathrm{THz}$, ***k*** spectral density at $1\,\mathrm{THz}$, ***l*** integral of the spectral density from $0.4\,\mathrm{THz}$ to $0.7\,\mathrm{THz}$.

it to be the cause: it could be an irregularity of the particular skin sample or an artifact due to local misalignment.

Finally, since each pixel contains the full spectral information carried by the THz beam, we also evaluated the Flourier transform $\hat{F}$ of each trace (pixel) and compared its values at selected frequencies. The magnitudes of the transform at $\nu = 0.5\,\mathrm{THz}$, $0.75\,\mathrm{THz}$ and $1\,\mathrm{THz}$ are displayed in panel ***i***, ***j*** and ***k***, while panel ***l*** reports the integral of the magnitude from $0.4\,\mathrm{THz}$ to $0.7\,\mathrm{THz}$. All the images clearly identify the burned area with good

contrast, though the image becomes dimmer and harder to distinguish getting closer to $1\,\mathrm{THz}$, in comparison to the bright spot already observed in the panels from ***e*** to ***h***. The integrated spectrum from panel ***l*** is not much different from the value at $0.5\,\mathrm{THz}$, indicating that the spectral components at higher frequencies are not intense enough to influence the result of such a simple approach. To fully exploit the spectral capabilities of the setup, it is necessary to implement an appropriate weighting function. Furthermore, a method to mitigate the hot spot observed in both time and frequency domain via software is necessary. Even supposing it is just an artifact due to alignment or skin irregularity, to remove it by adjusting the setup would not be a viable solution during active clinical use, since repeating the scan would typically take about $20\,\mathrm{min}$ after each adjustment. Therefore, we suggest, as future development, the definition of a 'sample' preparation procedure that minimizes the insurgence of such artifacts and the implementation of an analysis algorithm capable of mitigating their impact, without requiring a repetition of the raster scan procedure.

On the other hand, even the images obtained with simple approaches seem capable of identifying alterations of the skin due to the heating process, not only in the directly irradiated area, but also in the immediate vicinity. Indeed, this is evident from comparing the results of fig. 4.11 to the photograph of the burned skin sample in fig. 4.10.

Chapter 5. Conclusion and future development

Cancer is rising to prominence among the causes of death in industrialized countries, such as Canada. While this prominence is in large part due to the increasing expected lifespan as new, improved cures for other diseases are found, the economical, social and psychological costs associated with cancer and its treatment are very high and continue increasing. To date, an important part of cancer therapeutic techniques stems from physics, rather than pharmacology, *e.g.*: radiotherapy, Photodynamic Therapy and Photothermal Therapy (PTT). The latter, of special interest for skin cancers, exploits plasmonic excitation of nanoparticles via an IR laser to selectively deliver heat in the cancerous tissue and it would benefit from a technology capable of monitoring the temperature reached by the treated area, to assess the efficacy of the process and limit the damage to nearby healthy cells.

In this work we developed the prototype of an optical setup that uses THz radiation as the probe to measure, in real time, the temperature and hydration in the skin of a patient undergoing PTT treatment. Our setup is intended to be used concurrently with PTT as a contactless monitor of the state of the treated skin and as an *a posteriori* diagnostic tool to assess the damage delivered to the tumor. Since the ultimate goal is to see this machine used on actual patients, our primary focus in developing our proof-of-concept was to balance the accuracy of the measurement with the speed of the whole procedure. This is paramount to reduce patient discomfort to a minimum and make the whole treatment session as time-effective as possible.

The setup employs two delay lines operating at different speeds. The fast delay line (FDL) is the one intended to perform scans on patients during PTT sessions and to take diagnostic raster images of the treated area afterwards. It is capable of taking up to ten complete THz traces per second using the forward and backward swing of the $5\,\mathrm{Hz}$ retro-reflector oscillation (bidirectional mode). However, in order to obtain fully comparable results, the odd (forward) and even (backward) numbered swings should be subjected to different processing, since moving in opposite directions causes different distortions on the measured trace. At the time of writing, we just implemented an option to discard backwards scans (unidirectional mode) to ease data analysis, at least in the initial stage of the project. In principle, the FDL can reach even higher scanning frequencies, limited by the mechanical oscillation resonance of $19\,\mathrm{Hz}$, rather than by the noise level at higher PRFs, but there is an issue with the stability of the retro-reflector oscillations, which currently prevents this from happening for oscillations past $5\,\mathrm{Hz}$. Indeed,

the instability turns to a regular variation over time when the retro-reflector oscillates at $10\,\mathrm{Hz}$. This could be exploited to apply a software correction to the data and operate at $20\,\mathrm{Hz}$ ($10\,\mathrm{Hz}$) in bidirectional (unidirectional) mode. However, understanding and possibly removing the instability altogether would be preferable.

We also paid special attention to the software used to drive the setup, *i*) making it as modular as possible, so that future improvements would be easier to implement, and *ii*) 'hiding' in secondary UI panels the more advanced controls that could be useful to us during our research activities, but would be unnecessary to a clinical operator, more trained in medicine than in THz physics. The software was initially assembled from samples provided by the producers of the hardware parts, but it was extensively refactored to meet the goals of modularity and simplicity of use stated above. This effort also enabled us to identify several bottlenecks in the original implementation, thus speeding the whole data acquisition by a factor of at least three and removing instabilities that caused software crashes during long acquisitions.

Tests performed on porcine skin models subjected to PTT treatment confirmed that our setup is capable of detecting, in real time, the changes the model undergoes during the procedure, although the relationship between reflected THz light and temperature turned out to be more complex than expected, due to the concurrent change in hydration, that induces changes of the opposite sign. On the other hand, the raster scan imaging of the treated area has demonstrated to be sensitive to the damage caused to adjacent cells by the local temperature increase in the zone containing GNRs.

It is worth repeating here, that the wavelength ($786\,\mathrm{nm}$) and power level ($650\,\mathrm{mW}$) of the employed heating laser, would not cause the observed effects on skin without the injection of the GNR and that *in vivo*, the damage would be delivered selectively to the GNR-hoarding cancerous cells (as mentioned on page 8). When both monitoring of the temperature and assessment of the damage in real time will be fully implemented, it should be possible to determine automatically when to stop delivering the IR excitation on the GNR. As a result, the technique constitutes a promising diagnostic tool to monitor and drive a PTT session, as well as to assess its success afterwards.

The system developed in this work constitutes a solid foundation for further research in the field of skin cancer treatment. It has shown not only that it is capable of performing continuous monitoring of the skin being treated with PTT, but also that it offers the flexibility required by a research tool to fully understand the interaction of Terahertz with dermal tissue. Furthermore, it is amenable to improvements, both in the hardware and software departments, thanks to its modular design.

Among the most important goals for future development of the analysis algorithm, the ability to treat adequately both forward and backward scans and the lifting of the restriction to 5 Hz of retro-reflector oscillation frequency are particularly important. The achievement of these goals would effectively quadruple the data acquisition rate and open up further optimizations of the raster scan procedure. For instance, each scan line could be measured without stopping at the position of every pixel, resulting in a substantial speed-up. Another interesting possibility would be to replace the termination of the two branches in the free-space optical path with fiber optics, so that the two PCAs could be easily placed close to the sample (patient) instead of the other way around, as is currently the case.

On the software side, a significant improvement would be to implement the data analysis algorithm in a sub-VI that could feed information back to the **`fast_scan_procedure`** and **`Image_scanner`** modules, thus allowing them to perform the imaging over an adaptive, sparse set of points, rather than the current predetermined raster grid.

Ultimately, to bring this technology into fruition as an effective tool for the treatment of cancer by the healthcare system, it will be paramount that we fully understand the relationship between the information gathered from the various features of the reflected THz light and the state of the observed skin, so that they can be combined into one or more optimized estimators, capable to assess the efficacy and thus monitor the progress of the treatment in real time.

Appendix A. Format of saved data

The `save_load_data` library implements VIs that can be used to write arrays and records to a file in a consistent format and read them back for use into the program at a later time. The data are stored as plain text to allow easy inspection of the values during development. However, the sub-VIs could be changed to output a binary format without affecting any calling VI structure or interface. A data file is organized in blocks, each containing data related to each other. In the following, we will use conventional markings for ⟨**Mandatory elements**⟩ and **[Optional elements]**. A → at the start of a line will denote continuation of the previous line and ellipses (...) will denote repetition of the previous element.

A.1 Generic block

Each block is composed by a 'Descriptor', followed by an optional line of 'Field specifications', the data itself and an optional block 'Termination mark' according to the following specification:

Block:

⟨**Descriptor**⟩

[Field Specifications]

⟨**Data**⟩

[Termination mark]

A data file can contain any number of blocks, although in our use case only one is usually present.

⟨**Descriptor**⟩: # [⟨**Kind**⟩:⟨**Label**⟩] ⟨**Numrows**⟩ ⟨**Orientation**⟩ ⟨**[no] Fields**⟩ ⟨**[no] Units**⟩ **[comment]**

1. The descriptor is present to document the type of measurement, its layout and size, right inside the file, so that it can always be loaded correctly at any future time. Since a file with only one block can be read using standard tools, the Descriptor begins with a character that marks it as a comment, so that the used tool can easily ignore it: by default it is the hash sign (#), but it can be configured to match different tools.

2. The ⟨**Kind**⟩ element contains a conventional name that specifies the type of block (multiple arrays, records etc.) contained in the block, the ⟨**Label**⟩ element can be used to specify the type of measurement or a unique identifier. Numbers, punctuation, white space and special characters are not allowed in both elements.
3. ⟨**Numrows**⟩ is an integer number corresponding to the number of lines occupied by the actual ⟨**Data**⟩: if the number is negative, then its correct value was not known at the time the descriptor was written and the ⟨**Data**⟩ must be read line by line until the **[Termination mark]** is found or the end of the file is reached.
4. ⟨**Orientation**⟩ determines whether data have to be arranged in rows or columns: it is a single character, with any of (H, h, R, r) standing for horizontal or row layout, and any of (V, v, C, c) standing for vertical or column layout. Only the characters listed in this description are allowed.
5. The ⟨**[no] Fields**⟩ and ⟨**[no] Units**⟩ elements are mandatory and the absence or presence of their optional part (**[no]**) determines whether the **[Field Specifications]** should contain the field name and/or measurement unit specification, respectively (this format was chosen to make it more readable to a human operator). If neither field names nor units are required, the **[Field Specifications]** line is omitted; it is an error to require the units without requiring the field names too.
6. Anything following the ⟨**[no] Units**⟩ element is considered a **[comment]** and can be ignored.

[Field Specifications]: # ⟨**Field Name [(unit)]**⟩**[, Field Name [(unit)]]** . . .

1. If present, the **[Field Specifications]** must start with the same comment marker used in the ⟨**Descriptor**⟩, followed by one **Field Name [(unit)]** specification for each field in the following data, separated by a comma: notice that the optional unit is in parentheses.
2. At least one specification is mandatory, otherwise the line could be omitted altogether.

⟨**Data**⟩: ⟨⟨**Number**⟩**[, Number] . . .**⟩

. . .

1. The ⟨**Data**⟩ section is composed of at least one row of numbers separated by commas: at least one number must be present in each row.
2. If the descriptor element ⟨**Numrows**⟩ is negative, the number of rows is unspecified and they must be read one by one until the **[Termination mark]** is found or the end of the file is reached, if ⟨**Numrows**⟩ is positive, the number of rows must match it.

3. If the ⟨**Orientation**⟩ is one of (H, h, R, r), the data are arranged horizontally and each row corresponds to a field; conversely, if the ⟨**Orientation**⟩ is one of (V, v, C, c), the data are arranged vertically and each column of data corresponds to a field.
4. When the field names are given in the **[Field Specifications]**, and unless different provisions are made for a specific ⟨**Kind**⟩, the number of fields should match either *i*) the number of rows, if ⟨**Orientation**⟩ is one of (H, h, R, r), or *ii*) the number of columns, if ⟨**Orientation**⟩ is one of (V, v, C, c).
5. Each specific ⟨**Kind**⟩ is free to change provision 4, so that rows/columns can be combined according to some pattern as well as be followed, interleaved or replaced with nested blocks: in such cases, the grouping patterns and the allowed nested blocks as well as their meaning and use, have to be specified in detail.

[Termination mark]: [EndBlock]

This literal string is used to mark the end of a block: it is optional if the block is the last in the file or if the number of rows in the block is known and declared in the ⟨**Descriptor**⟩.

A.2 Scan data block

The most common measurement done with the setup is a THz pulse scan, that contains two fields, the time delay due to the current position on the delay line and the value sampled at that position from the signal.

DataXYn:

[⟨**DataXYn**⟩:⟨**Label**⟩] ⟨**Numrows**⟩ ⟨**Orientation**⟩ ⟨**[no] Fields**⟩ ⟨**[no] Units**⟩ **[comment]**
[# ⟨Independent Variable [(unit)]⟩[, Dependent Variable [(unit)]]]
⟨⟨**Number**⟩**[, Number] . . .**⟩
⟨⟨**Number**⟩**[, Number] . . .**⟩
. . .
[Termination mark]

The block used to store this type of data follows the specification of a generic block with the following additional provisions:

1. The ⟨**Kind**⟩ is required to be **DataXYn**.
2. The ⟨**Data**⟩ is required to have at least two rows/columns.
3. The first row/column represents the independent variable while the second represents the corresponding measurements (*e.g.*: time and electric field in the case of a THz pulse scan).
4. If more than two rows/columns are present, the third and subsequent ones are repetitions of the measurement at the same values of the independent variable and inherit the second row/column field name and unit.
5. It is recommended to specify both field names and units with the **[Field Specifications]**; however, only two fields need to be specified, since the remaining ones are implicitly the same as the second.

A.3 Record block

A record block is designed as a container of named fields and/or nested blocks, such as custom data structures or UI fields.

Record:

 # [⟨Record⟩:⟨Label⟩] ⟨1⟩ ⟨H⟩ ⟨Fields⟩ ⟨[no] Units⟩ [comment]
[# ⟨Independent Variable [(unit)]⟩[, Dependent Variable [(unit)]]]
⟨⟨Number⟩[, Number] …⟩
[Block]
[Block]
…
[Termination mark]

It follows the specification of the generic block with the following additional provisions:

1. The ⟨**Kind**⟩ is required to be **Record**.
2. The ⟨**Label**⟩ can have any value respecting the general limitations: specific values of this field can be given special meaning and add provisions of their own to the format of the **Record**.
3. The ⟨**Data**⟩ is required to have exactly one row: in addition, any number of nested blocks can be present if the specification for a sub-type of Record allows it.

4. The ⟨**Orientation**⟩ is always horizontal (H, h, R, r).
5. The ⟨**Fields**⟩ element is mandatory, since to use a record only makes sense when the names are important.
6. It is recommended to specify both field names and units with the **[Field Specifications]**; however, units remain optional.
7. After ⟨**Data**⟩ there may be any number of nested blocks, depending on provisions associated with a specific value of ⟨**Label**⟩: if they are present, the **[Termination mark]** of the container record becomes mandatory.

A.4 Pixel block

A pixel block is a specialized record block, describing a pixel of a raster scan performed with the setup.

Pixel:

[⟨**Record**⟩:⟨**Pixel**⟩] ⟨**1**⟩ ⟨**H**⟩ ⟨**Fields**⟩ ⟨**[no] Units**⟩ **[comment]**

⟨**# ⟨row[(unit)],⟩ ⟨col[(unit)],⟩ ⟨X[(unit)],⟩ ⟨Y[(unit)]⟩**⟩

⟨⟨**Number,**⟩ ⟨**Number,**⟩ ⟨**Number,**⟩ ⟨**Number**⟩⟩

⟨**DataXYn**⟩

⟨**Termination mark**⟩

It follows the record block specification with the following provisions:

1. The ⟨**Label**⟩ is required to be **Pixel**.
2. The **[Field Specifications]** are fixed to the values:
   - **row**, the row number of the pixel in the raster scan.
   - **col**, the column number of the pixel in the raster scan.
   - **X**, the abscissa of the pixel in motor coordinates.
   - **Y**, the ordinate of the pixel in motor coordinates.
3. The **Pixel** contains one nested **DataXYn** block holding as many scans as selected from the UI prior to the scanning.

A.5 Image block

An image block is a specialized **Record** that holds all the pixels of a raster scan image and all the information necessary to its reconstruction.

ImageSettings:

[⟨**Record**⟩:⟨**ImageSettings**⟩] ⟨**1**⟩ ⟨**H**⟩ ⟨**Fields**⟩ ⟨**[no] Units**⟩ **[comment]**

⟨**#** ⟨**Height[(unit)],**⟩ ⟨**Width (mm)[(unit)],**⟩ ⟨**Xstart[(unit)],**⟩ ⟨**Ystart[(unit)],**⟩ ⟨**XStep[(unit)],**⟩

→ ⟨**YStep[(unit)],**⟩ ⟨**Scans per pixel[(unit)],**⟩ ⟨**Pixel delay[(unit)],**⟩ ⟨**Transpose[(unit)]**⟩⟩

⟨⟨**Number,**⟩ ⟨**Number,**⟩ ⟨**Number,**⟩ ⟨**Number,**⟩ ⟨**Number,**⟩ ⟨**Number,**⟩ ⟨**Number,**⟩ ⟨**Number,**⟩

→ ⟨**boolean**⟩⟩

⟨**Pixel**⟩

[Pixel]

[Pixel]

...

⟨**Termination mark**⟩

It follows the record block specification with the following provisions:

- The ⟨**Label**⟩ is required to be **ImageSettings**. As an exception to the rule forbidding white space, the form **Image settings** is also allowed to guarantee compatibility with data files that were saved in the early phases of development, however it is recommended that such files are converted to the new form as soon as they are discovered.
- The **[Field Specifications]** are determined by the field names in the UI, the naming can change, but the order and meaning will be preserved in future versions. At the time of writing **[Field Specifications]** is:
  - **Height**, the vertical extent of the scanned area in motor coordinates[1].
  - **Width (mm)**, the horizontal extent of the scanned area in motor coordinates.
  - **Xstart**, the abscissa position of the first pixel of the raster scan in motor coordinates.

[1] Currently the motor units are mm for all imaging axes, but it can change if the motor is replaced with a different model.

  - **Ystart**, the ordinate position of the first pixel of the raster scan in motor coordinates.
  - **XStep**, the length of the raster scan step along the abscissa.
  - **YStep**, the length of the raster scan step along the ordinate.
  - **Scans per pixel**, the number of scans that will be saved in the **DataXYn** block nested in each **Pixel**.
  - **Pixel delay**, the waiting time passing between the completion of the motion between pixels and the start of the THz measurement.
  - **Transpose** tells whether or not the image has to be transposed to match its orientation with that of the sample: unlike all other fields this one holds a boolean value.

- An image block contains as many nested **Pixel** as there are raster scan points in the image (at least one), where their number can be evaluated as:

$$N_{pixel} = \left\lfloor \frac{Heigh}{X\_Step} + 1 \right\rfloor \cdot \left\lfloor \frac{Width}{Y\_Step} + 1 \right\rfloor . \tag{A.1}$$

- The pixels are recorded in acquisition order, rather than raster order. This is practically the same for raster images, but it can be very different if the pixel visitation order is more complex or a sparse imaging is implemented. In the latter case it would be probably easier to create a specialized variant of this block.

The format for raster images is significantly more complex than the others and cannot be read using standard tools, such as the MATLAB® functions **`readfields`**, **`csvread`** and **`textscan`**: a dedicated function has to be written. Example implementations of a function capable to read a file containing *only one* image block are given in the following for two major programming languages used in data analysis: MATLAB®, in listing A.1, at page 83 and Python™ (version 3.7 or higher), in listing A.2, at page 86.

These solutions do not use all the information in the block, but are robust enough to reliably read all the image data into a four dimensional array, as well as to provide arrays for the X-Y coordinates of the raster scan points and the times (probe delay) at which the THz signal has been sampled. Since the data files use a structured textual format, they are relatively simple to inspect visually by the researchers, but are way larger than the size of the bare data so, for the sake of speed, once the image data have been read, it is recommended to save them into a binary format, such as the one produced by the MATLAB® function **`save`** or the Python™ function **`scipy.io.savemat`** requiring the installation of the additional **`scipi`** library.

Listing A.1: MATLAB® function that receives as input the path to a file containing one **Block** of type **ImageSettings** and returns the image data in a four-dimensional array together with the X and Y coordinates of the raster scan grid points and the sampling times of the THz traces, each inside a one-dimensional array.

```
function [img, xrange, yrange, ...
  time, Transpose, pixeldelay] = readimg(file)
  fid = fopen(file);
  line_nr = 0;

  while ~feof(fid)
    a_line = fgetl(fid);
    line_nr = line_nr+1;
    if regexp(a_line, '# \[Record:Pixel\]')
      try
        fgetl(fid);
        a_line = fgetl(fid);
        line_nr = line_nr + 1;
        values = num2cell( ...
          str2double(strsplit(a_line, ', ')));
        [row, col, ~, ~] = values{:};
        row = row + 1;
        col = col + 1;
      catch
        fprintf('error2 encountered at line %d\n', line_nr);
      end
    elseif regexp(a_line, '# \[DataXYn:THzSignal\]')
```

```
    try
      fgetl(fid);
      a_line = fgetl(fid);
      line_nr = line_nr + 2;
      time = str2double(strsplit(a_line, ', '));
      scansize = length(time);
      if scansize > size(img, 4)
        % pad array to the correct size
        img = padarray( ...
          img, [0, 0, 0, ...
           scansize - size(img,4)], 0, 'post');
      end

      for scan = 1:scanperpixel
        a_line = fgetl(fid);
        line_nr = line_nr + 1;
        temp = str2double(strsplit(a_line, ', '));
        assert(scansize == length(temp));
        img(row, col, scan,:) = temp;
      end
    catch
      fprintf('error3 encountered at line %d ', line_nr);
      fprintf('scansize = %d, ', scansize);
      fprintf('actually = %d\n', length(temp));
    end

  elseif regexp(a_line, '# \[Record:Image( s|S)ettings\]')
```

```
        % Match Label ImageSettings,
        % allow old style Label "Image settings"
        % This case is executed only once at the start
        % It is the last case for performance reasons.
        try
          fgetl(fid);
          a_line = fgetl(fid);
          tokens = strsplit(a_line, ', ');
          line_nr = line_nr + 2;
          nums = num2cell(str2double(tokens));
          Transpose = strcmpi(tokens{end}, 'TRUE');
          [height, width, xstart, ystart, ...
            xstep, ystep, scanperpixel, pixeldelay]= nums{:};
          xrange = linspace(xstart, xstart+height, ...
                            floor(height/xstep) + 1);
          yrange = linspace(ystart, ystart+width, ...
                            floor(width/ystep) + 1);
          img = zeros([length(xrange), length(yrange), ...
                     scanperpixel, 1]);
        catch
          fprintf('error1 encountered at line %d\n', line_nr);
        end
      end
    end
    fclose(fid);
end
```

Listing A.2: Python™ (v 3.7+) function that receives as input the path to a file containing one **Block** of type **ImageSettings** and returns the image data in a four-dimensional array together with the X and Y coordinates of the raster scan grid points and the sampling times of the THz traces, each inside a one-dimensional array. For the sake of efficient numerical calculation, This function relies on module **`numpy`** which has to be installed separately, all the other imported modules are part of the Standard Library, hence available out-of-the-box. to load and save data in the binary format used by MATLAB® the additional **`scipy`** library must be installed too.

```
#!/usr/bin/env python3
from collections import namedtuple
import io, re, numpy as np
from pathlib import Path
imghead = re.compile(r'#␣\[Record:Image(␣s|S)ettings\]')
pixhead = re.compile(r'#␣\[Record:Pixel\]')
sighead = re.compile(r'#␣\[DataXYn:THzSignal\]')
tkon = (float, float, float, float, float, float,
        lambda s: int(float(s)), float, lambda s: s == 'TRUE\n')
tokens = namedtuple('tokens', 'height,␣width,␣xstart,␣ystart,␣'
                    'xstep,␣ystep,␣scanperpixel,␣pixdelay,␣transpose')

def do_range(start, span, step):
    return np.linspace(
        start, start+span, np.floor(span/step)+1, endpoint=True)
def fill_scan(img, row, col, scan, values):
    try:
        img[row, col, scan, :] = values
    except (IndexError, TypeError):
```

```
            # No img array yet: create it
            img = np.zeros(img.shape + (len(values),))
            img[row, col, scan, :] = values
    return img
def always(seq):
    while True:
        yield from seq
def getvalues(a_line, start=None, stop=None, conv=(float,)):
    idx = slice(start, stop)
    pairs = zip(a_line.split(', ')[idx], always(conv))
    yield from ([c(n) for n, c in pairs])
def readimg(afile, closeafter=True):
    if isinstance(afile, io.TextIOBase):
        fid = afile
        closeafter = False
    elif isinstance(afile, (str, Path)):
        fid = open(afile, 'r')
    par = img = time = xrange = yrange = None
    loop = enumerate(fid)
    for line_nr, a_line in loop:
        if pixhead.match(a_line):
            next(loop)
            line_nr, a_line = next(loop)
            row, col = getvalues(a_line, stop=2, conv=(tkon[6],))
        elif sighead.match(a_line):
            next(loop)
            line_nr, a_line = next(loop)
```

```
            try:
                time = np.fromiter(getvalues(a_line), float)
                for scan in range(par.scanperpixel):
                    line_nr, a_line = next(loop)
                    values = np.fromiter(getvalues(a_line), float)
                    img = fill_scan(img, row, col, scan, values)
            except ValueError:
                print(f'Error reading line {line_nr}')
                try:
                    print(f'File {fid.name} may be corrupt!')
                except AttributeError:
                    pass
                return (None,) * 6
        elif imghead.match(a_line):
            # This case is executed only once at the start
            # It is the last case for performance reasons.
            next(loop)
            line_nr, a_line = next(loop)
            par = tokens(*getvalues(a_line, conv=tkon))
            xrange = do_range(par.xstart, par.height, par.xstep)
            yrange = do_range(par.ystart, par.width, par.ystep)
            img = np.empty(
                [len(xrange), len(yrange), par.scanperpixel])
    if closeafter:
        fid.close()
    return img, xrange, yrange, time, par.transpose, par.pixdelay
```

Bibliography

[1] H. Ritchie and M. Roser. Causes of Death. https://ourworldindata.org/causes-of-death, February 2018.

[2] A. Urruticoechea, R. Alemany, J. Balart, A. Villanueva, F. Viñals, and G. Capellá. Recent advances in cancer therapy: An overview. *Current Pharmaceutical Design*, 16(1):3–10, January 2010.

[3] R. Baskar, K. A. Lee, R. Yeo, and K.-W. Yeoh. Cancer and Radiation Therapy: Current Advances and Future Directions. *International Journal of Medical Sciences*, 9(3):193–199, 2012.

[4] T. J. Dougherty, C. J. Gomer, B. W. Henderson, G. Jori, D. Kessel, M. Korbelik, J. Moan, and Q. Peng. Photodynamic Therapy. *Journal of the National Cancer Institute*, 90(12):889–905, June 1998.

[5] L. Zou, H. Wang, B. He, L. Zeng, T. Tan, H. Cao, X. He, Z. Zhang, S. Guo, and Y. Li. Current Approaches of Photothermal Therapy in Treating Cancer Metastasis with Nanotherapeutics. *Theranostics*, 6(6):762–772, 2016.

[6] J.-E. Park, M. Kim, J.-H. Hwang, and J.-M. Nam. Golden Opportunities: Plasmonic Gold Nanostructures for Biomedical Applications based on the Second Near-Infrared Window. *Small Methods*, 1(3):1600032, 2017.

[7] R. S. Riley and E. S. Day. Gold nanoparticle-mediated photothermal therapy: Applications and opportunities for multimodal cancer treatment. *Wiley Interdisciplinary Reviews. Nanomedicine and Nanobiotechnology*, 9(4):e1449, July 2017.

[8] D. de Melo-Diogo, C. Pais-Silva, D. R. Dias, A. F. Moreira, and I. J. Correia. Strategies to Improve Cancer Photothermal Therapy Mediated by Nanomaterials. *Advanced Healthcare Materials*, 6(10):1700073, 2017.

[9] D. Van Straten, V. Mashayekhi, H. S. De Bruijn, S. Oliveira, and D. J. Robinson. Oncologic Photodynamic Therapy: Basic Principles, Current Clinical Status and Future Directions. *Cancers*, 9(2):19, February 2017.

[10] Public Health Agency of Canada. *Cancer in Canada - an Epidemiological Overview: A Report Based on the Cancer Incidence Atlas - Volume 2, 2000-2006.* Public Health Agency of Canada, Ottawa, ON, Ottawa, February 2014.

[11] G. Urban, A. Jachimowicz, F. Kohl, H. Kuttner, F. Olcaytug, H. Kamper, F. Pittner, E. Mann-Buxbaum, T. Schalkhammer, O. Prohaska, and M. Schönauer. High-resolution thin-film temperature sensor arrays for medical applications. *Sensors and Actuators A: Physical*, 22(1):650–654, June 1990.

[12] G. J. Tattersall. Infrared thermography: A non-invasive window into thermal physiology. *Comparative Biochemistry and Physiology Part A: Molecular & Integrative Physiology*, 202:78–98, December 2016.

[13] L. J. Jiang, E. Y. K. Ng, A. C. B. Yeo, S. Wu, F. Pan, W. Y. Yau, J. H. Chen, and Y. Yang. A perspective on medical infrared imaging. *Journal of Medical Engineering & Technology*, 29(6):257–267, January 2005.

[14] R. Usamentiaga, P. Venegas, J. Guerediaga, L. Vega, J. Molleda, and F. G. Bulnes. Infrared Thermography for Temperature Measurement and Non-Destructive Testing. *Sensors (Basel, Switzerland)*, 14(7):12305–12348, July 2014.

[15] B. B. Lahiri, S. Bagavathiappan, T. Jayakumar, and J. Philip. Medical applications of infrared thermography: A review. *Infrared Physics & Technology*, 55(4):221–235, July 2012.

[16] E. F. J. Ring and K. Ammer. Infrared thermal imaging in medicine. *Physiological Measurement*, 33(3):R33–R46, February 2012.

[17] D. Jaque, B. del Rosal, E. M. Rodríguez, L. M. Maestro, P. Haro-González, and J. G. Solé. Fluorescent nanothermometers for intracellular thermal sensing. *Nanomedicine*, 9(7):1047–1062, May 2014.

[18] X.-d. Wang, O. S. Wolfbeis, and R. J. Meier. Luminescent probes and sensors for temperature. *Chemical Society Reviews*, 42(19):7834–7869, September 2013.

[19] D. Jaque and F. Vetrone. Luminescence nanothermometry. *Nanoscale*, 4(15):4301–4326, July 2012.

[20] C. D. S. Brites, P. P. Lima, N. J. O. Silva, A. Millán, V. S. Amaral, F. Palacio, and L. D. Carlos. Thermometry at the nanoscale. *Nanoscale*, 4(16):4799–4829, July 2012.

[21] L. M. Maestro, P. Haro-González, M. C. Iglesias-de la Cruz, F. SanzRodríguez, Á. Juarranz, J. G. Solé, and D. Jaque. Fluorescent nanothermometers provide controlled plasmonic-mediated intracellular hyperthermia. *Nanomedicine*, 8(3):379–388, December 2012.

[22] F. Vetrone, R. Naccache, A. Zamarrón, A. Juarranz de la Fuente, F. Sanz-Rodríguez, L. Martinez Maestro, E. Martín Rodriguez, D. Jaque, J. García Solé, and J. A. Capobianco. Temperature Sensing Using Fluorescent Nanothermometers. *ACS Nano*, 4(6):3254–3258, June 2010.

[23] M. Scheller. Data Extraction from Terahertz Time Domain Spectroscopy Measurements. *Journal of Infrared, Millimeter, and Terahertz Waves*, 35(8):638–648, January 2014.

[24] I. Pupeza, R. Wilk, and M. Koch. Highly accurate optical material parameter determination with THz time-domain spectroscopy. *Optics Express*, 15(7):4335–4350, April 2007.

[25] C. Rø nne and S. r. R. Keiding. Low frequency spectroscopy of liquid water using THz-time domain spectroscopy. *Journal of Molecular Liquids*, 101(1):199–218, November 2002.

[26] C. Rø nne, L. Thrane, P.-O. Å strand, A. Wallqvist, K. V. Mikkelsen, and S. R. Keiding. Investigation of the temperature dependence of dielectric relaxation in liquid water by THz reflection spectroscopy and molecular dynamics simulation. *The Journal of Chemical Physics*, 107(14):5319–5331, October 1997.

[27] X.-C. Zhang and J. Xu. *Introduction to THz Wave Photonics*. Springer US, 2010.

[28] S. S. Dhillon, M. S. Vitiello, E. H. Linfield, A. G. Davies, M. C. Hoffmann, J. Booske, C. Paoloni, M. Gensch, P. Weightman, G. P. Williams, E. Castro-Camus, D. R. S. Cumming, F. Simoens, I. Escorcia-Carranza, J. Grant, S. Lucyszyn, M. Kuwata-Gonokami, K. Konishi, M. Koch, C. A. Schmuttenmaer, T. L. Cocker, R. Huber, A. G. Markelz, Z. D. Taylor, V. P. Wallace, J. A. Zeitler, J. Sibik, T. M. Korter, B. Ellison, S. Rea, P. Goldsmith, K. B. Cooper, R. Appleby, D. Pardo, P. G. Huggard, V. Krozer, H. Shams, M. Fice, C. Renaud, A. Seeds, A. Stöhr, M. Naftaly, N. Ridler, R. Clarke, J. E. Cunningham, and M. B. Johnston. The 2017 terahertz science and technology roadmap. *Journal of Physics D: Applied Physics*, 50(4):043001, January 2017.

[29] S. J. Oh, J. Kang, I. Maeng, J.-S. Suh, Y.-M. Huh, S. Haam, and J.-H. Son. Nanoparticle-enabled terahertz imaging for cancer diagnosis. *Optics Express*, 17(5):3469–3475, March 2009.

[30] S. J. Oh, J. Choi, I. Maeng, J. Y. Park, K. Lee, Y.-M. Huh, J.-S. Suh, S. Haam, and J.-H. Son. Molecular imaging with terahertz waves. *Optics Express*, 19(5):4009–4016, February 2011.

[31] A. Stylianou and M. A. Talias. Nanotechnology-supported THz medical imaging. *F1000Research*, 2:100, March 2013.

[32] F. Novelli, J. W. M. Chon, and J. A. Davis. Terahertz thermometry of gold nanospheres in water. *Optics Letters*, 41(24):5801–5804, December 2016.

[33] R. Naccache, A. Mazhorova, M. Clerici, R. Piccoli, L. K. Khorashad, A. O. Govorov, L. Razzari, F. Vetrone, and R. Morandotti. Terahertz Thermometry: Combining Hyperspectral Imaging and Temperature Mapping at Terahertz Frequencies. *Laser & Photonics Reviews*, 11(5):n/a–n/a, September 2017.

[34] B. Baroli, M. G. Ennas, F. Loffredo, M. Isola, R. Pinna, and M. Arturo López-Quintela. Penetration of Metallic Nanoparticles in Human Full-Thickness Skin. *Journal of Investigative Dermatology*, 127(7):1701–1712, July 2007.

[35] K. W. Kim, H. Kim, J. Park, J. K. Han, and J. Son. Terahertz Tomographic Imaging of Transdermal Drug Delivery. *IEEE Transactions on Terahertz Science and Technology*, 2(1):99–106, January 2012.

[36] P. R. Smith, D. H. Auston, and M. C. Nuss. Subpicosecond photoconducting dipole antennas. *IEEE Journal of Quantum Electronics*, 24(2):255–260, February 1988.

[37] A. Nahata, A. S. Weling, and T. F. Heinz. A wideband coherent terahertz spectroscopy system using optical rectification and electro-optic sampling. *Applied Physics Letters*, 69(16):2321–2323, October 1996.

[38] R. Köhler, A. Tredicucci, F. Beltram, H. E. Beere, E. H. Linfield, A. G. Davies, D. A. Ritchie, R. C. Iotti, and F. Rossi. Terahertz semiconductor-heterostructure laser. *Nature*, 417(6885):156–159, May 2002.

[39] B. Yu, F. Zeng, Y. Yang, Q. Xing, A. Chechin, X. Xin, I. Zeylikovich, and R. Alfano. Torsional Vibrational Modes of Tryptophan Studied by Terahertz Time-Domain Spectroscopy. *Biophysical Journal*, 86(3):1649–1654, March 2004.

[40] N. Y. Tan, M. T. Ruggiero, C. Orellana-Tavra, T. Tian, A. D. Bond, T. M. Korter, D. Fairen-Jimenez, and J. A. Zeitler. Investigation of the terahertz vibrational modes of ZIF-8 and ZIF-90 with terahertz time-domain spectroscopy. *Chemical Communications (Cambridge, England)*, 51(89):16037–16040, November 2015.

[41] M. Walther, P. Plochocka, B. Fischer, H. Helm, and P. Uhd Jepsen. Collective vibrational modes in biological molecules investigated by terahertz time-domain spectroscopy. *Biopolymers*, 67(4-5):310–313, January 2002.

[42] J. Hohlfeld, S. S. Wellershoff, J. Güdde, U. Conrad, V. Jähnke, and E. Matthias. Electron and lattice dynamics following optical excitation of metals. *Chemical Physics*, 251(1–3):237–258, January 2000.

[43] I. Ivanov, Y. Hu, U. Beser, A. Narita, K. Müllen, M. Bonn, and D. Turchinovich. Terahertz Carrier Dynamics in Graphene Nanoribbons with Different Peripherial Functional Groups. In *Conference on Lasers and Electro-Optics (2016), Paper SM3L.6*, page SM3L.6, San Jose, CA, USA, June 2016. Optical Society of America.

[44] T. Chari. *Optimization Studies in Graphene Electronics*. Ph.D., Columbia University, 2016.

[45] C. A. Schmuttenmaer. Exploring Dynamics in the Far-Infrared with Terahertz Spectroscopy. *Chemical Reviews*, 104(4):1759–1780, April 2004.

[46] P. Griffiths and J. A. De Haseth. *Fourier Transform Infrared Spectrometry*. Chemical Analysis: A Series of Monographs on Analytical Chemistry and Its Applications. Wiley-Interscience, second edition, 2007.

[47] M. Naftaly and R. E. Miles. Terahertz Time-Domain Spectroscopy for Material Characterization. *Proceedings of the IEEE*, 95(8):1658–1665, August 2007.

[48] M. R. Kutteruf, C. M. Brown, L. K. Iwaki, M. B. Campbell, T. M. Korter, and E. J. Heilweil. Terahertz spectroscopy of short-chain polypeptides. *Chemical Physics Letters*, 375(3):337–343, July 2003.

[49] A. G. Markelz, A. Roitberg, and E. J. Heilweil. Pulsed terahertz spectroscopy of DNA, bovine serum albumin and collagen between 0.1 and 2.0 THz. *Chemical Physics Letters*, 320(1):42–48, March 2000.

[50] M. R. Leahy-Hoppa, M. J. Fitch, X. Zheng, L. M. Hayden, and R. Osiander. Wideband terahertz spectroscopy of explosives. *Chemical Physics Letters*, 434(4):227–230, February 2007.

[51] Y.-S. Jin, G.-J. Kim, and S.-G. Jeon. Terahertz Dielectric Properties of Polymers. *Journal of the Korean Physical Society*, 49(2):513, August 2006.

[52] M. Naftaly, J. F. Molloy, G. V. Lanskii, K. A. Kokh, and Y. M. Andreev. Terahertz time-domain spectroscopy for textile identification. *Applied Optics*, 52(19):4433–4437, July 2013.

[53] D. Banerjee, W. von Spiegel, M. D. Thomson, S. Schabel, and H. G. Roskos. Diagnosing water content in paper by terahertz radiation. *Optics Express*, 16(12):9060–9066, June 2008.

[54] Y. Liu, J. Tan, L. Jiang, S. Shi, B. Jin, and J. Ma. Diagnostic technique of pine wood nematode disease based on THz spectrum. In *SPIE (7277), Photonics and Optoelectronics Meetings (POEM) 2008: Terahertz Science and Technology*, volume 7277, page 72770V, Wuhan, China, February 2009. International Society for Optics and Photonics.

[55] K. Ahi and M. Anwar. Advanced terahertz techniques for quality control and counterfeit detection. In *SPIE (9856):Terahertz Physics, Devices, and Systems X: Advanced Applications in Industry and Defense*, volume 9856, pages 98560G+, Baltimore, MD, USA, 2016.

[56] J. Dong, A. Locquet, M. Melis, and D. S. Citrin. Global mapping of stratigraphy of an old-master painting using sparsity-based terahertz reflectometry. *Scientific Reports*, 7(1):15098, November 2017.

[57] E. Pickwell-MacPherson. Practical considerations for in vivo THz imaging. *Terahertz Science and Technology*, 3(4):163–171, December 2010.

[58] R. I. Stantchev, B. Sun, S. M. Hornett, P. A. Hobson, G. M. Gibson, M. J. Padgett, and E. Hendry. Noninvasive, near-field terahertz imaging of hidden objects using a single-pixel detector. *Science Advances*, 2(6):e1600190, June 2016.

[59] D. Suzuki, S. Oda, and Y. Kawano. A flexible and wearable terahertz scanner. *Nature Photonics*, 10(12):809–813, November 2016.

[60] T. Ouchi, K. Kajiki, T. Koizumi, T. Itsuji, Y. Koyama, R. Sekiguchi, O. Kubota, and K. Kawase. Terahertz Imaging System for Medical Applications and Related High Efficiency Terahertz Devices. *Journal of Infrared, Millimeter, and Terahertz Waves*, 35(1):118–130, January 2014.

[61] H.-B. Liu, Y. Chen, G. J. Bastiaans, and X.-C. Zhang. Detection and identification of explosive RDX by THz diffuse reflection spectroscopy. *Optics Express*, 14(1):415–423, January 2006.

[62] J. Dai, X. Guo, and X.-C. Zhang. Terahertz air photonics for standoff explosive detection. In *IEEE Conference on Technologies for Homeland Security, 2009. HST '09*, pages 461–464, May 2009.

[63] S. Verghese, K. A. McIntosh, and E. R. Brown. Highly tunable fiber-coupled photomixers with coherent terahertz output power. *IEEE Transactions on Microwave Theory and Techniques*, 45(8):1301–1309, August 1997.

[64] M. van Exter and D. Grischkowsky. Characterization of an optoelectronic terahertz beam system. *IEEE Transactions on Microwave Theory and Techniques*, 38(11):1684–1691, November 1990.

[65] G. Grüner. *Millimeter and Submillimeter Wave Spectroscopy of Solids*, volume 74 of *Topics in Applied Physics*. Springer, Berlin, Heidelberg, 1998.

[66] Y.-S. Lee. *Principles of Terahertz Science and Technology*. Springer US, Boston, MA, 2009.

[67] W. Shi, Y. J. Ding, N. Fernelius, and K. Vodopyanov. Efficient, tunable, and coherent 0.18–5.27-THz source based on GaSe crystal. *Optics Letters*, 27(16):1454–1456, August 2002.

[68] K. Kawase, J.-i. Shikata, K. Imai, and H. Ito. Transform-limited, narrow-linewidth, terahertz-wave parametric generator. *Applied Physics Letters*, 78(19):2819–2821, May 2001.

[69] K. J. Siebert, H. Quast, R. Leonhardt, T. Löffler, M. Thomson, T. Bauer, H. G. Roskos, and S. Czasch. Continuous-wave all-optoelectronic terahertz imaging. *Applied Physics Letters*, 80(16):3003–3005, April 2002.

[70] I. S. Gregory, W. R. Tribe, C. Baker, B. E. Cole, M. J. Evans, L. Spencer, M. Pepper, and M. Missous. Continuous-wave terahertz system with a 60 dB dynamic range. *Applied Physics Letters*, 86(20):204104, May 2005.

[71] Y. Wang, Z. Zhao, Z. Chen, L. Zhang, K. Kang, and J. Deng. Continuous-wave terahertz phase imaging using a far-infrared laser interferometer. *Applied Optics*, 50(35):6452–6460, December 2011.

[72] Q. Wu, M. Litz, and X.-C. Zhang. Broadband detection capability of ZnTe electro-optic field detectors. *Applied Physics Letters*, 68(21):2924–2926, May 1996.

[73] A. Stöhr and D. Jäger. THz photomixers: An overview. In *SPIE (6194) Millimeter-Wave and Terahertz Photonics*, volume 6194, page 61940D (8), Strasbourg, France, 2006.

[74] N. Kim, S.-P. Han, H. Ko, Y. A. Leem, H.-C. Ryu, C. W. Lee, D. Lee, M. Y. Jeon, S. K. Noh, and K. H. Park. Tunable continuous-wave terahertz generation/detection with compact 1.55 Mm detuned dual-mode laser diode and InGaAs based photomixer. *Optics Express*, 19(16):15397–15403, August 2011.

[75] H. Tanoto, J. H. Teng, Q. Y. Wu, M. Sun, Z. N. Chen, S. A. Maier, B. Wang, C. C. Chum, G. Y. Si, A. J. Danner, and S. J. Chua. Nano-antenna in a photoconductive photomixer for highly efficient continuous wave terahertz emission. *Scientific Reports*, 3, October 2013.

[76] G. W. Chantry. Long-wave optics: The science and technology of infrared and near-millimetre waves. Applications. *Astrophysics*, 2:379, 1984.

[77] M. Inguscio, G. Moruzzi, K. M. Evenson, and D. A. Jennings. A review of frequency measurements of optically pumped lasers from 0.1 to 8 THz. *Journal of Applied Physics*, 60(12):R161–R192, December 1986.

[78] A. Bergner, U. Heugen, E. Bründermann, G. Schwaab, M. Havenith, D. R. Chamberlin, and E. E. Haller. New p-Ge THz laser spectrometer for the study of solutions: THz absorption spectroscopy of water. *Review of Scientific Instruments*, 76(6):063110, May 2005.

[79] C. Dahl, L. Genzel, P. Goy, G. Grüner, J. P. Kotthaus, G. Kozlov, M. C. Nuss, J. Orenstein, and A. Volkov. *Millimeter and Submillimeter Wave Spectroscopy of Solids*. Springer, softcover reprint of the original 1st ed. 1998 edition, August 2013.

[80] J. Faist, F. Capasso, D. L. Sivco, C. Sirtori, A. L. Hutchinson, and A. Y. Cho. Quantum Cascade Laser. *Science*, 264(5158):553–556, April 1994.

[81] Y. Yao, A. J. Hoffman, and C. F. Gmachl. Mid-infrared quantum cascade lasers. *Nature Photonics*, 6(7):432–439, July 2012.

[82] S. Fathololoumi, E. Dupont, C. W. I. Chan, Z. R. Wasilewski, S. R. Laframboise, D. Ban, A. Mátyás, C. Jirauschek, Q. Hu, and H. C. Liu. Terahertz quantum cascade lasers operating up to $\sim$ 200 K with optimized oscillator strength and improved injection tunneling. *Optics Express*, 20(4):3866–3876, February 2012.

[83] F. Castellano, S. Zanotto, L. H. Li, A. Pitanti, A. Tredicucci, E. H. Linfield, A. G. Davies, and M. S. Vitiello. Distributed feedback terahertz frequency quantum cascade lasers with dual periodicity gratings. *Applied Physics Letters*, 106(1):011103, January 2015.

[84] R. Degl'Innocenti, Y. D. Shah, L. Masini, A. Ronzani, A. Pitanti, Y. Ren, D. S. Jessop, A. Tredicucci, H. E. Beere, and D. A. Ritchie. Hyperuniform disordered terahertz quantum cascade laser. *Scientific Reports*, 6:19325, January 2016.

[85] LongWave Photonics LLC. Terahertz Quantum Cascade Lasers. http://longwavephotonics.com/terahertz-quantum-cascade-lasers.html.

[86] S. G. Razavipour, E. Dupont, S. Fathololoumi, C. W. I. Chan, M. Lindskog, Z. R. Wasilewski, G. Aers, S. R. Laframboise, A. Wacker, Q. Hu, D. Ban, and H. C. Liu. An indirectly pumped terahertz quantum cascade laser with low injection coupling strength operating above 150 K. *Journal of Applied Physics*, 113(20):203107, May 2013.

[87] J. F. Webb. A possible room temperature terrahertz wave source via harmonic generation in a microwave pumped ferroelectric crystal. In *2009 Asia Pacific Microwave Conference*, pages 186–189, Singapore, December 2009.

[88] W. Li and J. Yao. Microwave and Terahertz Generation Based on Photonically Assisted Microwave Frequency Twelvetupling With Large Tunability. *IEEE Photonics Journal*, 2(6):954–959, December 2010.

[89] A. Maestrini, J. S. Ward, J. J. Gill, H. S. Javadi, E. Schlecht, C. Tripon-Canseliet, G. Chattopadhyay, and I. Mehdi. A 540-640-GHz high-efficiency four-anode frequency tripler. *IEEE Transactions on Microwave Theory and Techniques*, 53(9):2835–2843, September 2005.

[90] E. H. Putley. Indium Antimonide Submillimeter Photoconductive Detectors. *Applied Optics*, 4(6):649–657, June 1965.

[91] P. Yagoubov, M. Kroug, H. Merkel, E. Kollberg, G. Gol'tsman, S. Svechnikov, and E. Gershenzon. Noise temperature and local oscillator power requirement of NbN phonon-cooled hot electron bolometric mixers at terahertz frequencies. *Applied Physics Letters*, 73(19):2814–2816, November 1998.

[92] A. Skalare, W. R. McGrath, B. Bumble, H. G. LeDuc, P. J. Burke, A. A. Verheijen, R. J. Schoelkopf, and D. E. Prober. Large bandwidth and low noise in a diffusion-cooled hot-electron bolometer mixer. *Applied Physics Letters*, 68(11):1558–1560, March 1996.

[93] K. Ravi, W. R. Huang, S. Carbajo, E. A. Nanni, D. N. Schimpf, E. P. Ippen, and F. X. Kärtner. Theory of terahertz generation by optical rectification using tilted-pulse-fronts. *Optics Express*, 23(4):5253–5276, February 2015.

[94] R. Ulbricht, E. Hendry, J. Shan, T. F. Heinz, and M. Bonn. Carrier dynamics in semiconductors studied with time-resolved terahertz spectroscopy. *Reviews of Modern Physics*, 83(2):543–586, June 2011.

[95] R. W. Boyd. *Nonlinear Optics, Third Edition*. Academic Press, Amsterdam ; Boston, 3 edition edition, April 2008.

[96] Z. Zhao, A. Schwagmann, F. Ospald, D. C. Driscoll, H. Lu, A. C. Gossard, and J. H. Smet. Thickness dependence of the terahertz response in $\langle 110 \rangle$-oriented GaAs crystals for electro-optic sampling at 1.55 Mm. *Optics Express*, 18(15):15956–15963, July 2010.

[97] H. Hamster, A. Sullivan, S. Gordon, W. White, and R. W. Falcone. Subpicosecond, electromagnetic pulses from intense laser-plasma interaction. *Physical Review Letters*, 71(17):2725–2728, October 1993.

[98] H. Hamster, A. Sullivan, S. Gordon, and R. W. Falcone. Short-pulse terahertz radiation from high-intensity-laser-produced plasmas. *Physical Review E*, 49(1):671–677, January 1994.

[99] T. Löffler, F. Jacob, and H. G. Roskos. Generation of terahertz pulses by photoionization of electrically biased air. *Applied Physics Letters*, 77(3):453, July 2000.

[100] T. Bartel, P. Gaal, K. Reimann, M. Woerner, and T. Elsaesser. Generation of single-cycle THz transients with high electric-field amplitudes. *Optics Letters*, 30(20):2805–2807, October 2005.

[101] V. A. Andreeva, O. G. Kosareva, N. A. Panov, D. E. Shipilo, P. M. Solyankin, M. N. Esaulkov, P. González de Alaiza Martínez, A. P. Shkurinov, V. A. Makarov, L. Bergé, and S. L. Chin. Ultrabroad Terahertz Spectrum Generation from an Air-Based Filament Plasma. *Physical Review Letters*, 116(6):063902, February 2016.

[102] A. V. Balakin, A. V. Borodin, I. A. Kotelnikov, and A. P. Shkurinov. Terahertz emission from a femtosecond laser focus in a two-color scheme. *JOSA B*, 27(1):16–26, January 2010.

[103] K. Y. Kim, J. H. Glownia, A. J. Taylor, and G. Rodriguez. Terahertz emission from ultrafast ionizing air in symmetry-broken laser fields. *Optics Express*, 15(8):4577–4584, April 2007.

[104] M. Kreß, T. Löffler, M. D. Thomson, R. Dörner, H. Gimpel, K. Zrost, T. Ergler, R. Moshammer, U. Morgner, J. Ullrich, and H. G. Roskos. Determination of the carrier-envelope phase of few-cycle laser pulses with terahertz-emission spectroscopy. *Nature Physics*, 2(5):327–331, May 2006.

[105] M. Clerici, M. Peccianti, B. E. Schmidt, L. Caspani, M. Shalaby, M. Giguère, A. Lotti, A. Couairon, F. Légaré, T. Ozaki, D. Faccio, and R. Morandotti. Wavelength Scaling of Terahertz Generation by Gas Ionization. *Physical Review Letters*, 110(25):253901, June 2013.

[106] T. Nagatsuma, S. Horiguchi, Y. Minamikata, Y. Yoshimizu, S. Hisatake, S. Kuwano, N. Yoshimoto, J. Terada, and H. Takahashi. Terahertz wireless communications based on photonics technologies. *Optics Express*, 21(20):23736–23747, October 2013.

[107] R. E. Collin. *Foundations For Microwave Engineering, 2Nd Ed*. BWSTM, New Delhi, 2 edition edition, January 2007.

[108] Federal Communications Commission. FCC online table of Radio Spectrum Allocation, March 2011.

[109] I. Dey, K. Jana, V. Y. Fedorov, A. D. Koulouklidis, A. Mondal, M. Shaikh, D. Sarkar, A. D. Lad, S. Tzortzakis, A. Couairon, and G. R. Kumar. Highly efficient broadband terahertz generation from ultrashort laser filamentation in liquids. *Nature Communications*, 8(1):1184, October 2017.

[110] A. N. Tcypkin, E. A. Ponomareva, S. E. Putilin, S. V. Smirnov, S. A. Shtumpf, M. V. Melnik, Y. E, S. A. Kozlov, and X.-C. Zhang. Flat liquid jet as a highly efficient source of terahertz radiation. *Optics Express*, 27(11):15485–15494, May 2019.

[111] M. Clerici, A. Mazhorova, S. P. Ho, M. Peccianti, A. Pasquazi, L. Razzari, J. Ali, and R. Morandotti. On Chip Broadband Terahertz Detection via Four-Wave Mixing in Electrically Biased Silica Micro-Slits. In *Advanced Photonics*, OSA Technical Digest (Online), page NTu4A.3, Barcelona, Spain, July 2014. Optical Society of America.

[112] A. Tomasino, R. Piccoli, D. Caraffini, A. Markov, A. Mazhorova, R. Naccache, F. Vetrone, Y. Jestin, A. Busacca, L. Razzari, and R. Morandotti. Ultra-broadband terahertz time domain spectroscopy by Solid State Biased Coherent Detection. In *2017 42nd International Conference on Infrared, Millimeter, and Terahertz Waves (IRMMW-THz)*, pages 1–2, Cancún, Mexico, August 2017.

[113] A. Tomasino, A. Mazhorova, M. Clerici, M. Peccianti, S.-P. Ho, Y. Jestin, A. Pasquazi, A. Markov, X. Jin, R. Piccoli, S. Delprat, M. Chaker, A. Busacca, J. Ali, L. Razzari, and R. Morandotti. Solid-state-biased coherent detection of ultra-broadband terahertz pulses. *Optica*, 4(11):1358–1362, November 2017.

[114] A. Tomasino, R. Piccoli, Y. Jestin, A. Busacca, S. Delprat, M. Chaker, M. Peccianti, M. Clerici, L. Razzari, and R. Morandotti. Silicon nitride-based deep sub-λ slit for ultra-broadband THz coherent detection. In *2018 Conference on Lasers and Electro-Optics (CLEO)*, pages 1–2, San Jose, CA, USA, May 2018.

[115] F. Ganikhanov, G.-R. Lin, W.-C. Chen, C.-S. Chang, and C.-L. Pan. Subpicosecond carrier lifetimes in arsenic-ion-implanted GaAs. *Applied Physics Letters*, 67(23):3465–3467, December 1995.

[116] R. J. B. Dietz, B. Globisch, H. Roehle, D. Stanze, T. Göbel, and M. Schell. Influence and adjustment of carrier lifetimes in InGaAs/InAlAs photoconductive pulsed terahertz detectors: 6 THz bandwidth and 90dB dynamic range. *Optics Express*, 22(16):19411–19422, August 2014.

[117] M. Tani, S. Matsuura, K. Sakai, and S.-i. Nakashima. Emission characteristics of photoconductive antennas based on low-temperature-grown GaAs and semi-insulating GaAs. *Applied Optics*, 36(30):7853–7859, October 1997.

[118] TeTechS Inc. Measurement Kit for Research and Development.

[119] Stanford Research Systems. SR860 Operation Manual. https://www.thinksrs.com/downloads/pdfs/manuals/SR860m.pdf, September 2019.

[120] M. Naftaly and R. Dudley. Methodologies for determining the dynamic ranges and signal-to-noise ratios of terahertz time-domain spectrometers. *Optics Letters*, 34(8):1213–1215, April 2009.

[121] I. P. Dick and R. C. Scott. Pig Ear Skin as an In-vitro Model for Human Skin Permeability. *Journal of Pharmacy and Pharmacology*, 44(8):640–645, 1992.

[122] D. B. Bennett, W. Li, Z. D. Taylor, W. S. Grundfest, and E. R. Brown. Stratified Media Model for Terahertz Reflectometry of the Skin. *IEEE Sensors Journal*, 11(5):1253–1262, May 2011.

List of publications

The system developed during this thesis work has been used to perform several studies, directly and indirectly connected to the imaging of skin samples, thus involving the candidate in activities such as the development of plasmonic devices and alternative imaging procedures: the resulting peer reviewed publications and presentations at conferences are listed below.

Journals

[1] V. Aglieri, X. Jin, A. Rovere, R. Piccoli, D. Caraffini, S. Tuccio, F. De Angelis, R. Morandotti, R. Macaluso, A. Toma, and L. Razzari. Improving nanoscale terahertz field localization by means of sharply tapered resonant nanoantennas. *Nanophotonics*, 9(3):683–690, January 2020.

[2] L. Zanotto, R. Piccoli, J. Dong, D. Caraffini, R. Morandotti, and L. Razzari. Time-domain terahertz compressive imaging. *Optics Express*, 28(3):3795–3802, February 2020.

[3] J. Dong, H. Breitenborn, R. Piccoli, L. V. Besteiro, P. You, D. Caraffini, Z. M. Wang, A. O. Govorov, R. Naccache, F. Vetrone, L. Razzari, and R. Morandotti. Terahertz three-dimensional monitoring of nanoparticle-assisted laser tissue soldering. *Biomedical Optics Express*, 11(4):2254–2267, April 2020.

Conferences

[1] A. Tomasino, M. K. Mridha, A. Mazhorova, D. Caraffini, H. Breitenborn, M. Clerici, M. Peccianti, L. Razzari, A. C. Cino, S. Stivala, A. Busacca, and R. Morandotti. Waveguide-Integrated THz Spectral Filter. In *Photonics North 2015*, Ottawa, Canada, 2015.

[2] A. Tomasino, M. K. Mridha, A. Mazhorova, D. Caraffini, H. Breitenborn, M. Clerici, M. Peccianti, L. Razzari, A. C. Cino, S. Stivala, A. Busacca, and R. Morandotti. Two-Wire Waveguide-Based THz Spectral Filter. In *Colloque de Plasma-Québec*, Montréal, Canada, 2015.

[3] A. Tomasino, M. K. Mridha, A. Mazhorova, D. Caraffini, H. Breitenborn, M. Clerici, M. Peccianti, L. Razzari, A. C. Cino, S. Stivala, A. Busacca, and R. Morandotti. Two-Wire Waveguide-Based THz Spectral Filter. In *Fotonica 2015*, Turin, Italy, 2015.

[4] D. Caraffini, R. Piccoli, X. Jin, S. Tuccio, R. Morandotti, and L. Razzari. On the optimization of tapered nanoantennas resonating in the terahertz range. In *2016 Photonics North (PN)*, pages 1–1, Québec, Canada, May 2016.

[5] D. Caraffini, R. Piccoli, X. Jin, S. Tuccio, R. Morandotti, and L. Razzari. Optimal Taper Angle for Gold Nanoantennas Resonating with Terahertz Radiation. In *Colloque de Plasma-Québec*, Montréal, Canada, May 2017.

[6] A. Tomasino, R. Piccoli, D. Caraffini, A. Markov, A. Mazhorova, R. Naccache, F. Vetrone, Y. Jestin, A. Busacca, L. Razzari, and R. Morandotti. Ultra-broadband terahertz time domain spectroscopy by Solid State Biased Coherent Detection. In *2017 42nd International Conference on Infrared, Millimeter, and Terahertz Waves (IRMMW-THz)*, pages 1–2, Cancún, Mexico, August 2017.

[7] H. Breitenborn, J. Dong, A. Bruhacs, D. Caraffini, R. Piccoli, R. Marin, A. Skripka, F. Vetrone, R. Naccache, and R. Morandotti. Characterization of the Photothermal Heating Properties of Nanoparticles by Terahertz Radiation. In *Photonics North 2018: Biophotonics*, Montréal, Canada, June 2018.

[8] D. Caraffini, A. Tomasino, Y. Jestin, A. Busacca, R. Morandotti, and L. Razzari. Nonlinear Frequency Mixing Between Terahertz and Optical Waves in Silica. In *Photonics North 2018: High Power Laser Technology, Ultrafast Optics and Applications*, Montréal, Canada, June 2018.

[9] X. Jin, J. Dong, A. Rovere, R. Piccoli, D. Caraffini, A. Cerea, F. De Angelis, R. Morandotti, R. Macaluso, A. Toma, and L. Razzari. Near-field Enhancement Optimization by Tapering Terahertz Gold Nanoantennas. In *Photonics North 2018: Photonic Theory Design and Simulations*, Montréal, Canada, June 2018.

[10] H. Breitenborn, J. Dong, R. Piccoli, D. Caraffini, L. Razzari, Fiorenzo Vetrone, Rafik Naccache, and Roberto Morandotti. Terahertz Subsurface Imaging of Nanoparticle-mediated Plasmonic Heating in Skin. In *Photonics North 2019: Biophotonics*, Québec, Canada, May 2019.

[11] J. Dong, H. Breitenborn, D. Caraffini, R. Piccoli, A. O. Govorov, L. Razzari, R. Naccache, F. Vetrone, and R. Morandotti. Investigation of Nanoparticle-Assisted Laser Tissue Soldering by Terahertz Radiation. In *2019 Conference on Lasers and Electro-Optics Europe European Quantum Electronics Conference (CLEO/Europe-EQEC)*, pages 1–1, Munich, Germany, June 2019. IEEE.

[12] L. Zanotto, R. Piccoli, J. Dong, D. Caraffini, R. Morandotti, and L. Razzari. Terahertz compressive imaging directly in the time domain. In *2020 CLEO: Laser Science to Photonic Applications (Accepted)*, San Jose, USA (to be held online due to COVID-19), May 2020.

[13] V. Aglieri, X. Xin, A. Rovere, R. Piccoli, D. Caraffini, S. Tuccio, F. De Angelis, R. Morandotti, R. Macaluso, A. Toma, and L. Razzari. Improved Near Field Enhancement by Tapering Terahertz Gold Nanoantennas Contribution. In *IEEE International Conference in Nanotechnology*, Montréal, Canada, 2020.

[14] L. Zanotto, R. Piccoli, J. Dong, D. Caraffini, R. Morandotti, and L. Razzari. THz Single-pixel Imaging in Time-domain. In *Photonics North (Submitted)*, Niagara Falls, Canada, 2020.

[15] J. Dong, H. Breitenborn, R. Piccoli, L. V. Besteiro, P. You, D. Caraffini, Z. Wang, A. O. Govorov, R. Naccache, F. Vetrone, L. Razzari, and R. Morandotti. Dynamic Terahertz Investigation of Nanoparticle-assisted Laser-tissue Interaction. In *International Conference on Infrared, Millimeter, and Terahertz Waves (IRMMW-THz) (Submitted)*, Buffalo, USA, 2020.